TÉCNICO LISBOA

Layerwise electro-elastic user-defined elements in Abaqus for static and free vibration analysis of piezoelectric composite plates

João Pedro Dos Anjos Moreira

Thesis to obtain the Master of Science Degree in

Aerospace Engineering

Supervisors: Prof. Filipa Andreia de Matos Moleiro
Prof. Aurélio Lima Araújo

Examination Committee

Chairperson: Prof. Filipe Szolnoky Ramos Pinto Cunha
Supervisor: Prof. Filipa Andreia de Matos Moleiro
Member of the Committee: Prof. José Arnaldo Pereira Leite Miranda Guedes

January 2021

I declare that this document is an original work of my own authorship and that it fulfills all the requirements of the Code of Conduct and Good Practices of the Universidade de Lisboa.

To my father and to my mother. *Obrigado !*

Acknowledgments

The driving force for the present thesis is a combination of an insatiable intellectual curiosity with a formidable human support provided by the thesis supervisor's, family and closest friends.

To my mentors, Professor Filipa Moleiro and Professor Aurélio Araújo, no words could ever describe how thankful and honoured I am for their continuous guidance and encouragement. Firstly, I'm thankful to Professor Filipa Moleiro for providing me a large branch of data, without which the present thesis would not be certainly so self-satisfactory. In the same level, I'm also thankful to Professor Aurélio Araújo for the time and knowledge spent on helping me on the development and validation of the present models.

Nothing was possible without the love, education and opportunities that my parents, Mário and Teresa, had given to me. Also, the companion and loyalty that I've always received from my closest friends, Gonçalo Pereira, Mariana Marques and Carolina Ravara, are essential for achieving my objectives throughout my life.

I'm specially thankful for the willingness and support of my closest one.

Resumo

O crescente desenvolvimento de métodos fiáveis de análise de estruturas piezoelétricas laminadas em compósito com atuação por piezoelétricos é motivado pela ampla aplicabilidade em engenharia aeroespacial, complementando a elevada resistência específica dos materiais compósitos com a capacidade de monitorização e atuação dos materiais piezoelétricos.

Consequentemente, este trabalho apresenta um estudo computacional em análise estática e de vibrações livres com dois elementos finitos de placa electro-elásticos, implementados utilizando uma subroutina disponível para definir elementos próprios do utilizador (UEL), no software comercial Abaqus. Em ambos, uma descrição *Layerwise* para três lâminas discretas é utilizada para o campo de deslocamentos da teoria de primeira ordem de deformação por corte de placas laminadas, assim como uma expansão linear ou quadrática do potencial elétrico ao longo da direção transversal de cada camada, UEL1 e UEL2, respetivamente.

Os modelos desenvolvidos são comparados com as soluções exatas tridimensionais, para o caso de placas simplesmente apoiadas, reportadas na literatura. Para tal consideram-se duas sequências de laminagem com diferentes materiais piezoelétricos nas faces das mesmas, desde o caso de placas finas, moderadamente espessas a espessas.

A capacidade preditiva em resposta estática evidenciada pelos modelos é demonstrada pela concordância com as soluções exatas, nomeadamente ao nível de deslocamentos e potencial, assim como de tensões no plano para placas finas e moderadamente espessas. Em análise de vibrações livres, os doze primeiros modos e frequências de vibração previstas pelos modelos implementados revelam uma boa concordância com as soluções exatas, mesmo para placas mais espessas.

Palavras-chave: Placas piezoelétricas em compósito, Abaqus *user-defined element*, Teoria *Layerwise*, Teoria de primeira ordem, Modelação electro-elástica.

Abstract

The development of reliable methods for analysis of piezoelectric multilayered composite structures is motivated by a wide range of applications in aerospace engineering, combining high specific mechanical properties of composite materials, with monitoring and actuation capabilities of the piezoelectric materials.

Consequently, this work presents a computational study in static and free vibration analysis, using two electro-elastic plate elements implemented in a user-defined element (UEL) subroutine available in Abaqus. On both of them, a Layerwise description for three discrete layers is used, assuming in each layer a first-order shear deformation displacement field, as well as a linear or quadratic z-expansion of the electric potential, respectively, UEL1 and UEL2.

Furthermore, the models here developed are compared with three-dimensional exact solutions, available for the case of simply-supported plates reported in the literature. For this purpose, two multilayered plates with different piezoelectric materials in the face layers are considered, from the case of thin, moderately thick to thick plates.

The models predictive capabilities in static response for the displacements, electric potential and in-plane stresses is demonstrated to be in agreement with the exact solutions for thin and moderately thick plates. In free vibration analysis, the first twelve vibration modes and frequencies predicted by the developed models, reveal a good accuracy of the models comparatively to the exact solutions, even for thicker plates.

Keywords: Piezoelectric composite plates, Abaqus user-defined element, Layerwise theory, First-order theory, Electro-elastic modelling

Contents

List of Tables

List of Figures

Abbreviations

3D	Three-Dimensional
DOF	Degree of freedom
PVD	Principle of Virtual Displacements
RMVT	Reissner's Mixed Variational Theorem
ESL	Equivalent Single-Layer
LW	Layerwise
CLPT	Classical Laminated Plate Theory
FSDT	First-Order Shear Deformation Theory
TSDT	Third-Order Shear Deformation Theory
HSDT	High-Order Shear Deformation Theory
UEL	User-Defined Element
UEL1	User-Defined Element with linear z-expansion of the electric potential
UEL2	User-Defined Element with quadratic z-expansion of the electric potential
DLOAD	User-Defined Load
DISP	User-Defined Boundary Conditions
(C)	Constitutively derived
(E)	Equilibrium derived

Nomenclature

Roman symbols:

a	Plate dimension along the x-axes
$\{a\}$	Element DOFs vector
b	Plate dimension along the y-axes
B_i	Induced magnetic field in the i-direction
$[B]_j$	j-node generalized strain matrix
$[B_\phi]_j$	j-node generalized electric field matrix
$[B]$	Element generalized strain matrix
$[B_\phi]$	Element generalized electric field matrix
C_{ijkl}	Elastic tensor
$C_1,\ C_2$	Integration constants
$\{d\}_j$	j-node DOFs vector
D_i	Electric displacement in the i-direction
$\{D\}$	Electric displacement vector
$\{\hat{D}\}$	Electric displacement resultants vector
e_{ijk}	Piezoelectric coefficients tensor
$[e]$	Plane stress piezoelectric coefficients matrix
$[\bar{e}]$	Piezoelectric coefficients matrix in the global coordinate system
$[\hat{e}]$	Generalized piezoelectric coefficients matrix
E_i	Electric field or Young's modulus in the i-direction
$\{E\}$	Electric field vector
$\{\hat{E}\}$	Generalized electric field vector
$[I]$	Generic identity matrix
f_i	Body force component in the i-direction
$\{f_c\}$	Concentrated force vector
$\{f_s\}$	Surface force vector
F	Arbitrary scalar field
$g_s^{(k)}, g_i^{(k)}, g_m^{(k)}$	k-layer transverse coordinate functions
h	Total thickness
$h^{(k)}$	k-layer thickness
$h_t,\ h_c,\ h_b$	Discrete layers thicknesses
$\bar{H}_{n_{(k)}}$	k-layer transverse coordinate integration functions
$[J]$	Jacobian matrix
K_s	Shear correction factor
$[K_{uu}]$	Elastic Stiffness matrix
$[K_{u\phi}],\ [K_{\phi u}]$	Piezoelectric coupling matrices
$[K_{\phi\phi}]$	Dielectric stiffness matrix

m	Number of half-waves in the x-direction
M_G	Number of Gauss points in ξ-direction
$M_{xx},\ M_{yy},\ M_{xy}$	Moment resultants
$[M_{uu}]$	Mechanic mass matrix
n	Number of half-waves in the y-direction
N_G	Number of Gauss points in η-direction
$N_{xx},\ N_{yy},\ N_{xy}$	In-plane force resultants
$[N]$	Element mechanic DOFs shape functions matrix
$[N_\phi]$	Element electric DOFs shape functions matrix
$[P]$	Auxiliary matrix for evaluate the mass matrix
q	Distributed transverse load
q_0	Load amplitude
$Q_x,\ Q_y$	Transverse force resultants
$[Q]$	Plane stress elastic properties
$[\bar{Q}]$	Plane stress elastic properties in the global coordinate system
$[\hat{Q}]$	Generalized elastic properties
S	Entropy
$[S]$	Strain transformation matrix
$[S_\phi]$	Electric field transformation matrix
t	Time
t_i	Surface traction in the i-direction
T	Kinetic energy
S	Surface area
u_i	Displacement in the i-direction
$\dot{u}_i$	Time-derivative of the displacement in the i-direction
U	Electromechanical potential energy
(u, v, w)	Cartesian displacement components
V	Total energy
W	External work
$W_i,\ W_j$	Gauss weights
(x, y, z)	Problem Cartesian coordinate system
(x_1, x_2, x_3)	Material Cartesian coordinate system
z_k	k-layer local transverse coordinate
$\bar{z}_k$	k-layer mid-plane transverse coordinate
$[Z]$	Displacements transformation matrix

Greek symbols:

$\alpha_i,\ \beta_i$	Layerwise constants
γ_{ij}	Engineering shear strains in plane x_i-x_j

δ	Variational operator
$\delta_\bullet$	Relative discrepancy/error for variable or model $\bullet$
Δ	Auxiliary parameter
ϵ_0	Vacuum dielectric constant
ϵ_{ij}	Dielectric tensor
$[\epsilon]$	Dielectric matrix
$[\bar{\epsilon}]$	Dielectric matrix in the global coordinate system
ε_{ij}	Infinitesimal strain tensor
$\{\varepsilon\}$	Strain vector
$\{\hat{\varepsilon}\}$	Generalized strain vector
ε_{ijk}	Lévi-Civita symbol
θ	Fibres orientation
θ_x	Rotation about the y-axes (anticlockwise)
θ_y	Rotation about the x-axes (clockwise)
λ_x	HSDT generalized rotation in x-axes
λ_y	HSDT generalized rotation in y-axes
ν_{ij}	Poisson's ratio in plane x_i-x_j
(ξ, η)	Natural coordinates
ρ	Density
σ_{ij}	Cauchy stress tensor
$\{\sigma\}$	Stress vector
$\{\hat{\sigma}\}$	Stress resultants vector
τ_{ij}	Engineering shear stresses in plane x_i-x_j
ϕ	Electric potential
$\hat{\phi}$	Applied electric potential
ϕ_0	Electric potential amplitude
$\{\varphi\}_j$	Nodal electric DOFs vector
$\{\bar{\varphi}\}$	Element electric DOFs vector
χ_x	HSDT generalized displacement in x-axes
χ_y	HSDT generalized displacement in y-axes
ψ_j	j-node interpolation function
$\hat{\psi}_j$	Master element j-node finite element interpolation function
$[\Psi]_j$	j-node mechanic DOF shape function matrix
$[\Psi_\phi]_j$	j-node electric DOF shape function matrix
Ψ_0	Free energy
ω_{mn}	Vibration frequency of the mode (m, n)
$\hat{\Omega}$	Master element domain
Ω_e	e-element domain
$\Omega_{(k)}$	k-layer volume domain

Calligraphic symbols:

$\mathcal{E}_{ij}$	Green-Lagrange tensor
$\mathcal{J}$	Jacobian matrix determinant
$\mathcal{L}$	Lagrangian function
$\mathcal{Q}$	Distributed surface charge
$\mathcal{T}$	Absolute temperature
$\mathcal{U}$	Internal energy

Miscellaneous symbols:

∂	Partial derivative operator
∂_i	Partial derivative regard to i-direction
∇_i	Gradient operator in the i-direction
$\partial\Omega$	Boundary of the domain Ω

Subscripts:

$\bullet_{(k)}$	Variable $\bullet$ for the k-layer
$\bullet_t$	Variable $\bullet$ for the top layer, except on S_t, which is a certain surface with applied stress
$\bullet_c$	Variable $\bullet$ for the core layers, except in $\{f_c\}$
$\bullet_b$	Variable $\bullet$ for the bottom layer, except for generalized strains, for which means membrane
$\bullet_0$, $\bullet_{mid}$	Variable $\bullet$ with respect to the mid-plane, except q_0, ϵ_0, ϕ_0 and Ψ_0
$\bullet_m$	Variable $\bullet$ membrane components, except in g_m
$\bullet_s$	Variable $\bullet$ shear components, except in $\{f_s\}$ and g_s
$\bullet_{top}$	Variable $\bullet$ for the layer top surface
$\bullet_{bot}$	Variable $\bullet$ for the layer bottom surface

Supercripts:

$\bullet^*$	Reduced plane stress $\bullet$ property, except in the inverse Jacobian matrix
$\bullet^{(k)}$	Variable $\bullet$ for the k-layer
$\bullet^t$	Variable $\bullet$ for the top layer
$\bullet^c$	Variable $\bullet$ for the core layers
$\bullet^b$	Variable $\bullet$ for bottom layer
$\bullet^{inf}$	Variable $\bullet$ for the layer bottom surface
$\bullet^{sup}$	Variable $\bullet$ for the layer top surface
$\bullet^{(e)}$	Variable $\bullet$ for the e-element
$\bullet^s$	Variable $\bullet$ for a certain surface
$\bullet^T$	Transpose of variable $\bullet$

Chapter 1

Introduction

1.1 Motivation and Topic Overview

New challenges have emerged in the field of structural design, whether in aerospace, automobile or naval engineering. Designing lightweight and very stiff structural members has been achieved using multilayered composites. The resort to these materials represents more than 50% of modern commercial aircraft's structures [1], reducing its weight and consequently reducing the fuel consumption, as well as pollutant emissions.

In the current days, a new era of advanced structures with monitoring and actuation capabilities is a goal. These intelligent structures behave as close-loop systems, including health monitoring features, active vibration control, noise suppression, energy harvesting or even aeroelastic control. Viscoelastic materials, shape memory alloys, piezoelectric and piezomagnetic materials have been investigated due to a large number of applications in smart structures. In these types of materials, complex constitutive behaviour laws are found, leading to a multidisciplinary field of research. Multiphysics phenomena such as piezoelectricity, magnetostriction or hygrothermal effects, in general anisotropic elastic materials, can be translated into a coupling phenomena between continuum fields, whether mechanical, electrical, magnetic or thermochemical as can be seen in Heyliger [2], Lee and Saravanos [3], Moleiro et al. [4] and in Campos et al. [5].

Piezoelectric materials, such as the piezoceramic lead zirconate titanate (PZT) and polar polymers such as Polyvinylidene Fluoride (PVDF), have the ability to generate an electric potential difference and thus, an electric field arises from a mechanical deformation (*direct piezoelectric effect*), likewise mechanical deformation is produced when an electric field is applied (*converse piezoelectric effect*). These properties make piezoelectric materials capable to be tailored to act in active control of dynamic systems. For instance in distributed sensors, mechanical energy is transformed to an electric output for monitoring purposes, and in actuators, electric energy is converted to mechanical displacement. Historically the *direct piezoelectric effect* was discovered by Curie brothers [6] in 1880, while investigating pyroelectric crystals. The *converse piezoelectric effect* is only proved one year later in Lippmann [7], using fundamental thermodynamic principles.

The increased interest in piezoelectric materials is due to a wide range of their applications in smart

structures, particularly in aerospace structures such as wings, controls and high flexible long satellite panels. Lightweight and very stiff structures having monitoring and actuation capabilities can be designed combining piezoelectric layers with multilayered composites. In order to study the engineering applications of these types of structures, robust and accurate methods, either analytical or numerical, must be developed and experimentally validated.

By the 70's, exact three-dimensional (3D) solutions for the fundamental equilibrium equations of multilayered composite plates is derived by Pagano [8]. A zig-zag through-thickness continuous displacement field is demonstrated, as well as for the transverse stresses, leading to the commonly known C_z^0 interlaminar continuity conditions. In the following years, Heyliger [2, 9, 10] extended the work of Pagano, considering transversely poled piezoelectric layers (extension mode actuators) in multilayered orthotropic composite plates. Static and dynamic 3D equilibrium electro-elastic equations for simply-supported piezoelectric composite plates are solved by imposing both essential and natural boundary conditions and a compatible continuous description for the several transverse fields. More recently, electro-elastic exact solutions for piezoelectric multilayered composite plates are reported by Moleiro et al. [11] for static response, and in Moleiro et al. [12] for free vibrations. Also in Moleiro et al. [13], both static and free vibration exact solutions are reported for more piezoelectric multilayered composite plates, as well as for soft core sandwich plates. In a multilayered composite plate with skin layers made of extension mode actuators under applied transverse electric field, the piezoelectric layers undergo an in-plane deformation, where the lateral dimensions are increased or decreased, forcing the remaining substrate elastic layers in the multilayered composite core to deform. Further remarkable exact solutions are developed by Vel and Batra [14] considering an axially poled piezoelectric shear actuator core between elastic face layers, as well as by Baillargeon and Vel [15] for vibrations and active damping of composite plates, with embedded piezoelectric shear mode actuators.

Moreover, from the above-mentioned Heyliger's exact solutions, the C_z^0-requirements for the mechanical domain imply continuous displacements and transverse stresses at the layer's interfaces, while in-plane stresses are typically discontinuous between adjacent layers due to a possible change of the mechanical properties along the stacking scheme. Likewise, in-plane strains must be continuous at the layer's interfaces, although the change in mechanical properties could lead to discontinuous transverse strains. In terms of the electric domain, the electric potential must exhibit C^0-continuity at the interfaces, as well as the transverse electric displacement in the absence of internal electrodes, contrasting to the discontinuous in-plane electric displacements in consequence of different electric properties. In the same way as the in-plane strains, also the in-plane electric field components are through-thickness continuous, with C^0-continuity at the interfaces.

Although the exact solutions are a very resourceful mathematical description without any simplified assumptions, they represent a limited spectrum of combinations of essential and natural boundary conditions for the fundamental electro-elastic equations. Furthermore, in static analysis of piezoelectric composite plates only simply supported plates are considering and two load cases are exactly solved, namely an applied bi-sinusoidal distributed transverse load and a bi-sinusoidal electric potential, in order to respect the boundary conditions. Consequently, finite element models for multilayered piezoelectric

plates and shells appear to be necessary for studying more complex smart structures. However, accurate and efficient finite element models could be formulated by taking into account the exact solutions for the validation of the finite element models, mixing plate or shell theories and electric potential approximations.

The state of the art of theories and finite element models for multilayered composite structures is well presented by Carrera [16]. Also, Reddy's books [17, 18] are remarkable introductions to the study of laminated plates and the finite element method, respectively. For piezoelectric finite elements, Saravanos [19] presents the fundamental principles and computational methods for analysis of piezoelectric plates, shells and beams, assuming a linear through-thickness electric potential, while Benjeddou [20] reports a comprehensive survey in the field of electromechanical coupled analysis, using the finite element method. From these articles and books, sophisticated formulations must be applied in order to describe the overall physical mechanism that governs the response of multilayered composite plates and the piezoelectric effect associated with the presence of piezoelectric sensors or actuators.

For plates and shells, in which the transverse dimension, i.e., the thickness, is at least one order of magnitude lower than the in-plane dimensions, the three-dimensional problem can be reduced to a bi-dimensional one, under plane stress assumptions. In fact, bi-dimensional electro-elastic plate and shell finite elements differ from the classical ones by adding electromechanical coupling, and consequently electric degrees of freedom (DOFs) must be considered. Also, in Benjeddou [20] it is proved that the assumption of a through-thickness linear electric potential systematically neglects the contribution of the induced electric potential and consequently a partial electromechanical coupling is achieved. In order to enhance the electromechanical coupling, one could assume a quadratic through-thickness expansion of the electric potential, as suggested by the same author [20].

From the point of view of the calculus of variations applied to continuum solid mechanics, the *Principle of Virtual Displacements* (PVD) leads to a classical displacement formulation, while mixed variational principles, such as the *Reissner's Mixed Variational Theorem* (RMVT), which is well reviewed by Carrera [21], leads to a mixed displacement-strain-stress formulation. Noting that in coupled electro-elastic analysis, the electric potential is a primary variable, while the electric field and the electric displacement field are secondary variables, which can be introduced in the mixed variational formulations in a similar way as for strains and stresses. The mixed variational theorems represent an efficient approach to *a priori* fulfill the C_z^0-requirements for the displacements, electric potential, transverse stresses and transverse electric displacements of piezoelectric multilayered plates, demonstrated by the exact solutions.

According to Carrera [21], both PVD and Reissner's mixed and classical forms represent the ways to choose the unknown variables for the analysis of multilayered plates, where these variables could be described using *Equivalent Single Layer* (ESL) models or using *Layerwise Theories* (LW), as suggested by Reddy [17]. The ESL models are the most simple, and consequently with lowest computational effort, where the unknown variables are determined for the whole plate. Pushing forward in accuracy and in the number of variables, the LW descriptions allow to take each layer of the stacking scheme as an independent layer with respective governing equations and interface continuity conditions. A review on LW theories is presented by Li [22], dividing these theories in discrete LW models, with an assembly of

individual single layers through interlaminar continuity conditions, and in integrated LW models, where the transverse fields, either for the primary or secondary variables, are approximated by one-dimensional interpolation functions, being the in-plane variables discretized with bi-dimensional finite elements.

Electro-elastic integrated LW classical models were developed earlier by Saravanos et al. [23], using a linear z-expansion for the electric potential in each layer, and more recently, Semedo Garção et al. [24] and Robaldo et al. [25] extended the previous work to higher order z-expansion models for the electric potential. In order to improve LW classical models from the point of view of the C_z^0-requirements for the secondary variables on piezoelectric composite plates, Garcia Lage et al. [26] and Carrera et al. [27] developed LW mixed models. Moreover, Moleiro et al. [28, 29] developed LW mixed models based on the least-squares method for analysis of piezoelectric multilayered composite plates, where the least-squares models appear to be insensitive to shear locking, which is typically present in the analysis of thin plates with LW classical models.

Axiomatic theories based on displacements play an important role in the analysis of multilayered composite plates and shells with bi-dimensional finite elements on a first intuitive approach, with low computational cost. Hence, in a classical axiomatic approach for electro-elastic plates, the displacements and the electric potential are *a priori* assumed to have prescribed variation along the thickness direction, where both ESL and discrete LW theories can be used to model the overall multilayered plate. Reddy's book [17] provides the formulation of the common ESL axiomatic theories for plates and shells, where analytical solutions and numerical ones are largely presented. Regarding discrete LW models, Li [22] reviewed the main axiomatic theories used for the displacements and Polit et al. [30] for the electric potential approximations. The discrete LW theories allow formulations for a generalized number of layers as reported by Carrera [16], as well as in the works by Moreira et al. [31] and Mantari and Guedes Soares [32], although the same approach could be used for a prescribed number of layers, as by Araújo et al. [33] and by Lam et al. [34].

For an accurate analysis of thin and moderately thick piezoelectric multilayered composite plates with bi-dimensional elements, the LW description for the displacement field and for the electric potential is mandatory to at least fulfill the interlaminar continuity conditions for the primary variables. Since the electromechanical behaviour of most of the piezoelectric materials is dependent on shear strains, the First-Order Shear Deformation Theory (FSDT) displacement field could be used as first approximation for the kinematic description of the discrete layers, combined with a linear or quadratic z-expansion of the electric potential. A further reduction on the number of unknowns for a discrete LW electro-elastic plate element can be achieved considering the case of three discrete layers, where a multilayered composite core is treated as an ESL, with piezoelectric face layers on both top and bottom surfaces.

Powering the use of the finite element method, the commercial finite element softwares are an important tool for engineers and for academic purposes due to a user-friendly environment with 3D design capabilities, robust numerical solvers and a large library of finite elements and analysis, where the visualization and interpretation of the results are also facilitated. Abaqus is one of the most used commercial finite element codes and allows the user to program the stiffness and mass matrices of the elements used for the desired analysis. In order to implement new and improved finite elements and easily use

them, the *User-Defined Element* (UEL) subroutine available in Abaqus, among with others subroutines can be implemented in Fortran programming language, such as the DLOAD subroutine for prescribing loads or the DISP subroutine for specifying boundary conditions, accordingly to the instructions present in the software's manual [35].

1.2 Objectives

The present thesis concerns a new approach for analysis of piezoelectric composite plates through discrete layerwise electro-elastic plate finite elements, implemented using Abaqus UEL subroutine. The model assumes three discrete layers, where a multilayered composite core treated as an ESL is bounded in both top and bottom surfaces with piezoelectric face layers. Along with a piecewise linear kinematic description for each discrete layers, both through-thickness linear and quadratic electric potential approximations are used for comparison purposes, as suggested by Benjeddou [20].

In order to have a comprehensive model verification, two piezoelectric composite plates are considered, using different piezoelectric materials for the face layers. Moreover, access to static and free vibrations analysis of simply-supported piezoelectric composite plates with various aspect ratios, following the work of Heyliger [2, 9, 10] and Moleiro et al. [11–13, 28] is the main goal. For both static and free vibration analysis, the stacking schemes of interest will be the same two symmetric piezoelectric composite plates reported by Moleiro et al. [13] for $a/h = 10$ and 4, considering also the case of thinner plates with $a/h = 100$ and 20.

In static analysis the monitoring and actuation responses are studied through the classical test cases reported by the previous authors, namely a bi-sinusoidal applied distributed transverse load and an applied bi-sinusoidal electric potential, for which exact solutions are available and used for verification of the present models. Furthermore, improvements on the determination of the transverse shear stresses, using direct integration of the three-dimensional equilibrium equations, as suggested by Reddy [17], is also an objective.

For free vibration analysis, the homogeneous electric potential boundary conditions concerns the main focus of interest. In this case, the implemented finite element models are compared to a 3D piezoelectric element available in Abaqus and to the benchmarked exact solutions reported by Moleiro et al. [13] for $a/h = 10$ and 4.

1.3 Thesis Outline

The present thesis is divided in eight chapters, followed by five appendix chapters, concerning theoretical demonstrations, detailed matrices introduced in the generalized model and also some complementary results for thin plates. Briefly, the structure of the thesis contents is the following:

Chapter 1: An introduction to piezoelectric composite plates is made. Historical perspective, applications, theories and models are also presented as motivation for the present thesis and associated objectives.

Chapter 2: Background theoretic material related to multilayered anisotropic piezoelectric com-

posite plates is presented in order to build a solid foundation for the following chapters.

Chapter 3: An axiomatic piezoelectric layerwise model is formulated. The displacement field and electric potential for three discrete layers is formulated, as well as their derivatives: strains and electric field, respectively.

Chapter 4: The finite element formulation for the presented models is conducted, leading to the element mass and stiffness matrices. Numerical techniques are explained, as well as post-processing procedures.

Chapter 5: Abaqus UEL subroutine implementation in Fortran is discussed, including the linking to Abaqus is explained.

Chapter 6: Static analysis results for applied load and applied potential are provided and compared to exact solutions for simply-supported piezoelectric composite plates, considering two stacking schemes, from thin to thicker plates.

Chapter 7: Vibration frequencies and associated modes for simply-supported piezoelectric composite plates with two stacking schemes, are presented and compared to Abaqus-3D elements solutions and exact solutions, from thin to thicker plates.

Chapter 8: Concluding remarks and achievements regarding the present work are presented, along with future work suggestions.

1.4 Notation

Along the present work, several tensors with different orders are used. The notation used to represent the tensors follows the classical Einstein notation, where the order of the tensor is the same as the number of indices used, as well as the summation rule. Besides the Einstein convention, vector and matrices are sometimes represented using invariant notation in order to avoid a large number of indices in some variables. Although bold written tensors are simpler, this notation doesn't clearly distinguish first order tensors (vectors) and second order tensors (matrices). Therefore, vector entities are represented using braces ($\{\cdot\}$), while matrices are represented using square brackets ($[\cdot]$).

There are also some conventions in the subscripts that the author wants to highlight. First, the subscript 0 indicates mid surface of the layer while the subscripts inf and sup stays for the bottom and top surfaces of the layer, respectively. Typically, an isolated subscript or superscript (k) refers to the k-discrete layer: top, core and bottom layers.

Chapter 2

Background

In this chapter, the fundamental principles and equations regarding the modelling and analysis of multilayered piezoelectric composite plates are presented. The theory of linear elasticity is combined with linear dielectrics equations, providing an electromechanical coupling phenomena present in piezoelectric materials. Consequently, the main axiomatic theories for multilayered plates and electric potential approximations are discussed for the modelling and analysis of piezoelectric composite plates.

2.1 Anisotropic Electroelasticity

A deformable continuum body under an elastic deformation experiments a mechanical evolution between the undeformed configuration and the deformed one, featured in the displacement field components u_i, with $i = \{1, 2, 3\}$. From the displacement field, the deformation of the material fibers can be measured through the definition of the Green-Lagrange tensor, $\mathcal{E}_{ij}$, as:

$$\mathcal{E}_{ij} = \frac{1}{2}\left(\frac{\partial u_i}{\partial x_j} + \frac{\partial u_j}{\partial x_i} + \frac{\partial u_j}{\partial x_i}\frac{\partial u_i}{\partial x_j}\right) \tag{2.1}$$

Whenever the displacements are much lower than a reference initial dimension of the body, small displacements can be assumed. Hence, the last higher order term in the Green-Lagrange tensor definition can be neglected, leading to the infinitesimal or linear strain tensor, ε_{ij} , defined as,

$$\mathcal{E}_{ij} \approx \varepsilon_{ij} = \frac{1}{2}\left(\frac{\partial u_i}{\partial x_j} + \frac{\partial u_j}{\partial x_i}\right) \tag{2.2}$$

where for $i \neq j$, the engineering shear strains or distortions, γ_{ij}, are defined as follows:

$$\gamma_{ij} = 2\varepsilon_{ij} = \frac{\partial u_i}{\partial x_j} + \frac{\partial u_j}{\partial x_i} \text{ for } i \neq j \tag{2.3}$$

From the theory of linear elasticity, the material response in an elastic deformation is a linear function of the deformation, which is measured by the strain tensor. This strain-stress relation allows the calculation of the Cauchy stress tensor σ_{ij} and defines the so-called constitutive equation or law. For a linear elastic anisotropic material, the material behaviour is governed by the generalized form of the Hooke's

law, that holds,

$$\sigma_{ij} = C_{ijkl}\varepsilon_{kl} \tag{2.4}$$

where C_{ijkl} is the 4$^{\text{th}}$-order stiffness or elastic tensor, with 3^4 =81 scalar components. From an angular momentum balance to an infinitesimal piece of volume, within an elastic body in equilibrium, it is known that the Cauchy stress tensor is symmetric ($\sigma_{ij} = \sigma_{ji}$), as well as the linear strain tensor ($\varepsilon_{kl} = \varepsilon_{lk}$), by definition, in equation (2.2). Consequently, in the constitutive equation (2.4), from the symmetry of the stress tensor, the elastic tensor is symmetric in i and j ($C_{ijkl} = C_{jikl}$). Similarly, from the strain tensor symmetry, the elastic tensor is also symmetric in k and l ($C_{ijkl} = C_{ijlk}$). These symmetries reduce the 81 scalar components to only 6×6=36 independent components.

In piezoelectric materials, the elastic and electrical domains are coupled through the direct and converse piezoelectric effects. Consequently, the electrostatic theory of dielectric materials must be taken into account in order to describe the overall response of this type of materials. Maxwell equations arise as a set of four differential equations that describe the electromagnetic field in dielectric mediums (Serway's book [36]). Following Reddy's book [17], negligible magnetic effects may be assumed in piezoelectric materials, leading to an electro-quasi-static approximation, where the time derivative of the magnetic field components B_i in the Faraday's law can be neglected as follows,

$$\varepsilon_{ijk}\nabla_j E_k = -\partial_t B_i = 0 \tag{2.5}$$

where ∇_j is the spatial gradient operator in the j-direction, E_k the electric field component in the k-direction, ∂_t the time derivative operator and ε_{ijk} is the Lévi-Civita symbol. In line with equation (2.5), the rotational of the electric field is null, yielding a conservative electric field expressed as a gradient of a certain scalar field as shown,

$$E_k = -\frac{\partial \phi}{\partial x_k} \tag{2.6}$$

where the scalar field ϕ is known as electric potential. The negative sign appears from the opposing definitions of a mathematical gradient and the physical convention for the electric field direction.

A dielectric material under an applied external electric field, causes a displacement of bound (fixed) charged elements (atomic nuclei and electrons) and consequently a local electric dipole moment is generated, leading to a polarized medium neutral in charge. Opposing to bound charges, the free charges are the ones that turn the dielectric material non-neutral, inducing the electric displacement field components D_i. The electric displacements for an homogeneous linear dielectric material are obtained using the constitutive equation for the electric field as,

$$D_i = \epsilon_{ij} E_j \tag{2.7}$$

where the constants of proportionality are the dielectric constants, or electric permittivities, figured in the 2$^{\text{nd}}$-order dielectric tensor ϵ_{ij}, with six independent components.

The governing constitutive relations for piezoelectric materials are the generalized Hooke's law (2.4) and the constitutive electric field equation (2.7), both of them modified to account for a linear electrome-

chanical coupling through the introduction of piezoelectric coefficients. These piezoelectric coefficients, present in the 3rd-order piezoelectric tensor e_{ijk}, add a linear dependency of the stresses on the electric field, as well as a linear influence of the strains on the electric displacements. The general form of these equations is derived from the first thermodynamic principle, as can be seen in the Appendix A, leading to the following piezoelectric constitutive equations,

$$\begin{aligned} \sigma_{ij} &= C_{ijkl}\varepsilon_{kl} - e_{ijk}E_k \\ D_i &= e_{jki}\varepsilon_{jk} + \epsilon_{ij}E_j \end{aligned} \tag{2.8}$$

or using Kelvin-Voigt notation for the higher-order tensors,

$$\begin{aligned} \{\sigma\} &= \begin{Bmatrix} \sigma_1 & \sigma_2 & \sigma_3 & \sigma_4 & \sigma_5 & \sigma_6 \end{Bmatrix}^T \\ &= \begin{Bmatrix} \sigma_{11} & \sigma_{22} & \sigma_{33} & \sigma_{23} & \sigma_{13} & \sigma_{12} \end{Bmatrix}^T \end{aligned} \tag{2.9}$$

$$\begin{aligned} \{\varepsilon\} &= \begin{Bmatrix} \varepsilon_1 & \varepsilon_2 & \varepsilon_3 & \varepsilon_4 & \varepsilon_5 & \varepsilon_6 \end{Bmatrix}^T \\ &= \begin{Bmatrix} \varepsilon_{11} & \varepsilon_{22} & \varepsilon_{33} & \gamma_{23} & \gamma_{13} & \gamma_{12} \end{Bmatrix}^T \end{aligned} \tag{2.10}$$

the piezoelectric constitutive equations (2.8) can be written in a single-index notation as:

$$\begin{aligned} \sigma_i &= C_{ij}\varepsilon_j - e_{ik}E_k \\ D_k &= e_{kj}\varepsilon_j + \epsilon_{kl}E_l \end{aligned} \tag{2.11}$$

where $i, j = \{1, .., 6\}$ and $k, l = \{1, 2, 3\}$, noting that for $k = l$ and $j = \{1, 2, 3\}$ results $\varepsilon_j = \varepsilon_{kl}$, as well as for $k \neq l$ and $j = \{4, 5, 6\}$ results $\varepsilon_j = 2\varepsilon_{kl} = \gamma_{kl}$.

Assuming an hyperelastic material, the C_{ij} elastic matrix must be symmetric, i.e, $C_{ij} = C_{ji}$, remaining only 21 independent constants for the elastic tensor, as can be seen in Reddy [17]. Also, when considering general anisotropic hyperelastic piezoelectric material, there are only 18 independent components for the piezoelectric tensor and only 6 for the dielectric tensor.

Further reductions can be achieved taking into account material symmetries as demonstrated in Reddy's book [17]. Beginning with materials that don't have any material symmetries, called triclinic solids, the number of independent material properties is the same as for general anisotropic materials. By adding one reflective symmetry plane, monoclinic materials are found, having 13 independent elastic constants, since $C_{14} = C_{15} = C_{24} = C_{25} = C_{34} = C_{35} = C_{46} = C_{56} = 0$. Extending the unique plane of symmetry in triclinic solids, an orthotropic solid has three mutually orthogonal planes of symmetry, leading to 9 independent elastic constants, where normal stresses are decoupled from the shear strains, and vice-versa.

Moreover, in transversely poled orthotropic piezoelectric materials, where the transverse x_3-direction is the poling direction, the piezoelectric coefficients tensor has only 5 nonzero components (e_{31}, e_{32}, e_{33}, e_{24} and e_{15}) and the dielectric tensor 3 independent components (ϵ_{11}, ϵ_{22} and ϵ_{33}). According to Baillargeon et al. [15], in the case of axially poled piezoelectric materials, the only nonzero piezoelectric

coefficients are $e_{11},\ e_{12},\ e_{13},\ e_{35}$ and e_{26} when x_1-axes is the poling direction, likewise $e_{21},\ e_{22},\ e_{23},\ e_{34}$ and e_{16} in the case of being x_2-axes the poling direction. Consequently, for a thickness-poled piezoelectric orthotropic material, the constitutive equations (2.11) reduce to,

$$\begin{Bmatrix}\sigma_1\\ \sigma_2\\ \sigma_3\\ \sigma_4\\ \sigma_5\\ \sigma_6\end{Bmatrix} = \begin{bmatrix}C_{11} & C_{12} & C_{13} & 0 & 0 & 0\\ C_{21} & C_{22} & C_{23} & 0 & 0 & 0\\ C_{31} & C_{32} & C_{33} & 0 & 0 & 0\\ 0 & 0 & 0 & C_{44} & 0 & 0\\ 0 & 0 & 0 & 0 & C_{55} & 0\\ 0 & 0 & 0 & 0 & 0 & C_{66}\end{bmatrix} \begin{Bmatrix}\varepsilon_1\\ \varepsilon_2\\ \varepsilon_3\\ \varepsilon_4\\ \varepsilon_5\\ \varepsilon_6\end{Bmatrix} - \begin{bmatrix}0 & 0 & e_{31}\\ 0 & 0 & e_{32}\\ 0 & 0 & e_{33}\\ 0 & e_{24} & 0\\ e_{15} & 0 & 0\\ 0 & 0 & e_{36}\end{bmatrix} \begin{Bmatrix}E_1\\ E_2\\ E_3\end{Bmatrix} \tag{2.12}$$

$$\begin{Bmatrix}D_1\\ D_2\\ D_3\end{Bmatrix} = \begin{bmatrix}0 & 0 & 0 & 0 & e_{15} & 0\\ 0 & 0 & 0 & e_{24} & 0 & 0\\ e_{31} & e_{32} & e_{33} & 0 & 0 & e_{36}\end{bmatrix} \begin{Bmatrix}\varepsilon_1\\ \varepsilon_2\\ \varepsilon_3\\ \varepsilon_4\\ \varepsilon_5\\ \varepsilon_6\end{Bmatrix} + \begin{bmatrix}\epsilon_{11} & 0 & 0\\ 0 & \epsilon_{22} & 0\\ 0 & 0 & \epsilon_{33}\end{bmatrix} \begin{Bmatrix}E_1\\ E_2\\ E_3\end{Bmatrix}$$

For an orthotropic material, the elastic constants C_{ij} can be calculated using the so-called engineering constants, namely the Young's modulus with respect to the three cartesian directions ($E_1,\ E_2$ and E_3), the shear moduli G_{ij} on the three x_i-x_j planes, with $i \neq j$ ($G_{12},\ G_{13}$ and G_{23}), likewise the Poisson's coefficients for the same x_i-x_j planes ($\nu_{12},\ \nu_{13}$ and ν_{23}). One must pay attention to the nomenclature used for the electric field components and Young's modulus, where the same letter is used for both variables, since no equation is explicitly presented relating both of them. According to Reddy [17], the elastic constants C_{ij} are given by:

$$\begin{aligned}
&C_{11} = \frac{1-\nu_{23}\nu_{32}}{E_2E_3\Delta}\ ,\ C_{12} = \frac{\nu_{21}+\nu_{31}\nu_{23}}{E_2E_3\Delta}\ ,\ C_{22} = \frac{1-\nu_{13}\nu_{31}}{E_1E_3\Delta}\\
&C_{13} = \frac{\nu_{13}+\nu_{12}\nu_{23}}{E_1E_2\Delta}\ ,\ C_{23} = \frac{\nu_{32}+\nu_{12}\nu_{31}}{E_1E_3\Delta}\ ,\ C_{33} = \frac{1-\nu_{12}\nu_{21}}{E_1E_2\Delta}\\
&C_{44} = G_{23}\ ,\ C_{55} = G_{13}\ ,\ C_{66} = G_{12}\\
&\Delta = \frac{1-\nu_{12}\nu_{21}-\nu_{23}\nu_{32}-\nu_{31}\nu_{13}-2\nu_{21}\nu_{32}\nu_{13}}{E_1E_2E_3}
\end{aligned} \tag{2.13}$$

Also, from the symmetric properties of the compliance tensor (the inverse of the elastic tensor), one obtains the relation between the Poisson's coefficients and the Young's modulus, for $i,j = \{1,2,3\}$ and $i \neq j$, as follows:

$$\frac{\nu_{ij}}{E_i} = \frac{\nu_{ji}}{E_j} \tag{2.14}$$

In the case where the material has an infinite number of planes of symmetry, the orthotropic material reduces to an isotropic one, in which the properties are independent on the direction. Isotropic materials have two independent elastic constants, the Lamé's constants (λ and μ) or two of the three engineering

constants can be chosen: E the Young's moduli, ν the Poisson's coefficient and G the shear moduli. The classic relation between these variables can also be found in Reddy [17]. It can be noticed that in an isotropic material the dielectric tensor has only one independent component and the piezoelectric effect cannot exist, i.e., $e_{ijk} = 0$, because the Lévi-Civita symbol (or permutation symbol) is skew-symmetric, as explained in Campos et al. [5]. A particular case can be found when an orthotropic solid, in which an orthotropic principal axis is a symmetry axis, is isotropic in the orthogonal plane to that axis, the so-called transversely isotropic material.

One last simplification can be introduced by considering a plane stress state, which is the typical scenario of thin and moderately thick multilayered plates, where the transverse direct stresses can be neglected. Considering a certain layer in the x_1-x_2 plane, being the x_3-direction the thickness direction, the plane stress state is achieved by forcing the transverse direct stress to be zero, $\sigma_3 = \sigma_{33} = 0$, leading to the plane stress piezoelectric constitutive equations for orthotropic materials as following:

$$\begin{Bmatrix} \sigma_{11} \\ \sigma_{22} \\ \sigma_{23} \\ \sigma_{13} \\ \sigma_{12} \end{Bmatrix} = \begin{bmatrix} Q_{11} & Q_{12} & 0 & 0 & 0 \\ Q_{12} & Q_{22} & 0 & 0 & 0 \\ 0 & 0 & Q_{44} & 0 & 0 \\ 0 & 0 & 0 & Q_{55} & 0 \\ 0 & 0 & 0 & 0 & Q_{66} \end{bmatrix} \begin{Bmatrix} \varepsilon_{11} \\ \varepsilon_{22} \\ \gamma_{23} \\ \gamma_{13} \\ \gamma_{12} \end{Bmatrix} - \begin{bmatrix} 0 & 0 & e_{31}^* \\ 0 & 0 & e_{32}^* \\ 0 & e_{24} & 0 \\ e_{15} & 0 & 0 \\ 0 & 0 & 0 \end{bmatrix} \begin{Bmatrix} E_1 \\ E_2 \\ E_3 \end{Bmatrix}$$

$$\begin{Bmatrix} D_1 \\ D_2 \\ D_3 \end{Bmatrix} = \begin{bmatrix} 0 & 0 & 0 & e_{15} & 0 \\ 0 & 0 & e_{24} & 0 & 0 \\ e_{31}^* & e_{32}^* & 0 & 0 & 0 \end{bmatrix} \begin{Bmatrix} \varepsilon_{11} \\ \varepsilon_{22} \\ \gamma_{23} \\ \gamma_{13} \\ \gamma_{12} \end{Bmatrix} + \begin{bmatrix} \epsilon_{11} & 0 & 0 \\ 0 & \epsilon_{22} & 0 \\ 0 & 0 & \epsilon_{33}^* \end{bmatrix} \begin{Bmatrix} E_1 \\ E_2 \\ E_3 \end{Bmatrix} \tag{2.15}$$

The new material properties presented in the plane stress constitutive law (2.15) are reduced plane stress elastic constants Q_{ij}, reduced piezoelectric coefficients e_{ij}^* and reduced dielectric constants ϵ_{ij}^* for the constitutive equations (2.12). The reduced plane stress properties are obtained, according to Araújo et al. [37], as:

$$Q_{ij} = C_{ij} - \frac{C_{i3}C_{j3}}{C_{33}}, \;\; i,j = \{1,2\} \tag{2.16a}$$

$$Q_{44} = C_{44} \; , \; Q_{55} = C_{55} \; , \; Q_{66} = C_{66} \tag{2.16b}$$

$$e_{3i}^* = e_{3i} - e_{33}\frac{C_{i3}}{C_{33}}, \;\; i,j = \{1,2\} \tag{2.16c}$$

$$\epsilon_{33}^* = \epsilon_{33} + \frac{e_{33}^2}{C_{33}} \tag{2.16d}$$

So far, the already presented constitutive laws are written on the material coordinate system (x_1, x_2, x_3), figure 2.1. In order to use the global coordinate system (x, y, z) basis, a rotation on the plane must be applied to the constitutive matrices in order to obtain the piezoelectric constitutive law written in the

global coordinate system, as following:

$$\begin{Bmatrix} \sigma_{xx} \\ \sigma_{yy} \\ \tau_{yz} \\ \tau_{xz} \\ \tau_{xy} \end{Bmatrix} = \begin{bmatrix} \bar{Q}_{11} & \bar{Q}_{12} & 0 & 0 & \bar{Q}_{16} \\ \bar{Q}_{12} & \bar{Q}_{22} & 0 & 0 & \bar{Q}_{26} \\ 0 & 0 & \bar{Q}_{44} & \bar{Q}_{45} & 0 \\ 0 & 0 & \bar{Q}_{45} & \bar{Q}_{55} & 0 \\ \bar{Q}_{16} & \bar{Q}_{26} & 0 & 0 & \bar{Q}_{66} \end{bmatrix} \begin{Bmatrix} \varepsilon_{xx} \\ \varepsilon_{yy} \\ \gamma_{yz} \\ \gamma_{xz} \\ \gamma_{xy} \end{Bmatrix} - \begin{bmatrix} 0 & 0 & \bar{e}_{31} \\ 0 & 0 & \bar{e}_{32} \\ \bar{e}_{14} & \bar{e}_{24} & 0 \\ \bar{e}_{15} & \bar{e}_{25} & 0 \\ 0 & 0 & \bar{e}_{36} \end{bmatrix} \begin{Bmatrix} E_x \\ E_y \\ E_z \end{Bmatrix}$$

$$\begin{Bmatrix} D_x \\ D_y \\ D_z \end{Bmatrix} = \begin{bmatrix} 0 & 0 & \bar{e}_{14} & \bar{e}_{15} & 0 \\ 0 & 0 & \bar{e}_{24} & \bar{e}_{25} & 0 \\ \bar{e}_{31} & \bar{e}_{32} & 0 & 0 & \bar{e}_{36} \end{bmatrix} \begin{Bmatrix} \varepsilon_{xx} \\ \varepsilon_{yy} \\ \gamma_{yz} \\ \gamma_{xz} \\ \gamma_{xy} \end{Bmatrix} + \begin{bmatrix} \epsilon_{xx} & \epsilon_{xy} & 0 \\ \epsilon_{xy} & \epsilon_{yy} & 0 \\ 0 & 0 & \epsilon_{zz} \end{bmatrix} \begin{Bmatrix} E_x \\ E_y \\ E_z \end{Bmatrix} \tag{2.17}$$

or using compact invariant notation as,

$$\begin{aligned} \{\sigma\} &= \left[\bar{Q}\right]\{\varepsilon\} - [\bar{e}]\{E\} \\ \{D\} &= [\bar{e}]^T\{\varepsilon\} + [\bar{\epsilon}]\{E\} \end{aligned} \tag{2.18}$$

where the transformed elastic properties $\bar{Q}_{ij}$ in the $[\bar{Q}]$ matrix are derived from the application of a rotation matrix of an angle θ, on the x-y plane, to change the basis where the the strains and the stresses are written, as explained in Reddy's book [17], leading to,

$$\bar{Q}_{11} = Q_{11}\cos^4\theta + 2\left(Q_{12} + 2Q_{66}\right)\sin^2\theta\cos^2\theta + Q_{22}\sin^4\theta \tag{2.19a}$$

$$\bar{Q}_{22} = Q_{11}\sin^4\theta + 2\left(Q_{12} + 2Q_{66}\right)\sin^2\theta\cos^2\theta + Q_{22}\cos^4\theta \tag{2.19b}$$

$$\bar{Q}_{12} = \left(Q_{11} + Q_{22} - 4Q_{66}\right)\sin^2\theta\cos^2\theta + Q_{12}(\sin^4 + \cos^4) \tag{2.19c}$$

$$\bar{Q}_{16} = \left(Q_{11} - Q_{12} - 2Q_{66}\right)\sin\theta\cos^3\theta + \left(Q_{12} - Q_{22} + 2Q_{66}\right)\sin^3\theta\cos\theta \tag{2.19d}$$

$$\bar{Q}_{26} = \left(Q_{11} - Q_{12} - 2Q_{66}\right)\sin^3\theta\cos\theta + \left(Q_{12} - Q_{22} + 2Q_{66}\right)\sin\theta\cos^3\theta \tag{2.19e}$$

$$\bar{Q}_{66} = \left(Q_{11} + Q_{22} - 2Q_{12} - 2Q_{66}\right)\sin^2\theta\cos^2\theta + Q_{66}\left(\sin^4\theta\ + cos^4\theta\right) \tag{2.19f}$$

$$\bar{Q}_{44} = Q_{44}\cos^2\theta + Q_{55}\sin^2\theta\ ,\ \bar{Q}_{45} = \left(Q_{55} - Q_{44}\right)\cos\theta\sin\theta \tag{2.19g}$$

$$\bar{Q}_{55} = Q_{55}\cos^2\theta + Q_{44}\sin^2\theta \tag{2.19h}$$

Likewise, the rotated piezoelectric coefficients $\bar{e}_{ij}$ and dielectric constants ϵ_{ij}, respectively in $[\bar{e}]$ and $[\bar{\epsilon}]$ matrices, are given, according to Reddy's book [17], as follows:

$$\bar{e}_{31} = e^*_{31}\cos^2\theta + e^*_{32}\sin^2\theta\ ,\ \bar{e}_{32} = e^*_{32}\cos^2\theta + e^*_{31}\sin^2\theta \tag{2.20a}$$

$$\bar{e}_{36} = (e^*_{31} - e^*_{32})\sin\theta\cos\theta\ ,\ \bar{e}_{14} = (e_{15} - e_{24})\sin\theta\cos\theta \tag{2.20b}$$

$$\bar{e}_{24} = e_{24}\cos^2\theta + e_{15}\sin^2\theta\ ,\ \bar{e}_{15} = e_{15}\cos^2\theta + e_{24}\sin^2\theta \tag{2.20c}$$

$$\bar{e}_{25} = (e_{15} - e_{24})\sin\theta\cos\theta\ ,\ \epsilon_{xx} = \epsilon_{11}\cos^2\theta + \epsilon_{22}\sin^2\theta \tag{2.20d}$$

$$\epsilon_{yy} = \epsilon_{22}\cos^2\theta + \epsilon_{11}\sin^2\theta\ ,\ \epsilon_{xy} = (\epsilon_{11} - \epsilon_{22})\sin\theta\cos\theta \tag{2.20e}$$

$$\epsilon_{zz} = \epsilon^*_{33} \tag{2.20f}$$

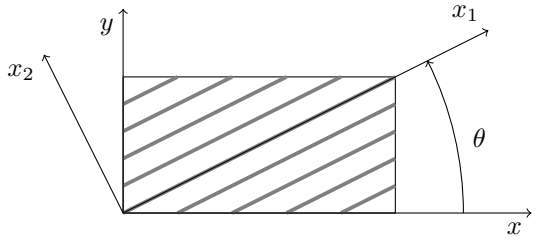

Figure 2.1: Material coordinate system (x_1, x_2) and global one (x, y).

2.2 Fundamental Electro-Elastic Equations

Fundamental electro-elastic equations can be derived recalling the equilibrium equations for elastic continuum bodies and dielectric continuum domains. In the mechanical domain, a compatible stress state and displacement field must verify the equilibrium conditions, while in the electrical domain, the conservation of electric charge equation of electrostatics must be respected.

The fundamental differential equations of motion for an elastic body, the so-called equilibrium equations, are achieved using a linear momentum balance to an infinitesimal piece of volume within the body volume domain Ω, subjected to an arbitrary volume force f. Following Reddy [17], the equilibrium equation in the i-direction, in terms of the Cauchy stress tensor σ_{ij} and the displacement field u_i holds,

$$\frac{\partial \sigma_{ij}}{\partial x_j} + f_i = \rho\frac{\partial^2 u_i}{\partial t^2} \quad \text{on } \Omega \tag{2.21}$$

From the electrostatics point of view, the Gauss law for the electric displacement field, which express the equilibrium of free charges, is valid over the continuum piezoelectric medium [38], and in the absence of volumetric distributed free charges is written as:

$$\frac{\partial D_i}{\partial x_i} = 0 \quad \text{on } \Omega \tag{2.22}$$

Substituting the constitutive equations (2.8), the strain-displacement equations (2.2) and the field-potential (2.6) equations into the equations of motion (2.21) and the charge equation (2.22), the govern-

ing differential equations for piezoelectric materials follow as,

$$\frac{1}{2}C_{ijkl}\left(\frac{\partial^2 u_k}{\partial x_j \partial x_l}+\frac{\partial^2 u_l}{\partial x_j \partial x_k}\right)+e_{ijk}\frac{\partial^2 \phi}{\partial x_j \partial x_k}+f_i=\rho\frac{\partial^2 u_i}{\partial t^2} \quad \text{on } \Omega \tag{2.23}$$

$$\epsilon_{ij}\frac{\partial^2 \phi}{\partial x_i \partial x_j}-\frac{1}{2}e_{jki}\left(\frac{\partial^2 u_k}{\partial x_i \partial x_j}+\frac{\partial^2 u_j}{\partial x_i \partial x_k}\right)=0 \quad \text{on } \Omega \tag{2.24}$$

representing a set of four coupled partial differential equations, which relate the typical cartesian displacement field components $(u_1, u_2, u_3) \equiv (u, v, w)$ and the electric potential ϕ.

Heyliger's exact solutions [2, 9, 10] for simply-supported multilayered piezoelectric composite plates represent an exact approach to solve the coupled partial differential equations (2.23) and (2.24), for transversely poled orthotropic materials, when a bi-sinusoidal transverse distributed load or a bi-sinusoidal electric potential is applied, in the absence of volume forces. The fundamental differential equations must be equipped with essential boundary conditions along with continuity conditions for the displacements, electric potential, transverse stresses and transverse electric displacement at the layers interfaces.

In order to obtain an integral form, also known as weak formulation, of the fundamental piezoelectric equations, both equilibrium equations (2.23) and charge conservation equation (2.24) must be added and integrated over the volume in order to express the balance of the system's energy. According to Benjeddou [20], for an arbitrary admissible variation of displacement δu_i and an admissible variation of electric potential $\delta\phi$ (i.e. both in line with the essential boundary conditions), equations (2.21) and (2.22) are equivalent to:

$$\int_\Omega \left(\frac{\partial \sigma_{ij}}{\partial x_j}+f_i-\rho\frac{\partial^2 u_i}{\partial t^2}\right)\delta u_i+\frac{\partial D_i}{\partial x_i}\delta\phi \; d\Omega=0 \tag{2.25}$$

The weak formulation for the piezoelectric differential equations (2.23) and (2.24) is fully derived in the Appendix B, using equation (2.25). Briefly, the integration by parts method and the divergence theorem must be used to highlight the stress boundary conditions on the imposed stress surface S_t and also the charge boundary conditions imposed on the surface $S_\mathcal{Q}$. Further, the symmetric property of the stress tensor must be used, along with the piezoelectric constitutive equations (2.8). To express the variational formulation in terms of displacements and electric potential, the linear strain tensor definition in equation (2.2) must be applied, along with the electric field-potential relation (2.6). Following this, one obtains the piezoelectric variational principle as,

$$\begin{aligned} 0=\int_\Omega & -C_{ijkl}\varepsilon_{kl}\delta\varepsilon_{ij}+e_{ijk}E_k\delta\varepsilon_{ij}+e_{jki}\varepsilon_{jk}\delta E_i+\epsilon_{ij}E_j\delta E_i+f_i\delta u_i-\rho\frac{\partial^2 u_i}{\partial t^2}\delta u_i \; d\Omega \\ & +\int_{S_t} t_i^s \delta u_i dA+\int_{S_\mathcal{Q}} \mathcal{Q}^s\delta\phi \; dA \end{aligned} \tag{2.26}$$

where the natural boundary conditions are $t_i^s=\sigma_{ij}n_j$, the prescribed surface traction in S_t, and $\mathcal{Q}^s = D_i n_i$, the imposed surface charge (including the minus sign) in $S_\mathcal{Q}$, knowing that n_i are the surfaces outward unit normal vector components.

This approach can also be used in order to extended the Hamilton's principle (2.27), and to define the kinetic energy T, the electromechanical energy U and the work done by the external forces and charges W. The Hamilton's principle concerns the integral of action between two time steps t_1 and t_2

and is written in terms of the Lagrangian function $\mathcal{L} = T - V$ as,

$$\delta \int_{t_1}^{t_2} \mathcal{L} dt = \delta \int_{t_1}^{t_2} T - V dt = 0 \tag{2.27}$$

where $V = U + W$ is the total potential energy and δ, the variational operator. According to Benjeddou [20], the kinetic energy T, the electromechanical energy U and the external work W are given by:

$$T = \frac{1}{2} \int_{\Omega} \rho \dot{u}_i \dot{u}_i \, d\Omega \tag{2.28}$$

$$U = \frac{1}{2} \int_{\Omega} (\sigma_{ij} \varepsilon_{ij} - D_i E_i) \, d\Omega \tag{2.29}$$

$$W = \int_{\Omega} f_i u_i d\Omega + \int_{S_t} t_i^s u_i dS_t + \int_{S_{\mathcal{Q}}} \mathcal{Q}^s dS_{\mathcal{Q}} \tag{2.30}$$

At this moment, one could think of an analogy between the primary and secondary variables of the mechanical and electrical domains as presented in table 2.1, along with the associated S.I. units.

Table 2.1: Mechanical and electrical variables: analogy and S.I. units

Mechanical	Electrical
Displacement: u (m)	Electric potential: ϕ (V)
Strain: ε (-)	Electric Field: E (V/m)
Stress: σ (Pa)	Electric Displacement: D (C/m^2)
Concentrated Force: f (N)	Concentrated Charge: $\mathcal{Q}$ (C)

2.3 Piezoelectric Multilayered Composite Plates Modelling

Concerning the modelling and analysis of piezoelectric multilayered composite plates, axiomatic theories based on generalized displacements, typically shear deformation theories, are the most simple and intuitive approach to modelling the kinematics of these types of adaptive smart structures. In this scope, and considering the case of arbitrary piezoelectric layers, ESL and discrete LW theories represent the possible choices for the description of the displacements and the electric potential. Even when considering only piezoelectric face layers, i.e., in the absence of embedded sensors or actuators, the exact solutions exhibit a zig-zag through-thickness continuous evolution for the primary variables between the multilayered composite core and the piezoelectric face layers, schematically represented in figure 2.2.

Consequently, discrete LW classical theories, which *a priori* satisfy the C_z^0-requirements for the displacements and electric potential, should be more accurate for the analysis of piezoelectric composite plates than ESL theories. Moreover, since in LW models each layer is treated individually, the number of unknown variables depends on the number of layers in the stacking scheme, pushing forward in complexity comparatively to ESL models, where the unknown variables are introduced for the whole plate.

In order to keep a discrete LW model for piezoelectric composite plates the most simple possible, one could consider the case where only piezoelectric face layers are present, bounding the top and bottom surfaces of a multilayered composite core, which is described using the ESL theory. By doing this,

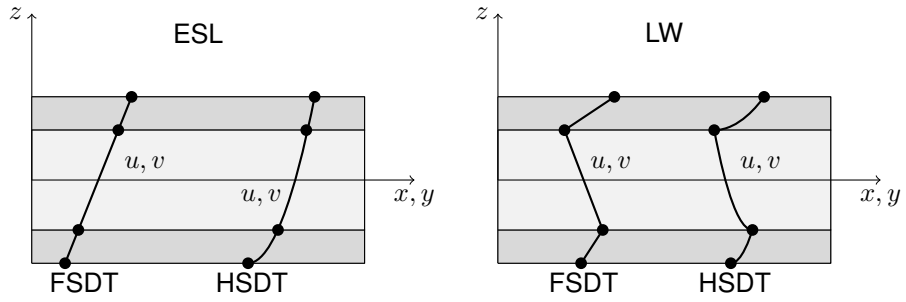

Figure 2.2: Equivalent Single Layer theory vs. Layerwise theory.

only three discrete layers are considered, bottom (b), core (c) and top (t) layers (figure 2.4), avoiding a generalized LW description of an arbitrary number of layers, while keeping a low number of unknown variables, as well as a reasonably accurate kinematic description.

Further, for each k-discrete layer, with $k = \{b, c, t\}$, following Reddy's book [17], the displacement field $(u^{(k)}, u^{(k)}, w^{(k)})$ could take the axiomatic description of the classical theory (CLPT), present in equation (2.31), or alternatively the first-order theory (FSDT) displacement field in equation (2.32), or even for a more accurate description, an higher-order theory (HSDT), represented in equation (2.33), could be used (see figure 2.3). Other refined theories can be found in the literature, as can be seen in the review by Li [22] or in the modified-HSDT reported by Mantari and Guedes Soares [32]. Independently of the chosen axiomatic theory, the LW model for three discrete layers must account for the interlaminar C_z^0-requirements for the displacement field, as well as for the electric potential. Hence, the compatibility conditions must be established at the layer's interfaces (bottom-core and core-top) in order to *a priori* fulfill the through-thickness continuity conditions for the primary variables.

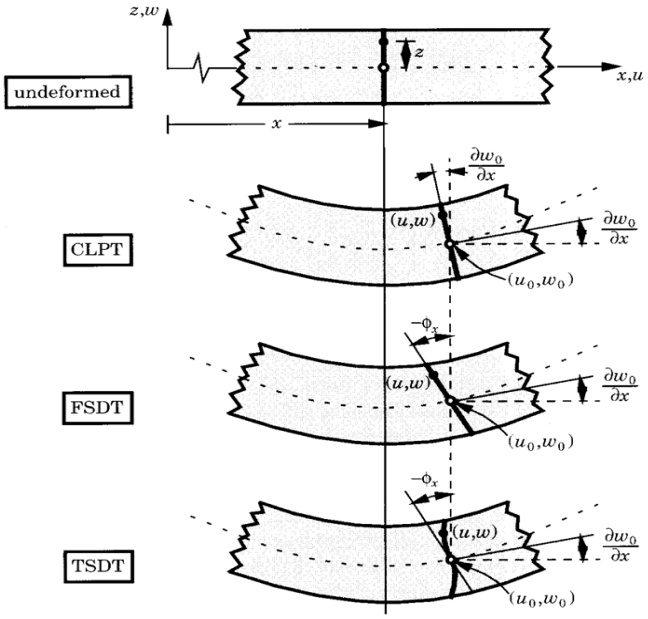

Figure 2.3: Undeformed and deformed configurations of a transverse normal according to the classical, first-order and third-order plate theories, from Reddy [17].

Moreover, the displacement field associated to the classical theory (CLPT) in equation (2.31), doesn't

account for shear strains and is typically valid in thin structures, where the side-to-thickness ratios, a/h and b/h, are higher then 100. Also, the classic theory is based on the Kirchhoff hypothesis, namely:

1. Straight lines orthogonal to the mid-surface, i.e, transverse normals, before deformation remain straight after deformation.

2. The transverse normals are inextensible.

3. The transverse normals rotate in a way that they remain orthogonal to the mid-surface after deformation.

From the first two hypothesis, the plate's thickness remains unchanged, hence the transverse normal strains ε_{zz} are null, leading to a constant through-thickness transverse displacement. The third hypothesis is the one that implies null transverse shear strains, γ_{xz} and γ_{yz}, providing a theory without transverse shear deformation mechanisms.

For an arbitrary k-layer within a multilayered plate, the Kirchhoff hypothesis holds the CLPT displacement field as follows,

$$\begin{aligned} u^{(k)}(x,y,z_k,t) &= u_0^{(k)}(x,y,t) - z_k \frac{\partial w_0^{(k)}}{\partial x}(x,y,t) \\ v^{(k)}(x,y,z_k,t) &= v_0^{(k)}(x,y,t) - z_k \frac{\partial w_0^{(k)}}{\partial y}(x,y,t) \\ w^{(k)}(x,y,z_k,t) &= w_0^{(k)}(x,y,t) \end{aligned} \tag{2.31}$$

where the generalized displacements $(u_0^{(k)}, v_0^{(k)}, w_0^{(k)})$ are the cartesian displacement components for the k-layer's mid-plane ($z_k = 0$), being z_k the layer's transverse coordinate, as can be seen in figure 2.4.

In order to introduce shear effects, the Kirchhoff's third hypothesis could be relaxed, eliminating the orthogonality condition. Improving the accuracy of the classical theory for moderately thick laminates $(a/h > 20)$, the first-order shear deformation theory (FSDT) is formulated by introducing the unknown rotations of the normals to the mid-plane of the k-layer as shown in figure 2.3. Geometrically, one could obtain the FSDT displacement field as follows,

$$\begin{aligned} u^{(k)}(x,y,z_k,t) &= u_0^{(k)}(x,y,t) + z_k \theta_x^{(k)}(x,y,t) \\ v^{(k)}(x,y,z_k,t) &= v_0^{(k)}(x,y,t) + z_k \theta_y^{(k)}(x,y,t) \\ w^{(k)}(x,y,z_k,t) &= w_0^{(k)}(x,y,t) \end{aligned} \tag{2.32}$$

where the linear z-expansion coefficients of the in-plane displacements are $\theta_x^{(k)}$ and $\theta_y^{(k)}$, the rotations about the y-axes (anticlockwise) and x-axes (clockwise), respectively. Consequently, the in-plane strains $(\varepsilon_{xx}^{(k)}, \varepsilon_{yy}^{(k)}, \gamma_{xy}^{(k)})$ are through-thickness linear, while fictitious constant transverse shear strains $(\gamma_{yz}^{(k)}, \gamma_{xz}^{(k)})$ are assumed.

From this gross hypothesis, a shear correction factor K_s must be taken into account for the consequent discrepancy between the real transverse shear stress state and the constant one, predicted by the first-order theory. Also, K_s minimizes the difference from the FSDT shear strain energy and the exact three-dimensional one. Such determination is a complex task since for an arbitrary multilayered

composite plate, the shear correction factor depends on the stacking sequence, geometric parameters, material properties as well as on the loading and boundary conditions.

A better kinematic description might be achieved using higher-order theories (HSDT), namely for thick plates $(a/h < 10)$, where higher-order z-expansions for the in-plane displacements are used. In this scope, the third-order shear deformation theories (TSDT) are achieved by relaxing the straightness and orthogonality of the first two Kirchhoff hypothesis for the transverse normals accomplished by a cubic expansion of the in-plane displacements as follows,

$$\begin{aligned} u^{(k)}(x,y,z_k,t) &= u_0^{(k)}(x,y,t) + z_k\theta_x^{(k)}(x,y,t) + z_k^2\chi_x^{(k)}(x,y,t) + z_k^3\lambda_x^{(k)}(x,y,t) \\ v^{(k)}(x,y,z_k,t) &= v_0^{(k)}(x,y,t) + z_k\theta_y^{(k)}(x,y,t) + z_k^2\chi_y^{(k)}(x,y,t) + z_k^3\lambda_y^{(k)}(x,y,t) \\ w^{(k)}(x,y,z_k,t) &= w_0^{(k)}(x,y,t) \end{aligned} \tag{2.33}$$

where the additional generalized displacements $(\chi_x^{(k)}, \chi_y^{(k)})$ and $(\lambda_x^{(k)}, \lambda_y^{(k)})$ are difficult to interpret geometrically. The displacement field in equation (2.33) provides a through-thickness cubic variation of the in-plane strains and stresses, while the correspondent transverse shear terms have a quadratic evolution. Hence, HSDT models do not require shear corrections factors, yielding a more accurate distribution for the transverse shear stresses, in consequence of a more complex theory with greater computational needs.

A further reduction on the number of unknowns is achieved using an ESL description in which the TSDT displacement field is *a priori* forced to have vanishing transverse shear stresses on both top and bottom surfaces of the multilayered plate, leading to the so-called Reddy's TSDT [17].

Similarly to the displacement field, the electric potential could also be described using an axiomatic theory. The most simple case is a linear z-expansion, however and according to Benjeddou [20], this assumption systematically neglects the induced potential, leading to a partial electromechanical coupling, which is thought to be improved using a quadratic variation.

Expanding the electric potential in a Taylor series on the z-direction, the first order coefficient will be the symmetric of the transverse electric field, i.e, $\partial\phi/\partial z = -E_z$. The same happens if one expands the transverse displacement w, where the transverse normal strain $\varepsilon_{zz} = \partial w/\partial z$ is the first order coefficient. This type of unknowns, i.e., derivatives of primary variables, can only be used with Reissner's mixed formulations, as explained by Carrera [21].

In order to use an electric potential z-expansion based formulation, one could use the electric potential at various z-coordinates along the layer's thickness direction, such as the top surface potential ϕ_{sup} and the bottom one ϕ_{inf} for a linear z-expansion, or adding the mid-plane's potential ϕ_{mid} for a quadratic z-expansion, according to Polit et al. [30].

Hence, let $h_{(k)}$ be the thickness of an arbitrary k-layer in figure 2.4. One could obtain the linear z-expansion for the layer's electric potential $\phi_{(k)}$, in terms of the local transverse coordinate z_k as,

$$\phi_{(k)}(x,y,z_k,t) = \frac{1}{2}\left(\phi_{sup}^{(k)}(x,y,t) + \phi_{inf}^{(k)}(x,y,t)\right) + \frac{z_k}{h_{(k)}}\left(\phi_{sup}^{(k)}(x,y,t) - \phi_{inf}^{(k)}(x,y,t)\right) \tag{2.34}$$

where the consequent transverse electric field is independent on the transverse coordinate.

On the other hand, the quadratic z-expansion for the electric potential leads to a through-thickness linear transverse electric field, which is a more generalized and accurate assumption than the previous one. In compact notation, the second-order z-expansion of the electric potential is

$$\phi_{(k)}(x,y,z_k,t) = g_s^{(k)}(z_k)\phi_{sup}^{(k)}(x,y,t) + g_i^{(k)}(z_k)\phi_{inf}^{(k)}(x,y,t) + g_m^{(k)}(z_k)\phi_{mid}^{(k)}(x,y,t) \tag{2.35}$$

being the transverse coordinate functions $g_s(z_k),\ g_i(z_k)$ and $g_m(z_k)$ the one-dimensional quadratic Lagrange's functions, which for the present formulation are given by:

$$g_s^{(k)}(z_k) = 2\left(\frac{z_k}{h_{(k)}}\right)^2 + \frac{z_k}{h_{(k)}} \tag{2.36a}$$

$$g_i^{(k)}(z_k) = 2\left(\frac{z_k}{h_{(k)}}\right)^2 - \frac{z_k}{h_{(k)}} \tag{2.36b}$$

$$g_m^{(k)}(z_k) = 1 - 4\left(\frac{z_k}{h_{(k)}}\right)^2 \tag{2.36c}$$

The local transverse coordinate z_k is related to the global one z through the following translation:

$$z_k = z - \bar{z}_k \tag{2.37}$$

where $\bar{z}_k$ is the transverse coordinate of the k-layer's mid-plane in the global coordinate system.

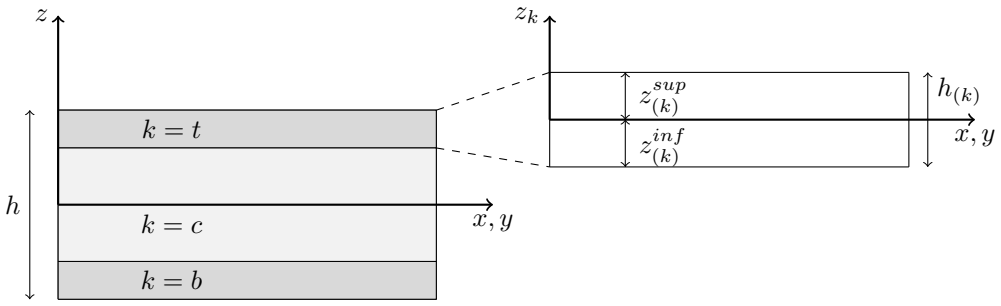

Figure 2.4: Generic k-layer coordinate system (x, y, z_k).

Chapter 3

Layerwise Model

In the following chapter, a discrete LW model for three discrete layers is formulated for analysis of piezoelectric multilayered composite plates, with a displacement field based on FSDT assumptions, combined with linear or quadratic z-expansions for the electric potential in each layer. The assumed stacking sequence is made of piezoelectric face layers bounding a multilayered composite core, which is treated as an equivalent single layer. The interlaminar continuity conditions at the interfaces between the discrete layers are employed to formulate a displacement field and electric potential that fulfill the C_z^0-requirements.

3.1 Layerwise Displacement Field

The layerwise displacement field is developed for a model with three discrete layers, driven by the assumption of a multilayered composite plate with piezoelectric face layers (figure 3.1), where no slip occurs at the interfaces between layers. The composite core (c), as well as the piezoelectric top (t) and bottom (b) layers, are modelled using the displacement field of the first-order theory in equation (2.32).

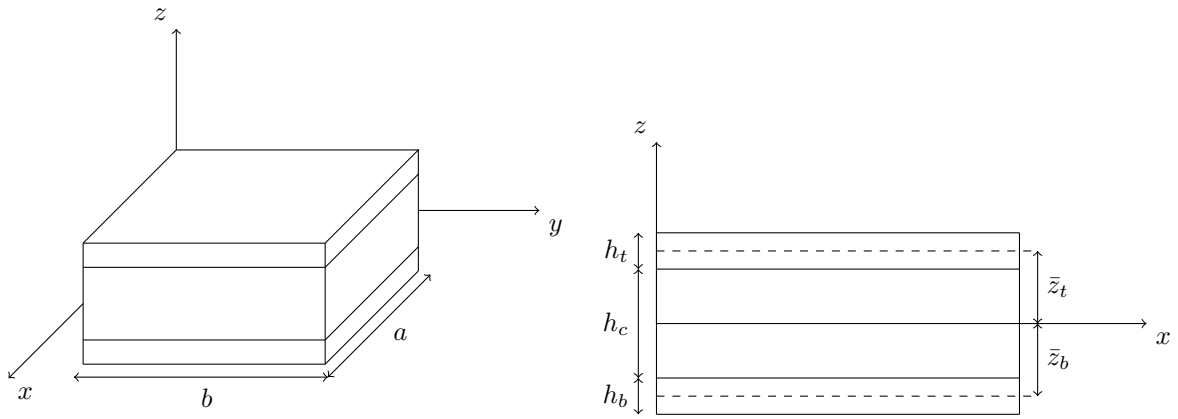

Figure 3.1: Piezoelectric composite plate and geometric parameters.

Following the assumed stacking sequence of discrete layers and the geometric parameters repre-

sented in figure 3.1, the FSDT displacement field for the multilayered composite core is given by,

$$\begin{aligned} u_c(x,y,z,t) &= u_{0_c}(x,y,t) + z\theta_{x_c}(x,y,t) \\ v_c(x,y,z,t) &= v_{0_c}(x,y,t) + z\theta_{y_c}(x,y,t) \\ w_c(x,y,z,t) &= w_{0_c}(x,y,t) \end{aligned} \tag{3.1}$$

likewise for the piezoelectric top layer as,

$$\begin{aligned} u_t(x,y,z,t) &= u_{0_t}(x,y,t) + (z-\bar{z}_t)\theta_{x_t}(x,y,t) \\ v_t(x,y,z,t) &= v_{0_t}(x,y,t) + (z-\bar{z}_t)\theta_{y_t}(x,y,t) \\ w_t(x,y,z,t) &= w_{0_t}(x,y,t) \end{aligned} \tag{3.2}$$

and for the piezoelectric bottom layer as,

$$\begin{aligned} u_b(x,y,z,t) &= u_{0_b}(x,y,t) + (z-\bar{z}_b)\theta_{x_b}(x,y,t) \\ v_b(x,y,z,t) &= v_{0_b}(x,y,t) + (z-\bar{z}_b)\theta_{y_b}(x,y,t) \\ w_b(x,y,z,t) &= w_{0_b}(x,y,t) \end{aligned} \tag{3.3}$$

where $\bar{z}_t$ and $\bar{z}_b$ are the mid-plane transverse coordinates for both top and bottom layers with respect to the plate's mid-plane, respectively, defined as follows:

$$\bar{z}_t = \frac{h_c}{2} + \frac{h_t}{2}\ ,\ \bar{z}_b = -\frac{h_c}{2} - \frac{h_b}{2} \tag{3.4}$$

In order to fulfill the C_z^0-requirements for the displacements along the layer's interfaces, the interlaminar continuity conditions must be verified for all displacement components. Since the FSDT transverse displacement is assumed to be independent on the z-coordinate, the interlaminar continuity conditions for the transverse displacement leads to,

$$w_c(x,y,z,t) = w_t(x,y,z,t) = w_b(x,y,z,t) = w_0(x,y,t) \tag{3.5}$$

where w_0 represents the plate's mid-plane $(z=0)$ transverse displacement.

The continuity conditions for the in-plane displacements at the interfaces between the piezoelectric face layers and the composite core as follows,

$$u_c\left(x,y,\frac{h_c}{2},t\right) = u_t\left(x,y,\bar{z}_t - \frac{h_t}{2},t\right) \tag{3.6a}$$

$$v_c\left(x,y,\frac{h_c}{2},t\right) = v_t\left(x,y,\bar{z}_t - \frac{h_t}{2},t\right) \tag{3.6b}$$

$$u_c\left(x,y,-\frac{h_c}{2},t\right) = u_b\left(x,y,\bar{z}_b + \frac{h_b}{2},t\right) \tag{3.6c}$$

$$v_c\left(x,y,-\frac{h_c}{2},t\right) = v_b\left(x,y,\bar{z}_b + \frac{h_b}{2},t\right) \tag{3.6d}$$

allow to reduce the number of unknowns (generalized displacements) in the model by writing the rotations of both bottom and top layers, $(\theta_{x_b}, \theta_{y_b})$ and $(\theta_{x_t}, \theta_{y_t})$, respectively, as a function of the remaining unknowns.

Solving the continuity conditions (3.6) for the displacements defined in equations (3.1), (3.2) and (3.3), one obtains,

$$\theta_{x_t} = -\frac{2}{h_t}u_{0_c} - \frac{h_c}{h_t}\theta_{x_c} + \frac{2}{h_t}u_{0_t} \tag{3.7a}$$

$$\theta_{y_t} = -\frac{2}{h_t}v_{0_c} - \frac{h_c}{h_t}\theta_{y_c} + \frac{2}{h_t}v_{0_t} \tag{3.7b}$$

$$\theta_{x_b} = \frac{2}{h_b}u_{0_c} - \frac{h_c}{h_b}\theta_{x_c} - \frac{2}{h_b}u_{0_b} \tag{3.7c}$$

$$\theta_{y_b} = \frac{2}{h_b}v_{0_c} - \frac{h_c}{h_b}\theta_{y_c} - \frac{2}{h_b}v_{0_b} \tag{3.7d}$$

and defining the layerwise-constants α_k and β_k, with $k = \{1, 2, 3\}$ as,

$$\begin{Bmatrix} \alpha_1 \\ \alpha_2 \\ \alpha_3 \end{Bmatrix} = \frac{1}{h_t}\begin{Bmatrix} -2 \\ -h_c \\ 2 \end{Bmatrix}, \quad \begin{Bmatrix} \beta_1 \\ \beta_2 \\ \beta_3 \end{Bmatrix} = \frac{1}{h_b}\begin{Bmatrix} 2 \\ -h_c \\ -2 \end{Bmatrix} \tag{3.8}$$

the rotations in equation (3.7) can be written as shown:

$$\theta_{xt} = \alpha_1 u_{0_c} + \alpha_2\theta_{x_c} + \alpha_3 u_{0_t} \tag{3.9a}$$

$$\theta_{y_t} = \alpha_1 v_{0_c} + \alpha_2\theta_{y_c} + \alpha_3 v_{0_t} \tag{3.9b}$$

$$\theta_{xb} = \beta_1 u_{0_c} + \beta_2\theta_{x_c} + \beta_3 u_{0_b} \tag{3.9c}$$

$$\theta_{y_b} = \beta_1 v_{0_c} + \beta_2\theta_{y_c} + \beta_3 v_{0_b} \tag{3.9d}$$

Replacing the rotations in equation (3.7), for the top and bottom layers, in the respective displacement field in equations (3.2) and (3.3), respectively, one obtains the LW-FSDT in-plane displacements for the piezoelectric face layers as follows:

$$u_t = \left[1 + \frac{2(z-\bar{z}_t)}{h_t}\right]u_{0_t} - \frac{2(z-\bar{z}_t)}{h_t}u_{0_c} - \frac{h_c}{h_t}(z-\bar{z}_t)\theta_{x_c} \tag{3.10a}$$

$$v_t = \left[1 + \frac{2(z-\bar{z}_t)}{h_t}\right]v_{0_t} - \frac{2(z-\bar{z}_t)}{h_t}v_{0_c} - \frac{h_c}{h_t}(z-\bar{z}_t)\theta_{y_c} \tag{3.10b}$$

$$u_b = \left[1 - \frac{2(z-\bar{z}_b)}{h_b}\right]u_{0_b} + \frac{2(z-\bar{z}_b)}{h_b}u_{0_c} - \frac{h_c}{h_b}(z-\bar{z}_b)\theta_{x_c} \tag{3.10c}$$

$$v_b = \left[1 - \frac{2(z-\bar{z}_b)}{h_b}\right]v_{0_c} + \frac{2(z-\bar{z}_b)}{h_b}v_{0_c} - \frac{h_c}{h_b}(z-\bar{z}_b)\theta_{y_c} \tag{3.10d}$$

The transverse displacements of the three discrete layers are given in equation (3.5).

The relation between the displacement components for each k-discrete layer, for $k = \{c, t, b\}$, and the nine independent unknown mechanical variables, ordained in the vector of mechanical degrees of

freedom $\{d\}$ defined as,

$$\{d\} = \{u_{0_c}\ v_{0_c}\ w_0\ \theta_{x_c}\ \theta_{y_c}\ u_{0_t}\ v_{0_t}\ u_{0_b}\ v_{0_b}\}^T \tag{3.11}$$

is achieved through a matrix $[Z]_{(k)}$ which establishes,

$$\{u\}_{(k)} = \{u_{(k)}\ v_{(k)}\ w_{(k)}\}^T = [Z]_{(k)}\{d\} \tag{3.12}$$

where the $[Z]_{(k)}$ matrices, for the composite core, are derived from equation (3.1) in order to verify equation (3.12), leading to,

$$[Z]_c = \begin{bmatrix} 1 & 0 & 0 & z & 0 & 0 & 0 & 0 & 0 \\ 0 & 1 & 0 & 0 & z & 0 & 0 & 0 & 0 \\ 0 & 0 & 1 & 0 & 0 & 0 & 0 & 0 & 0 \end{bmatrix} \tag{3.13}$$

while for the top and bottom layers, one could use the layerwise constants defined in equation (3.8), as well as the modified displacements in equation (3.10) to derive:

$$[Z]_t = \begin{bmatrix} \alpha_1(z-\bar{z}_t) & 0 & 0 & \alpha_2(z-\bar{z}_t) & 0 & [1+\alpha_3(z-\bar{z}_t)] & 0 & 0 & 0 \\ 0 & \alpha_1(z-\bar{z}_t) & 0 & 0 & \alpha_2(z-\bar{z}_t) & 0 & [1+\alpha_3(z-\bar{z}_t)] & 0 & 0 \\ 0 & 0 & 1 & 0 & 0 & 0 & 0 & 0 & 0 \end{bmatrix} \tag{3.14}$$

$$[Z]_b = \begin{bmatrix} \beta_1(z-\bar{z}_b) & 0 & 0 & \beta_2(z-\bar{z}_b) & 0 & 0 & 0 & [1+\beta_3(z-\bar{z}_b)] & 0 \\ 0 & \beta_1(z-\bar{z}_b) & 0 & 0 & \beta_2(z-\bar{z}_b) & 0 & 0 & 0 & [1+\beta_3(z-\bar{z}_b)] \\ 0 & 0 & 1 & 0 & 0 & 0 & 0 & 0 & \end{bmatrix} \tag{3.15}$$

3.2 Layerwise Strain Field

From the infinitesimal strain tensor definition in equation (2.2), the nonzero linear strains associated with the assumed FSDT displacement field for an arbitrary k-layer in equation (2.32) are written in the global transverse coordinate z as shown,

$$\begin{aligned} \varepsilon_{xx}^{(k)} &= \frac{\partial u_0^{(k)}}{\partial x} + (z-\bar{z}_k)\frac{\partial \theta_x^{(k)}}{\partial x} \\ \varepsilon_{yy}^{(k)} &= \frac{\partial v_0^{(k)}}{\partial y} + (z-\bar{z}_k)\frac{\partial \theta_y^{(k)}}{\partial y} \\ \gamma_{xy}^{(k)} &= \frac{\partial u_0^{(k)}}{\partial y} + \frac{\partial v_0^{(k)}}{\partial x} + (z-\bar{z}_k)\left(\frac{\partial \theta_x^{(k)}}{\partial y} + \frac{\partial \theta_y^{(k)}}{\partial x}\right) \\ \gamma_{xz}^{(k)} &= \theta_x^{(k)} + \frac{\partial w_0}{\partial x} \\ \gamma_{yz}^{(k)} &= \theta_y^{(k)} + \frac{\partial w_0}{\partial y} \end{aligned} \tag{3.16}$$

where $\bar{z}_k$ is the transverse coordinate of the k-layer's mid-plane in the global coordinate system. Consequently, from the displacement field for the multilayered core in equation (3.1), one can obtain the

nonzero strains as follows:

$$\begin{aligned}
\varepsilon^c_{xx} &= \frac{\partial u_{0_c}}{\partial x} + z\frac{\partial \theta_{x_c}}{\partial x} \\
\varepsilon^c_{yy} &= \frac{\partial v_{0_c}}{\partial y} + z\frac{\partial \theta_{y_c}}{\partial y} \\
\gamma^c_{xy} &= \frac{\partial u_{0_c}}{\partial y} + \frac{\partial v_{0_c}}{\partial x} + z\left(\frac{\partial \theta_{x_c}}{\partial y} + \frac{\partial \theta_{y_c}}{\partial x}\right) \\
\gamma^c_{xz} &= \theta^c_x + \frac{\partial w_0}{\partial x} \\
\gamma^c_{yz} &= \theta^c_y + \frac{\partial w_0}{\partial y}
\end{aligned} \tag{3.17}$$

For the piezoelectric face layers, the rotation dependent terms in equation (3.16) (bending strain components) are expanded using the defined rotations in equation (3.9), as a function of the layerwise-constants α_i for the top layer and the β_i ones for the bottom layer given in equation (3.8). Hence, the LW strain field for the piezoelectric top layer is given by

$$\begin{aligned}
\varepsilon^t_{xx} &= \frac{\partial u_{0t}}{\partial x} + (z-\bar{z}_t)\left(\alpha_1\frac{\partial u_{0c}}{\partial x} + \alpha_2\frac{\partial \theta_{xc}}{\partial x} + \alpha_3\frac{\partial u_{0t}}{\partial x}\right) \\
\varepsilon^t_{yy} &= \frac{\partial v_{0t}}{\partial y} + (z-\bar{z}_t)\left(\alpha_1\frac{\partial v_{0c}}{\partial y} + \alpha_2\frac{\partial \theta_{y_c}}{\partial y} + \alpha_3\frac{\partial v_{0t}}{\partial y}\right) \\
\gamma^t_{xy} &= \frac{\partial u_{0t}}{\partial y} + \frac{\partial v_{0t}}{\partial x} + (z-\bar{z}_t)\left[\alpha_1\left(\frac{\partial v_{0c}}{\partial x} + \frac{\partial u_{0c}}{\partial y}\right) + \alpha_2\left(\frac{\partial \theta_{y_c}}{\partial x} + \frac{\partial \theta_{xc}}{\partial y}\right) + \alpha_3\left(\frac{\partial v_{0t}}{\partial x} + \frac{\partial u_{0t}}{\partial y}\right)\right] \\
\gamma^t_{xz} &= \alpha_1 u_{0c} + \alpha_2\theta_{x_c} + \alpha_3 u_{0t} + \frac{\partial w_0}{\partial x} \\
\gamma^t_{yz} &= \alpha_1 v_{0c} + \alpha_2\theta_{y_c} + \alpha_3 v_{0t} + \frac{\partial w_0}{\partial y}
\end{aligned} \tag{3.18}$$

while for the bottom layer by

$$\begin{aligned}
\varepsilon^b_{xx} &= \frac{\partial u_{0b}}{\partial x} + (z-\bar{z}_b)\left(\beta_1\frac{\partial u_{0c}}{\partial x} + \beta_2\frac{\partial \theta_{xc}}{\partial x} + \beta_3\frac{\partial u_{0b}}{\partial x}\right) \\
\varepsilon^b_{yy} &= \frac{\partial v_{0b}}{\partial y} + (z-\bar{z}_b)\left(\beta_1\frac{\partial v_{0c}}{\partial y} + \beta_2\frac{\partial \theta_{y_c}}{\partial y} + \beta_3\frac{\partial v_{0b}}{\partial y}\right) \\
\gamma^b_{xy} &= \frac{\partial u_{0b}}{\partial y} + \frac{\partial v_{0b}}{\partial x} + (z-\bar{z}_b)\left[\beta_1\left(\frac{\partial v_{0c}}{\partial x} + \frac{\partial u_{0c}}{\partial y}\right) + \beta_2\left(\frac{\partial \theta_{y_c}}{\partial x} + \frac{\partial \theta_{xc}}{\partial y}\right) + \beta_3\left(\frac{\partial v_{0b}}{\partial x} + \frac{\partial u_{0b}}{\partial y}\right)\right] \\
\gamma^b_{xz} &= \beta_1 u_{0c} + \beta_2\theta_{x_c} + \beta_3 u_{0t} + \frac{\partial w_0}{\partial x} \\
\gamma^b_{yz} &= \beta_1 v_{0c} + \beta_2\theta_{y_c} + \beta_3 v_{0t} + \frac{\partial w_0}{\partial y}
\end{aligned} \tag{3.19}$$

where the mid-plane coordinates $\bar{z}_t$ and $\bar{z}_b$ are given in equation (3.4).

The strain components in equations (3.17), (3.18) and (3.19) can be divided in z-independent strains, i.e., the generalized membrane strains $\{\hat{\varepsilon}_m\}$, while the z-dependent linear terms are the generalized bending strains $\{\hat{\varepsilon}_b\}$. For the transverse shear strains, the generalized shear strains $\{\hat{\varepsilon}_s\}$ for each discrete layer coincide with the natural ones, in the previous equations. Explicitly, for an arbitrary k-discrete layer, the generalized strain vector $\{\hat{\varepsilon}\}_{(k)}$ is defined as shown,

$$\{\hat{\varepsilon}\}_{(k)} = \left\{\{\hat{\varepsilon}_m\}^T_{(k)} \ \{\hat{\varepsilon}_b\}^T_{(k)} \ \{\hat{\varepsilon}_s\}^T_{(k)}\right\}^T \tag{3.20}$$

where the generalized strain components are:

$$\{\hat{\varepsilon}_m\}_{(k)} = \left\{ \frac{\partial u_0^{(k)}}{\partial x} \quad \frac{\partial v_0^{(k)}}{\partial y} \quad \frac{\partial u_0^{(k)}}{\partial y} + \frac{\partial v_0^{(k)}}{\partial x} \right\}^T \tag{3.21a}$$

$$\{\hat{\varepsilon}_b\}_{(k)} = \left\{ \frac{\partial \theta_x^{(k)}}{\partial x} \quad \frac{\partial \theta_y^{(k)}}{\partial y} \quad \left(\frac{\partial \theta_x^{(k)}}{\partial y} + \frac{\partial \theta_y^{(k)}}{\partial x} \right) \right\}^T \tag{3.21b}$$

$$\{\hat{\varepsilon}_s\}_{(k)} = \left\{ \theta_y^{(k)} + \frac{\partial w_0^{(k)}}{\partial y} \quad \theta_x^{(k)} + \frac{\partial w_0^{(k)}}{\partial x} \right\}^T \tag{3.21c}$$

The strain vector $\{\varepsilon\}_{(k)}$ for the k-discrete layer, following the Kelvin-Voigt notation (2.9), is computed using the generalized strain vector $\{\hat{\varepsilon}\}_{(k)}$ as,

$$\{\varepsilon\}_{(k)} = [S]_{(k)} \{\hat{\varepsilon}\}_{(k)} \tag{3.22}$$

where the strain transformation matrix $[S]_{(k)}$ for the k-discrete layer, with $k = \{t, c, b\}$, is given by:

$$[S]_{(k)} = \begin{bmatrix} 1 & 0 & 0 & (z - \bar{z}_k) & 0 & 0 & 0 & 0 \\ 0 & 1 & 0 & 0 & (z - \bar{z}_k) & 0 & 0 & 0 \\ 0 & 0 & 0 & 0 & 0 & 0 & 1 & 0 \\ 0 & 0 & 0 & 0 & 0 & 0 & 0 & 1 \\ 0 & 0 & 1 & 0 & 0 & (z - \bar{z}_k) & 0 & 0 \end{bmatrix} \tag{3.23}$$

Noting that for the composite core (c) the respective mid-plane transverse coordinate $\bar{z}_c$ is zero, while for the top and bottom layers, $\bar{z}_t$ and $\bar{z}_b$, are given in equation (3.4).

3.3 Layerwise Electric Potential

Attempting to obtain a LW description for the electric potential, one can use for each discrete layer, the linear z-expansion in equation (2.34), or the quadratic one in equation (2.35), imposing equipotential continuity conditions at the layer's interfaces, in figure 3.1, as shown:

$$\phi_c\,(x, y, z = h_c/2, t) = \phi_t\,(x, y, z = h_c/2, t) \tag{3.24a}$$

$$\phi_c\,(x, y, z = -h_c/2, t) = \phi_b\,(x, y, z = -h_c/2, t) \tag{3.24b}$$

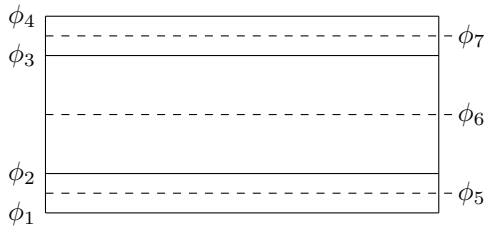

Figure 3.2: Electrical DOFs location in three discrete layers.

Defining the surface electric potentials represented in figure 3.2 as follows,

$$\phi_1(x,y,t) \equiv \phi(x,y,z=-h/2,t) \tag{3.25a}$$

$$\phi_2(x,y,t) \equiv \phi(x,y,z=-h_c/2,t) \tag{3.25b}$$

$$\phi_3(x,y,t) \equiv \phi(x,y,z=h_c/2,t) \tag{3.25c}$$

$$\phi_4(x,y,t) \equiv \phi(x,y,z=h/2,t) \tag{3.25d}$$

where h is the total plate thickness, i.e, $h = h_b + h_c + h_t$ (see figure 3.1), one obtains the linear z-expansion for the three discrete layers as:

$$\phi_c(x,y,z,t) = \frac{1}{2}\left(\phi_3(x,y,t) + \phi_2(x,y,t)\right) + \frac{z}{h_c}\left(\phi_3(x,y,t) - \phi_2(x,y,t)\right) \tag{3.26a}$$

$$\phi_t(x,y,z,t) = \frac{1}{2}\left(\phi_4(x,y,t) + \phi_3(x,y,t)\right) + \frac{(z-\bar{z}_t)}{h_t}\left(\phi_4(x,y,t) - \phi_3(x,y,t)\right) \tag{3.26b}$$

$$\phi_b(x,y,z,t) = \frac{1}{2}\left(\phi_2(x,y,t) + \phi_1(x,y,t)\right) + \frac{(z-\bar{z}_b)}{h_b}\left(\phi_2(x,y,t) - \phi_1(x,y,t)\right) \tag{3.26c}$$

Furthermore, in order to define a quadratic z-expansion for the electric potential, the potentials in the mid-planes must be introduced. Defining the electric potentials for the respective mid-planes of the three discrete layers in figure 3.2 as follows,

$$\phi_5(x,y,t) \equiv \phi(x,y,z=\bar{z}_b,t) \tag{3.27a}$$

$$\phi_6(x,y,t) \equiv \phi(x,y,z=0,t) \tag{3.27b}$$

$$\phi_7(x,y,t) \equiv \phi(x,y,z=\bar{z}_t,t) \tag{3.27c}$$

one obtains the quadratic z-expansion for the three discrete layers as shown,

$$\phi_c(x,y,z,t) = g_s^c(z)\phi_3(x,y,t) + g_i^c(z)\phi_2(x,y,t) + g_m^c(z)\phi_6(x,y,t) \tag{3.28a}$$

$$\phi_t(x,y,z,t) = g_s^t(z)\phi_4(x,y,t) + g_i^t(z)\phi_3(x,y,t) + g_m^t(z)\phi_7(x,y,t) \tag{3.28b}$$

$$\phi_b(x,y,z,t) = g_s^b(z)\phi_2(x,y,t) + g_i^b(z)\phi_1(x,y,t) + g_m^b(z)\phi_5(x,y,t) \tag{3.28c}$$

where the thickness coordinate functions are the one-dimensional quadratic Lagrange's functions, given in equation (2.36) for a generic layer, with $z_k = z - \bar{z}_k$, for $k = \{b,c,t\}$.

The seven electric potential unknowns, for the quadratic z-expansion, are ordained in the electric degrees of freedom vector $\{\varphi\}$ as,

$$\{\varphi\} = \{\phi_1\ \phi_2\ \phi_3\ \phi_4\ \phi_5\ \phi_6\ \phi_7\}^T \tag{3.29}$$

while for the linear z-expansion, only the first four variables are used.

3.4 Layerwise Electric Field

The LW electric field associated with both linear and quadratic z-expansions for the electric potential is derived from the field-potential relation in equation (2.6). For an arbitrary k-layer, the linear electric potential variation in equation (3.26), have the associated electric field components written in the global transverse coordinate z as follows:

$$\begin{aligned}
E_x^{(k)} &= -\frac{\partial \phi_{(k)}}{\partial x} = \frac{1}{2}\left(-\frac{\partial \phi_{sup}^{(k)}}{\partial x} - \frac{\partial \phi_{inf}^{(k)}}{\partial x}\right) + \frac{(z-\bar{z}_k)}{h_{(k)}}\left(-\frac{\partial \phi_{sup}^{(k)}}{\partial x} + \frac{\partial \phi_{inf}^{(k)}}{\partial x}\right) \\
E_y^{(k)} &= -\frac{\partial \phi_{(k)}}{\partial y} = \frac{1}{2}\left(-\frac{\partial \phi_{sup}^{(k)}}{\partial y} - \frac{\partial \phi_{inf}^{(k)}}{\partial y}\right) + \frac{(z-\bar{z}_k)}{h_{(k)}}\left(-\frac{\partial \phi_{sup}^{(k)}}{\partial y} + \frac{\partial \phi_{inf}^{(k)}}{\partial y}\right) \\
E_z^{(k)} &= -\frac{\partial \phi_{(k)}}{\partial z} = \frac{\phi_{inf}^{(k)} - \phi_{sup}^{(k)}}{h_{(k)}}
\end{aligned} \tag{3.30}$$

From the electric DOFs definitions, in equation (3.25), the electric field components within the composite core holds,

$$\begin{aligned}
E_{x_c} &= -\frac{\partial \phi_c}{\partial x} = \frac{1}{2}\left(-\frac{\partial \phi_3}{\partial x} - \frac{\partial \phi_2}{\partial x}\right) + \frac{z}{h_c}\left(-\frac{\partial \phi_3}{\partial x} + \frac{\partial \phi_2}{\partial x}\right) \\
E_{y_c} &= -\frac{\partial \phi_c}{\partial y} = \frac{1}{2}\left(-\frac{\partial \phi_3}{\partial y} - \frac{\partial \phi_2}{\partial y}\right) + \frac{z}{h_c}\left(-\frac{\partial \phi_3}{\partial y} + \frac{\partial \phi_2}{\partial y}\right) \\
E_{z_c} &= -\frac{\partial \phi_c}{\partial z} = \frac{\phi_2 - \phi_3}{h_c}
\end{aligned} \tag{3.31}$$

while the electric field for the piezoelectric top layer becomes,

$$\begin{aligned}
E_{x_t} &= -\frac{\partial \phi_t}{\partial x} = \frac{1}{2}\left(-\frac{\partial \phi_4}{\partial x} - \frac{\partial \phi_3}{\partial x}\right) + \frac{(z-\bar{z}_t)}{h_t}\left(-\frac{\partial \phi_4}{\partial x} + \frac{\partial \phi_3}{\partial x}\right) \\
E_{y_t} &= -\frac{\partial \phi_t}{\partial y} = \frac{1}{2}\left(-\frac{\partial \phi_4}{\partial y} - \frac{\partial \phi_3}{\partial y}\right) + \frac{(z-\bar{z}_t)}{h_t}\left(-\frac{\partial \phi_4}{\partial y} + \frac{\partial \phi_3}{\partial y}\right) \\
E_{z_t} &= -\frac{\partial \phi_t}{\partial z} = \frac{\phi_3 - \phi_4}{h_t}
\end{aligned} \tag{3.32}$$

as well as for the piezoelectric bottom layer as follows,

$$\begin{aligned}
E_{x_b} &= -\frac{\partial \phi_b}{\partial x} = \frac{1}{2}\left(-\frac{\partial \phi_2}{\partial x} - \frac{\partial \phi_1}{\partial x}\right) + \frac{(z-\bar{z}_b)}{h_b}\left(-\frac{\partial \phi_2}{\partial x} + \frac{\partial \phi_1}{\partial x}\right) \\
E_{y_b} &= -\frac{\partial \phi_b}{\partial y} = \frac{1}{2}\left(-\frac{\partial \phi_2}{\partial y} - \frac{\partial \phi_1}{\partial y}\right) + \frac{(z-\bar{z}_b)}{h_b}\left(-\frac{\partial \phi_2}{\partial y} + \frac{\partial \phi_1}{\partial y}\right) \\
E_{z_b} &= -\frac{\partial \phi_b}{\partial z} = \frac{\phi_1 - \phi_2}{h_b}
\end{aligned} \tag{3.33}$$

where a linear through-thickness variation is achieved for the in-plane components and a constant one for the transverse component.

Similarly to the generalized strain field, the k-discrete layer electric field vector $\{E\}_{(k)}$ can also be decomposed in generalized electric field components $\{\hat{E}\}_{(k)}$ following,

$$\{E\}_{(k)} = [S_\phi]_{(k)}\{\hat{E}\}_{(k)} \tag{3.34}$$

where the generalized electric field components for the linear z-expansion of the electric potential are defined by:

$$\{\hat{E}\}_{(k)} = \left\{ -\frac{\partial \phi_{sup}^{(k)}}{\partial x} - \frac{\partial \phi_{inf}^{(k)}}{\partial x} \, , -\frac{\partial \phi_{sup}^{(k)}}{\partial y} - \frac{\partial \phi_{inf}^{(k)}}{\partial y} \, , -\frac{\partial \phi_{sup}^{(k)}}{\partial x} + \frac{\partial \phi_{inf}^{(k)}}{\partial x} \, , -\frac{\partial \phi_{sup}^{(k)}}{\partial y} + \frac{\partial \phi_{inf}^{(k)}}{\partial y} \, , \phi_{inf}^{(k)} - \phi_{sup}^{(k)} \right\}^T \tag{3.35}$$

Hence, one obtains the electric field transformation matrix $[S_\phi]_{(k)}$, for $k = \{b, c, t\}$, as follows:

$$[S_\phi]_{(k)} = \begin{bmatrix} 1/2 & 0 & (z - \bar{z}_k)/h_{(k)} & 0 & 0 \\ 0 & 1/2 & 0 & (z - \bar{z}_k)/h_{(k)} & 0 \\ 0 & 0 & 0 & 0 & 1/h_{(k)} \end{bmatrix} \tag{3.36}$$

From the quadratic z-expansion of the electric potential in equation (3.28), the associated electric field for the k-discrete layer holds,

$$\begin{aligned} E_x^{(k)} &= -\frac{\partial \phi_{(k)}}{\partial x} = -g_s^{(k)}(z)\frac{\partial \phi_{sup}^{(k)}}{\partial x} - g_i^{(k)}(z)\frac{\partial \phi_{inf}^{(k)}}{\partial x} - g_m^{(k)}(z)\frac{\partial \phi_{mid}^{(k)}}{\partial x} \\ E_y^{(k)} &= -\frac{\partial \phi_{(k)}}{\partial y} = -g_s^{(k)}(z)\frac{\partial \phi_{sup}^{(k)}}{\partial y} - g_i^{(k)}(z)\frac{\partial \phi_{inf}^{(k)}}{\partial y} - g_m^{(k)}(z)\frac{\partial \phi_{mid}^{(k)}}{\partial y} \\ E_z^{(k)} &= -\frac{\partial \phi_{(k)}}{\partial z} = -\frac{\mathrm{d}g_s^{(k)}}{\mathrm{d}z}\phi_{sup}^{(k)} - \frac{\mathrm{d}g_i^{(k)}}{\mathrm{d}z}\phi_{inf}^{(k)} - \frac{\mathrm{d}g_m^{(k)}}{\mathrm{d}z}\phi_{mid}^{(k)} \end{aligned} \tag{3.37}$$

where the in-plane components are through-thickness quadratic and the transverse one is through-thickness linear, due to the quadratic Lagrange's functions in equation (2.36).

For the bottom layer, $k = b$, the potentials $\left(\phi_{inf}^{(b)}, \phi_{sup}^{(b)}, \phi_{mid}^{(b)}\right)$ are equivalent to the aforementioned potentials (ϕ_1, ϕ_2, ϕ_5) in equations (3.25) and (3.27). Likewise, for the composite core, $k = c$, where $\left(\phi_{inf}^{(c)}, \phi_{sup}^{(c)}, \phi_{mid}^{(c)}\right) \equiv (\phi_2, \phi_3, \phi_6)$, while for the top layer, $k = t$, being $\left(\phi_{inf}^{(t}, \phi_{sup}^{(t)}, \phi_{mid}^{(t)}\right) \equiv (\phi_3, \phi_4, \phi_7)$.

In order to satisfy the generalized electric field transformation in equation (3.34), one could define the new generalized electric field components for the quadratic potential as

$$\{\hat{E}\}_{(k)} = -\left\{ \frac{\partial \phi_{sup}^{(k)}}{\partial x} \, , \frac{\partial \phi_{inf}^{(k)}}{\partial x} \, , \frac{\partial \phi_{mid}^{(k)}}{\partial x} \, , \frac{\partial \phi_{sup}^{(k)}}{\partial y} \, , \frac{\partial \phi_{inf}^{(k)}}{\partial y} \, , \frac{\partial \phi_{mid}^{(k)}}{\partial y} \, , \phi_{sup}^{(k)} \, , \phi_{inf}^{(k)} \, , \phi_{mid}^{(k)} \right\}^T \tag{3.38}$$

and from the electric field in equation (3.37), the consequent electric field transformation matrix $[S_\phi]_{(k)}$, for $k = \{b, c, t\}$, are given by:

$$[S_\phi]_{(k)} = \begin{bmatrix} g_s^{(k)}(z) & g_i^{(k)}(z) & g_m^{(k)}(z) & 0 & 0 & 0 & 0 & 0 & 0 \\ 0 & 0 & 0 & g_s^{(k)}(z) & g_i^{(k)}(z) & g_m^{(k)}(z) & 0 & 0 & 0 \\ 0 & 0 & 0 & 0 & 0 & 0 & dg_s^{(k)}/dz & dg_i^{(k)}/dz & dg_m^{(k)}/dz \end{bmatrix} \tag{3.39}$$

3.5 Multilayered Generalized Constitutive Equations

The piezoelectric multilayered constitutive equations relate the force and moment resultants, per unit length, to the strains and electric field of a piezoelectric laminated plate. The in-plane force resultants (N_{xx}, N_{yy}, N_{xy}) and the moment resultants (M_{xx}, M_{yy}, M_{xy}) are derived from the thickness integration of the in-plane stresses as follows,

$$\begin{Bmatrix} N_{xx} \\ N_{yy} \\ N_{xy} \end{Bmatrix} = \int_{-\frac{h}{2}}^{\frac{h}{2}} \begin{Bmatrix} \sigma_{xx} \\ \sigma_{yy} \\ \tau_{xy} \end{Bmatrix} dz, \quad \begin{Bmatrix} M_{xx} \\ M_{yy} \\ M_{xy} \end{Bmatrix} = \int_{-\frac{h}{2}}^{\frac{h}{2}} \begin{Bmatrix} \sigma_{xx} \\ \sigma_{yy} \\ \tau_{xy} \end{Bmatrix} z \, dz \tag{3.40}$$

while the transverse force resultants (Q_x, Q_y) are related to the transverse shear stresses through

$$\begin{Bmatrix} Q_y \\ Q_x \end{Bmatrix} = K_s \int_{-\frac{h}{2}}^{\frac{h}{2}} \begin{Bmatrix} \tau_{yz} \\ \tau_{xz} \end{Bmatrix} dz \tag{3.41}$$

where K_s is the shear correction factor used to account for the discrepancy between the real transverse shear stress state and the constant one assumed by the FSDT. In a first approximation, Birman et al. [39] suggest a unitary K_s for multilayered sandwich structures, which is the default value used in the present model.

Due to different material properties in each layer and consequent discontinuous stress fields, the thickness integration is carried out using a lamina-wise integration in the layer's local transverse coordinate. Following the generalized fields defined in equations (3.22) and (3.34), the stress resultants vector for the k-layer $\{\hat{\sigma}\}_{(k)}$, as well as the electric displacement resultants $\{\hat{D}\}_{(k)}$ are given by:

$$\{\hat{\sigma}\}_{(k)} = \int_{z_{(k)}^{inf}}^{z_{(k)}^{sup}} [S]_{(k)}^{T} \{\sigma\}_{(k)} \, dz_k, \quad \{\hat{D}\}_{(k)} = \int_{z_{(k)}^{inf}}^{z_{(k)}^{sup}} [S_\phi]_{(k)}^{T} \{D\}_{(k)} \, dz_k \tag{3.42}$$

where z_k is the local transverse coordinate, i.e., $z_k = z - \bar{z}_k$ which varies from the bottom $z_{(k)}^{inf} = -h_{(k)}/2$ to the top $z_{(k)}^{sup} = h_{(k)}/2$. Introducing the piezoelectric constitutive equations (2.18), and then the generalized fields definitions in equations (3.22) and (3.34), in equation (3.42), one obtains the generalized constitutive equations as follows,

$$\begin{aligned} \{\hat{\sigma}\}_{(k)} &= [\hat{Q}]_{(k)} \{\hat{\varepsilon}\}_{(k)} - [\hat{e}]_{(k)} \{\hat{E}\}_{(k)} \\ \{\hat{D}\}_{(k)} &= [\hat{e}]_{(k)}^{T} \{\hat{\varepsilon}\}_{(k)} + [\hat{\epsilon}]_{(k)} \{\hat{E}\}_{(k)} \end{aligned} \tag{3.43}$$

where the generalized constitutive matrices are obtained following the integration along the layer's thickness direction as shown:

$$[\hat{Q}]_{(k)} = \int_{z_{(k)}^{inf}}^{z_{(k)}^{sup}} [S]_{(k)}^{T} \left[\bar{Q}\right]_{(k)} [S]_{(k)} \; dz_k \tag{3.44a}$$

$$[\hat{e}]_{(k)} = \int_{z_{(k)}^{inf}}^{z_{(k)}^{sup}} [S]_{(k)}^{T} [\bar{e}]_{(k)} [S_\phi]_{(k)} \; dz_k \tag{3.44b}$$

$$[\hat{e}]^T_{(k)} = \int_{z^{inf}_{(k)}}^{z^{sup}_{(k)}} [S_\phi]^T_{(k)} \, [\bar{e}]^T_{(k)} \, [S]_{(k)} \; dz_k \tag{3.44c}$$

$$[\hat{\epsilon}]_{(k)} = \int_{z^{inf}_{(k)}}^{z^{sup}_{(k)}} [S_\phi]^T_{(k)} \, [\bar{\epsilon}]_{(k)} \, [S_\phi]_{(k)} \, dz_k \tag{3.44d}$$

The generalized constitutive matrices in equations (3.44) are explicitly presented in the Appendix D, for the model with linear z-expansion of the electric potential.

For the whole multilayered plate, applying the additive property of the integral operator to equations (3.40) and (3.41), the stress resultants are the sum of each layer's contribution. Considering the present discrete LW model with three-discrete layers, one obtains:

$$\{\hat{\sigma}\} = \sum_{k=c,t,b} \{\hat{\sigma}\}_{(k)} = \sum_{k=c,t,b} [\hat{Q}]_{(k)} \, \{\hat{\varepsilon}\}_{(k)} - \sum_{k=c,t,b} [\hat{e}]_{(k)} \{\hat{E}\}_{(k)} \tag{3.45}$$

and

$$\{\hat{D}\} = \sum_{k=c,t,b} \{\hat{D}\}_{(k)} = \sum_{k=c,t,b} [\hat{e}]^T_{(k)} \, \{\hat{\varepsilon}\}_{(k)} + \sum_{k=c,t,b} [\hat{\epsilon}]_{(k)} \{\hat{E}\}_{(k)} \tag{3.46}$$

Noting that for the multilayered composite core ($k = c$), where an ESL approach is used, each one of the generalized constitutive matrices in equations (3.44) are the sum of the respective generalized constitutive matrices for each composite layer, integrated using a lamina-wise scheme as consequence of the additive property of integral operator. In these layers, the transverse coordinate of the mid-plane is null, i.e., $\bar{z}_c = 0$, for all layers in the composite core, since the multilayered composite core is treated as an equivalent single layer.

Chapter 4

Finite Element Formulation

In this chapter, the finite element approximation is used to describe and implement in a computational way, the already presented discrete layerwise models for piezoelectric multilayered composite plates. The finite element formulation is presented for a quadrilateral electro-elastic plate element, where the element stiffness and mass matrices are derived for static and free-vibration analysis. Moreover, optimal post-processing procedures are discussed and an improved method is presented for the determination of transverse shear stresses.

4.1 Finite Element Approximation

The finite element approximation on the element domain Ω_e, for both mechanical and electrical DOFs in equations (3.11) and (3.29), respectively, is made using the same interpolation functions ψ_j^e. Briefly, the finite element approximation takes the form,

$$w_0(x,y,t) = \sum_{j=1}^{n} \psi_j^e(x,y) w_{0_j}^e(t) \tag{4.1}$$
$$\phi_1(x,y,t) = \sum_{j=1}^{n} \psi_j^e(x,y) {\phi_1}_j^e(t)$$

where n it's the element number of nodes per element, while $w_{0_j}^e$ and ${\phi_1}_j^e$ are the transverse displacement and electric potential at the j^{th}-node of the e-element, respectively.

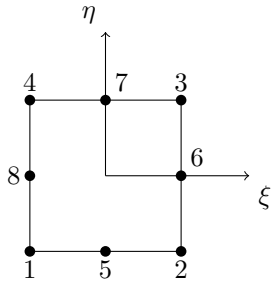

Figure 4.1: Eight node quadratic serendipity master element.

The finite element approximation is achieved using the quadratic serendipity eight node $(n = 8)$

interpolation functions. In terms of the master element $\Omega_e = \{(\xi,\eta) \in \mathbb{R}^2 : -1 < \xi < 1, \ -1 < \eta < 1\}$, in figure 4.1, the interpolation functions, according to Reddy [18], are given by:

$$\begin{Bmatrix} \psi_1^e \\ \psi_2^e \\ \psi_3^e \\ \psi_4^e \\ \psi_5^e \\ \psi_6^e \\ \psi_7^e \\ \psi_8^e \end{Bmatrix} = \frac{1}{4} \begin{Bmatrix} (1-\xi)(1-\eta)(-\xi-\eta-1) \\ (1+\xi)(1-\eta)(\xi-\eta-1) \\ (1+\xi)(1+\eta)(\xi+\eta-1) \\ (1-\xi)(1+\eta)(-\xi+\eta-1) \\ 2(1-\xi^2)(1-\eta) \\ 2(1+\xi)(1-\eta^2) \\ 2(1-\xi^2)(1+\eta) \\ 2(1-\xi)(1-\eta^2) \end{Bmatrix} \tag{4.2}$$

A generic matrix form for the element mechanical DOFs vector can be achieved defining a matrix $[N]$, containing the serendipity shape functions. The overall element DOFs, either mechanical $\{d\}^{(e)}$ or electrical $\{\varphi\}^{(e)}$, can be expressed as a function of the nodal DOFs $\{d\}_j^{(e)}$ and $\{\varphi\}_j^{(e)}$ for all the n j-nodes as shown,

$$\{d\}^{(e)} = [N]\{a\}^{(e)}, \ \ \{a\}^{(e)} = \{\{d\}_1^{(e)^T} ... \{d\}_n^{(e)^T}\}^T \tag{4.3}$$

and

$$\{\varphi\}^{(e)} = [N_\phi]\{\bar{\varphi}\}^{(e)}, \ \ \{\bar{\varphi}\}^{(e)} = \{\{\varphi\}_1^{(e)^T} ... \{\varphi\}_n^{(e)^T}\}^T \tag{4.4}$$

where the element shape functions matrices for the mechanical DOFs, $[N]$, and for the electrical ones, $[N_\phi]$, are given by:

$$[N] = [[\Psi]_1, [\Psi]_2, ..., [\Psi]_n] \tag{4.5}$$

and

$$[N_\phi] = \left[[\Psi_\phi]_1, [\Psi_\phi]_2, ..., [\Psi_\phi]_n\right] \tag{4.6}$$

with $n = 8$ for an element with eight nodes. Moreover, the diagonal matrices $[\Psi]_j$ and $[\Psi_\phi]_j$, with $j = \{1, ..., 8\}$, are define as follows:

$$[\Psi]_j = \psi_j^e \left[I_{n_d}\right] \ \ [\Psi_\phi]_j = \psi_j^e \left[I_{n_\phi}\right] \tag{4.7}$$

where $[I_{n_d}]$, is the $n_d \times n_d$ identity matrix with $n_d = 9$, i.e., the number of mechanical DOFs. Similarly, $[I_{n_\phi}]$ is also an $n_\phi \times n_\phi$ identity matrix, with $n_\phi = 4$ for the linear z-expansion of the electric potential or $n_\phi = 7$ for the quadratic z-expansion.

Besides the displacement and electric potential DOFs, one could obtain the generalized strains in equation (3.22), as well as the generalized electric field components in equation (3.34) from the finite element approximation for the DOFs in equations (4.3) and (4.4). For each k-layer, with $k = \{t, c, b\}$, the relation between the generalized strains and the nodal mechanic DOFs holds,

$$\{\hat{\varepsilon}\}_{(k)} = [B]_{(k)}\{a\} \tag{4.8}$$

where $[B]_{(k)}$ is the element generalized strain matrix for the k-layer, which in fact is the concatenation of the n nodal generalized strain matrix as shown,

$$[B]_{(k)} = \left[[B]_{(k)_1} \ [B]_{(k)_2} \ ... \ [B]_{(k)_n} \right] \tag{4.9}$$

with $[B]_{(k)_j}$ the j-node generalized strain matrix for the k-layer and $n = 8$ nodes.

Similarly, for the same k-layer, the relation between the generalized electric field and the nodal electric DOFs holds,

$$\{\hat{E}\}_{(k)} = -[B_\phi]_{(k)}\{\bar{\varphi}\} \tag{4.10}$$

where $[B_\phi]_{(k)}$ is the element generalized electric field matrix for the k-layer, given by:

$$[B_\phi]_{(k)} = \left[[B_\phi]_{(k)_1}, [B_\phi]_{(k)_2}, ..., [B_\phi]_{(k)_n} \right] \tag{4.11}$$

with $[B_\phi]_{(k)_j}$ the j-node generalized electric field matrix for the k-layer and again $n = 8$ nodes.

Both nodal strain and nodal electric field matrices in equations (4.9) and (4.11) are explicitly presented in Appendix C for the three-discrete layers as a function of the interpolation functions (4.2) and their derivatives, considering an arbitrary j-node.

4.2 Element Stiffness and Mass Matrices

The element stiffness and mass matrices establish the equilibrium equations through a system of linear equations, at the element level, where the unknowns are the element DOFs and their second derivatives with respect to the time. The Hamilton's principle (2.27) is used to derive the governing equations for static and free vibration analysis, knowing that for the k-discrete layer, which fills the volume domain $\Omega_{(k)}$, the kinetic energy in equation (2.28) and the electromechanical energy in equation (2.29), can now be written using matrix notation as follows,

$$T_{(k)} = \frac{1}{2} \int_{\Omega_{(k)}} \rho_{(k)} \{\dot{u}\}^T_{(k)} \{\dot{u}\}_{(k)} d\Omega_{(k)} \tag{4.12}$$

and

$$U_{(k)} = \frac{1}{2} \int_{\Omega_{(k)}} \left(\{\varepsilon\}^T_{(k)} \{\sigma\}_{(k)} - \{E\}^T_{(k)} \{D\}_{(k)} \right) d\Omega_{(k)} \tag{4.13}$$

while the external work in equation (2.30), in the absence of volume forces and surface charges reads,

$$W_{(k)} = \int_{S_{(k)}} \{u\}^T_{(k)} \{f_s\}_{(k)} \, dS_{(k)} + \{u\}^T_{(k)} \{f_c\}_{(k)} \tag{4.14}$$

knowing that $\{f_s\}_{(k)}$ and $\{f_c\}_{(k)}$ are the k-layer surface and concentrated forces, respectively.

The integral over the k-layer volume domain $\Omega_{(k)}$ in equations (4.12) and (4.13), can be decomposed into a surface integral in the k-layer surface $S_{(k)}$, following an integral in the transverse coordinate domain $z_k \in \left[-h_{(k)}/2, h_{(k)}/2\right]$. Hence, for the whole piezoelectric multilayered plate, the total kinetic and

potential energies will be the sum of all layer's energies, specifically for the present model,

$$T = \sum_{k=c,t,b} T_{(k)} = \sum_{k=c,t,b} \frac{1}{2} \int_{\Omega_{(k)}} \rho_{(k)} \{\dot{u}\}_{(k)}^T \{\dot{u}\}_{(k)} d\Omega_{(k)} \tag{4.15}$$

and

$$U = \sum_{k=c,t,b} U_{(k)} = \sum_{k=c,t,b} \frac{1}{2} \int_{\Omega_{(k)}} \left(\{\varepsilon\}_{(k)}^T \{\sigma\}_{(k)} - \{E\}_{(k)}^T \{D\}_{(k)} \right) d\Omega_{(k)} \tag{4.16}$$

The total kinetic energy in equation (4.15), can be rewritten using the displacement-DOFs relation, equation (3.12), and the element shape function matrices in equation (4.3), leading to

$$T = \frac{1}{2} \sum_{k=c,t,b} \int_{S_{(k)}} \rho_{(k)} \{\dot{a}\}^T [N]^T [P]_{(k)} [N] \{\dot{a}\} \, dS_{(k)} \tag{4.17}$$

where the $[P]_{(k)}$ matrix is given by:

$$[P]_{(k)} = \int_{z_{(k)}^{inf}}^{z_{(k)}^{sup}} [Z]_{(k)}^T [Z]_{(k)} \, dz_k \tag{4.18}$$

Also, the total electromechanical energy in equation (4.16), can be related to the nodal DOFs using the piezoelectric constitutive equations in (2.18), following the transformation to generalized strains and electric field in equations (3.22) and (3.34), as well as the relation between the generalized strains and electric field to the mechanical and electrical DOFs in equations (4.8) and (4.10), respectively. Hence, one obtains:

$$\begin{aligned} U &= \sum_{k=c,t,b} \frac{1}{2} \int_{\Omega_{(k)}} \left(\{\varepsilon\}_{(k)}^T [\bar{Q}]_{(k)} \{\varepsilon\}_{(k)} - \{\varepsilon\}_{(k)}^T [\bar{e}]_{(k)} \{E\}_{(k)} - \{E\}_{(k)}^T [\bar{e}]_{(k)}^T \{\varepsilon\}_{(k)} - \{E\}_{(k)}^T [\bar{\epsilon}]_{(k)} \{E\}_{(k)} \right) d\Omega_{(k)} \\ &= \frac{1}{2} \sum_{k=c,t,b} \int_{S_{(k)}} \{a\}^T [B]_{(k)}^T [\hat{Q}]_{(k)} [B]_{(k)} \{a\} \, dS_{(k)} + \int_{S_{(k)}} \{a\}^T [B]_{(k)}^T [\hat{e}]_{(k)} [B_\phi]_{(k)} \{\bar{\varphi}\} \, dS_{(k)} \\ &\quad + \int_{S_{(k)}} \{\bar{\varphi}\}^T [B_\phi]_{(k)}^T [\hat{e}]_{(k)}^T [B]_{(k)} \{a\} \, dS_{(k)} - \int_{S_{(k)}} \{\bar{\varphi}\}^T [B_\phi]_{(k)}^T [\hat{\epsilon}]_{(k)} [B_\phi]_{(k)} \{\bar{\varphi}\} \, dS_{(k)} \end{aligned} \tag{4.19}$$

where the generalized constitutive matrices $[\hat{Q}]$, $[\hat{e}]$ and $[\hat{\epsilon}]$ are given in (3.44).

Following the energy principle at stationary conditions and the variational principle in equation (2.26), one obtains the element dynamic equilibrium equations for the piezoelectric multilayered plate as follows,

$$\begin{bmatrix} [M_{uu}]^{(e)} & [0] \\ [0] & [0] \end{bmatrix} \begin{Bmatrix} \{\ddot{a}\} \\ \{\ddot{\bar{\varphi}}\} \end{Bmatrix}^{(e)} + \begin{bmatrix} [K_{uu}]^{(e)} & [K_{u\phi}]^{(e)} \\ [K_{\phi u}]^{(e)} & [K_{\phi\phi}]^{(e)} \end{bmatrix} \begin{Bmatrix} \{a\} \\ \{\bar{\varphi}\} \end{Bmatrix}^{(e)} = \begin{Bmatrix} \{F_u\} \\ \{0\} \end{Bmatrix}^{(e)} \tag{4.20}$$

where the mass sub-matrix $[M_{uu}]^{(e)}$ for the element is given by,

$$[M_{uu}]^{(e)} = \sum_{k=c,t,b} \int_{S_{(k)}} \rho_{(k)} [N]^T [P]_{(k)} [N] \; dS_{(k)} \tag{4.21}$$

while the stiffness sub-matrices, particularly, $[K_{uu}]^{(e)}$ the elastic stiffness matrix, $[K_{u\phi}]^{(e)} = [K_{\phi u}]^{(e)^T}$

the electromechanical coupling stiffness matrices and $[K_{\phi\phi}]^{(e)}$ the dielectric stiffness matrix, are given by:

$$[K_{uu}]^{(e)} = \sum_{k=c,t,b} \int_{S_{(k)}} [B]_{(k)}^{(e)^T} [\hat{Q}]_{(k)} [B]_{(k)}^{(e)} \, dS_{(k)} \tag{4.22a}$$

$$[K_{u\phi}]^{(e)} = \sum_{k=c,t,b} \int_{S_{(k)}} [B]_{(k)}^{(e)^T} [\hat{e}]_{(k)} [B_\phi]_{(k)}^{(e)} \, dS_{(k)} \tag{4.22b}$$

$$[K_{\phi u}]^{(e)} = \sum_{k=c,t,b} \int_{S_{(k)}} [B_\phi]_{(k)}^{(e)^T} [\hat{e}]_{(k)}^T [B]_{(k)}^{(e)} \, dS_{(k)} \; = \; [K_{u\phi}]^{(e)^T} \tag{4.22c}$$

$$[K_{\phi\phi}]^{(e)} = - \sum_{k=c,t,b} \int_{S_{(k)}} [B_\phi]_{(k)}^{(e)^T} [\hat{\epsilon}]_{(k)} [B_\phi]_{(k)}^{(e)} \, dS_{(k)} \tag{4.22d}$$

From the external work, equation (4.14), one could obtain the mechanical force vector as shown:

$$\{F_u\}^{(e)} = \sum_{k=c,t,b} \int_{S_{(k)}} [N] [Z]_{(k)}^T \{f_s\}_{(k)}^{(e)} \, dS_{(k)} + [N] [Z]_{(k)}^T \{f_c\}_{(k)}^{(e)} \tag{4.23}$$

which computation is not required in the UEL subroutine because the loads are applied to a soft dummy plate element available in Abaqus (S8R), attached to the UEL, being the computation of the force vector fully performed by Abaqus. Moreover, for the case of transverse loads, the nonzero force components are applied to the transverse displacement DOF, which is the same for all layers.

The system of equilibrium equations (4.20), after the usual assembly procedures performed by Abaqus, leads to the overall system of equilibrium equations for the multilayered plate, which is solved in static analysis by neglecting the inertial terms. In free vibration analysis, when imposing zero applied forces, as well as an harmonic motion for the DOFs, the overall system of equations (4.20) leads to an eigenvalue problem, where the eigenvalues are the square of the vibration frequencies, i.e., ω_{mn}^2, and the eigenvectors are the vibration modes.

4.3 Coordinate Transformation

Attempting to avoid the computation of complex and numerous integrals, the stiffness and mass matrices are computed using numerical integration. Specifically, the useful Gauss-Legendre quadrature is used attempting to obtain an exact approach to evaluate the integrals of the polynomial functions provided by the quadratic interpolation functions.

In fact, both nodal strain and electric field matrices in equations (4.9) and (4.11), which are explicitly presented in Appendix C for the three-discrete layers, are linearly dependent on the interpolation functions in equation (4.2) and their derivatives.Therefore, a coordinate transformation between the global coordinate system (x, y) and the natural one (ξ, η) must be used in order to simplify the integration over a quadrilateral element Ω^e by means of a master element $\hat{\Omega}$.

The coordinate transformation between Ω^e and $\hat{\Omega}$ is by definition the mapping of any point (x, y) in

Ω^e of the mesh, to a point (ξ, η) in $\hat{\Omega}$ which is achieved by,

$$x = \sum_{j=1}^{m} x_j^e \hat{\psi}_j^e(\xi, \eta), \quad y = \sum_{j=1}^{m} y_j^e \hat{\psi}_j^e(\xi, \eta) \tag{4.24}$$

where $\hat{\psi}_j^e(\xi, \eta)$ are the interpolation functions of the master element and $m = n = 8$ is the number of nodes per element. These functions can differ from the element interpolation functions used to approximate the DOFs, although in this model the same quadratic serendipity interpolation functions, equation (4.2), will be used for both DOFs and geometric approximations, which leads to an isoparametric finite element, according to Reddy [17].

Using the chain rule, the derivatives of the interpolation functions with respect to the natural coordinates can be written as shown,

$$\begin{aligned} \frac{\partial \psi_j^e}{\partial \xi} &= \frac{\partial \psi_j^e}{\partial x}\frac{\partial x}{\partial \xi} + \frac{\partial \psi_j^e}{\partial y}\frac{\partial y}{\partial \xi} \\ \frac{\partial \psi_j^e}{\partial \eta} &= \frac{\partial \psi_j^e}{\partial x}\frac{\partial x}{\partial \eta} + \frac{\partial \psi_j^e}{\partial y}\frac{\partial y}{\partial \eta} \end{aligned} \tag{4.25}$$

or using the usual matrix form, the transformation Jacobian matrix $[J]^e$ will appear as follows:

$$\begin{Bmatrix} \frac{\partial \psi_j^e}{\partial \xi} \\ \frac{\partial \psi_j^e}{\partial \eta} \end{Bmatrix} = \begin{bmatrix} \frac{\partial x}{\partial \xi} & \frac{\partial y}{\partial \xi} \\ \frac{\partial x}{\partial \eta} & \frac{\partial y}{\partial \eta} \end{bmatrix}^e \begin{Bmatrix} \frac{\partial \psi_j^e}{\partial x} \\ \frac{\partial \psi_j^e}{\partial y} \end{Bmatrix} = [J]^e \begin{Bmatrix} \frac{\partial \psi_j^e}{\partial x} \\ \frac{\partial \psi_j^e}{\partial y} \end{Bmatrix} \tag{4.26}$$

Using the coordinated transformation in equation (4.24), one could obtain the e-element Jacobian matrix given by:

$$[J]^e = \sum_{j=1}^{m} \begin{bmatrix} x_j \frac{\partial \hat{\psi}_j}{\partial \xi} & y_j \frac{\partial \hat{\psi}_j}{\partial \xi} \\ x_j \frac{\partial \hat{\psi}_j}{\partial \eta} & y_j \frac{\partial \hat{\psi}_j}{\partial \eta} \end{bmatrix} = \begin{bmatrix} \frac{\partial \hat{\psi}_1}{\partial \xi} & \frac{\partial \hat{\psi}_2}{\partial \xi} & \dots & \frac{\partial \hat{\psi}_m}{\partial \xi} \\ \frac{\partial \hat{\psi}_1}{\partial \eta} & \frac{\partial \hat{\psi}_2}{\partial \eta} & \dots & \frac{\partial \hat{\psi}_m}{\partial \eta} \end{bmatrix} \begin{bmatrix} x_1 & y_1 \\ x_2 & y_2 \\ \vdots & \vdots \\ x_m & y_m \end{bmatrix} \tag{4.27}$$

Since the physical model is built on the (x, y) coordinates, the derivatives of the interpolation functions, with respect to x and y, are evaluated inverting equation (4.26) leading to,

$$\begin{Bmatrix} \frac{\partial \psi_j^e}{\partial x} \\ \frac{\partial \psi_j^e}{\partial y} \end{Bmatrix} = [J]^{-1} \begin{Bmatrix} \frac{\partial \psi_j^e}{\partial \xi} \\ \frac{\partial \psi_j^e}{\partial \eta} \end{Bmatrix} = [J^*] \begin{Bmatrix} \frac{\partial \psi_j^e}{\partial \xi} \\ \frac{\partial \psi_j^e}{\partial \eta} \end{Bmatrix} \tag{4.28}$$

where the entries of the inverse Jacobian matrix $[J^*]$ are defined using the Jacobian matrix determinant $\mathcal{J} = J_{11}J_{22} - J_{12}J_{21}$, following:

$$J_{11}^* = \frac{J_{22}}{\mathcal{J}}, \quad J_{12}^* = -\frac{J_{12}}{\mathcal{J}}, \quad J_{22}^* = \frac{J_{11}}{\mathcal{J}}, \quad J_{21}^* = -\frac{J_{21}}{\mathcal{J}} \tag{4.29}$$

Note that the Jacobian matrix $[J]$ must be nonsingular, in order to be invertible and should have a positive determinant $\mathcal{J}$. In fact, the Jacobian matrix determinant, it's also the key to transform the infinitesimal element of area $dS = dxdy$, in the element domain Ω^e, to an infinitesimal element of area

$d\xi d\eta$ in the master element $\hat{\Omega}$, through $dxdy = \mathcal{J}d\xi d\eta$, allowing the numerical integration via Gauss-Legendre quadrature. Moreover, on the right hand-side of equation (4.28), the first derivatives of the eight node serendipity shape function, with respect to the natural coordinates, are found in Reddy [18].

4.4 Gauss Numerical Integration

There are several numerical methods that intend to obtain an approximated solution for a certain integral. According to Reddy [18], the Gauss quadrature over a rectangular master element $\hat{\Omega}$, for an arbitrary scalar field $F(\xi, \eta)$ yields,

$$\int_{\hat{\Omega}} F(\xi,\eta)d\xi d\eta \approx \sum_{i=1}^{M_G}\sum_{j=1}^{N_G} F(\xi_i,\eta_j)W_iW_j \tag{4.30}$$

where M_G and N_G denote the number of Gauss points in the ξ and η-directions, respectively, the pair (ξ_i, η_j) denote the Gauss points coordinates, while W_i and W_j represent the associated Gauss weights. Since the interpolation functions have the same order in ξ and η, one has $M_G = N_G$, and a total of $N_G \times N_G$ Gauss points are used. Also, the number of Gauss points can be chosen in order to obtain exact solutions, knowing that a p-order polynomial function is exactly integrated when $N_G = int\left[(p+1)/2\right]$ Gauss points, in both ξ and η-directions, are employed.

Observing the mass sub-matrix in equation (4.21), the associated $[N]$ matrices, defined in equation (4.5), are the ones that contain the interpolation functions which needs to be integrated. Hence, one could obtain that the polynomial of higher order that will appear in the mass matrix (4.21), is ψ_j^2. Knowing that the shape functions ψ_j in equation (4.2) are quadratic, then ψ_j^2 is a polynomial function with order $p = 4$. Consequently, the number of Gauss points necessary to exactly integrate equation (4.21) is $N_G = 3$. Following equations (4.21) and (4.30), one obtains:

$$\begin{aligned}
\left[M_{uu}\right]^{(e)} &= \sum_{k=c,t,b}\int_{-1}^{1}\int_{-1}^{1}\rho_{(k)}\left[N\right]^T\left[P\right]_{(k)}\left[N\right]\mathcal{J}d\xi d\eta \\
&= \sum_{k=c,t,b}\left(\sum_{i=1}^{3}\sum_{j=1}^{3}\rho_{(k)}\left[N(\xi_i,\eta_j)\right]^T\left[P\right]_{(k)}\left[N(\xi_i,\eta_j)\right]\mathcal{J}(\xi_i,\eta_j)W_iW_j\right)
\end{aligned} \tag{4.31}$$

Following the same procedure for the stiffness sub-matrices in equations (4.22), inspecting the the generalized strain matrices $[B]_{(k)_j}$, in Appendix C, one could obtain that for the elastic stiffness matrix $[K_{uu}]^{(e)}$, the higher order polynomial function in the membrane and bending terms have order $p = 2$, leading to $N_G = 2$ Gauss points. For the shear terms, the associated polynomial with higher order have $p = 4$, witch gives $N_G = 3$.

According to Reddy's book [17], in order to avoid the shear locking phenomena, reduced integration must be carried for the shear terms. Hence, only $N_G = 2$ Gauss points are used to integrate the shear terms of the stiffness sub-matrix $[K_{uu}]^{(e)}$.

Consequently, the elastic stiffness sub-matrix in equation (4.30) can be exactly evaluated by means

of the Gauss quadrature following:

$$\begin{aligned}[K_{uu}]^{(e)} &= \sum_{k=c,t,b} \int_{-1}^{1}\int_{-1}^{1} [B]_{(k)}^{T} [\hat{Q}]_{(k)} [B]_{(k)} \mathcal{J} d\xi d\eta \\ &= \sum_{k=c,t,b} \left(\sum_{i=1}^{2}\sum_{j=1}^{2} [B(\xi_i,\eta_j)]_{(k)}^{T} [\hat{Q}]_{(k)} [B(\xi_i,\eta_j)]_{(k)} \mathcal{J}(\xi_i,\eta_j) W_i W_j \right)\end{aligned} \tag{4.32}$$

Also, for the dielectric stiffness sub-matrix, $[K_{\phi\phi}]^{(e)}$, inspecting the electric field matrices $[B_\phi]_{(k)_j}$, in Appendix C, the number of necessary Gauss points is $N_G = 3$, leading to:

$$\begin{aligned}[K_{\phi\phi}]^{(e)} &= -\sum_{k=c,t,b} \int_{-1}^{1}\int_{-1}^{1} [B_\phi]_{(k)}^{T} [\hat{\epsilon}]_{(k)} [B_\phi]_{(k)} \mathcal{J} d\xi d\eta \\ &= \sum_{k=c,t,b} \left(\sum_{i=1}^{3}\sum_{j=1}^{3} [B_\phi(\xi_i,\eta_j)]_{(k)}^{T} [\hat{\epsilon}]_{(k)} [B_\phi(\xi_i,\eta_j)]_{(k)} \mathcal{J}(\xi_i,\eta_j) W_i W_j \right)\end{aligned} \tag{4.33}$$

Finally, for the electromechanical coupling stiffness sub-matrix, $[K_{u\phi}]^{(e)}$, using the same argument as before, $N_G = 3$ Gauss points are used to evaluate the coupling matrix as shown:

$$\begin{aligned}[K_{u\phi}]^{(e)} &= \sum_{k=c,t,b} \int_{-1}^{1}\int_{-1}^{1} [B]_{(k)}^{T} [\hat{e}]_{(k)} [B_\phi]_{(k)} \mathcal{J} d\xi d\eta \\ &= \sum_{k=c,t,b} \left(\sum_{i=1}^{3}\sum_{j=1}^{3} [B(\xi_i,\eta_j)]_{(k)}^{T} [\hat{e}]_{(k)} [B_\phi(\xi_i,\eta_j)]_{(k)} \mathcal{J}(\xi_i,\eta_j) W_i W_j \right)\end{aligned} \tag{4.34}$$

Since the stiffness matrix is symmetric for the overall system of equation (4.20), hence the electromechanical coupling sub-matrix $[K_{\phi u}]^{(e)}$ is computed by transposing $[K_{u\phi}]^{(e)}$, i.e., $[K_{\phi u}]^{(e)} = [K_{u\phi}]^{(e)^T}$.

The Gauss points coordinates and associated weights are summarized in table 4.1, according to Reddy's book [18], for the 2×2 and 3×3 rules. For 2×2 Gauss points, figure 4.4 show the locations of the integration points in the coordinate system of the master element.

Table 4.1: Gauss points and weights.

N_G	$\xi_i,\ \eta_i$	$W_i,\ W_j$
2	$\pm\sqrt{3}/3$	1
3	0	$8/9$
	$\pm\sqrt{3/5}$	$5/9$

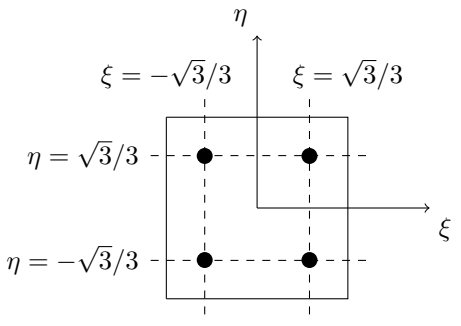

Figure 4.2: 2×2 Gauss points.

4.5 Post-Processing

Once the nodal variables are obtained, the generalized strains for a certain (x, y) point are evaluated from equation (4.8), while the generalized electric field components are obtained from equation (4.10). Then in order to compute the strains and the electric field components, for a certain z-coordinate, the associated transformation matrices $[S]_{(k)}$, in equation (3.22), and $[S_\phi]_{(k)}$, in equation (3.34), must be used. Once the strains and electric fields are determined, the stresses and electric displacements are derived from the layer's constitutive equations (2.15).

According to Barlow [40], the optimal points to compute the strains, and consequently the stresses, coincide with the reduced integration points, i.e, the 2×2 Gauss points used in the present models, represented in figure 4.2. Moreover, the same points are used to compute the electric field components and associated electric displacements. Consequently, local smoothing methods explained in Hinton et al. [41, 42] are used to directly extrapolate the secondary variables to the desired (x, y) location from the values at the Barlow's points.

Furthermore, and according to Reddy [17], since the present model assumes constant transverse shear stresses, one way to possibly improve the determination of these stresses is based on the direct integration of the equilibrium equations (2.21) in the transverse direction, for each k-layer as follows,

$$\tau_{xz}^{(k)} = -\int_{z_{(k)}^{inf}}^{z_{(k)}^{sup}} \left(\frac{\partial \sigma_{xx}^{(k)}}{\partial x} + \frac{\partial \tau_{xy}^{(k)}}{\partial y} \right) dz_k + C_1^{(k)}(x, y) \tag{4.35a}$$

$$\tau_{yz}^{(k)} = -\int_{z_{(k)}^{inf}}^{z_{(k)}^{sup}} \left(\frac{\partial \tau_{xy}^{(k)}}{\partial x} + \frac{\partial \sigma_{yy}^{(k)}}{\partial y} \right) dz_k + C_2^{(k)}(x, y) \tag{4.35b}$$

equipped with interlaminar continuity conditions at the interfaces between adjacent layers given by,

$$\begin{aligned} \tau_{xz}^{(k)}(x, y, z_{(k)}^{sup}) &= \tau_{xz}^{(k+1)}(x, y, z_{(k+1)}^{inf}) \\ \tau_{yz}^{(k)}(x, y, z_{(k)}^{sup}) &= \tau_{yz}^{(k+1)}(x, y, z_{(k+1)}^{inf}) \end{aligned} \tag{4.36}$$

and vanishing transverse shear stresses at the bottom surface of the plate as shown,

$$\tau_{xz}(x, y, -h/2) = \tau_{yz}(x, y, -h/2) = 0 \tag{4.37}$$

which yields null integration constants for the bottom surface, i.e., $C_1^{(b)} = C_2^{(b)} = 0$. The remaining integration constants, $C_1^{(k)}(x, y)$ and $C_2^{(k)}(x, y)$ are determined by imposing a continuous stress field at the layer's interfaces in order to obtain a quadratic variation that fulfills the C_z^0-requirements.

In order to evaluate the integrals in equation (4.35) as a function of the nodal DOFs, one could use the constitutive equation (2.18) for the in-plane stresses and then recall the generalized strains and electric fields definitions, (3.22) and (3.34), which can be related to the nodal variables through the equations (4.8) and (4.10), respectively. Following this approach, second order derivatives of the shape functions at the Barlow's points will appear, and must be properly accounted for in the coordinate transformation.

Chapter 5

Abaqus User-Element Implementation

In this chapter, the implementation of the developed LW electro-elastic plate elements, using the User-Defined Element (UEL) subroutine available in Abaqus, is discussed. This tool allows the user to define the element matrices needed for the desired finite element analysis, using Fortran programming language linked with a specific Abaqus input file. The main definitions regarding the UEL subroutine and its use are presented, as well as the several steps for the model implementation. Also, the input-file description is presented, regarding the mesh generation, boundary conditions and analysis options.

5.1 UEL Subroutine

Abaqus UEL subroutine translates all the developed theories and definitions in Fortran programming language. All element's definitions presented in Chapters 3 and 4, needed to build the mass and stiffness matrices must be included for the desired analysis, along with the associated post-processing requests. Moreover, for user defined boundary conditions, DISP subroutine must be attached to the UEL subroutine. The same happens for the user defined loads, where the DLOAD subroutine must be also included.

The UEL subroutine is called by Abaqus for every element within a mesh defined in the input file. According to the input file, Abaqus sends to the UEL block (figure 5.1) the nodal coordinates, and for each element computes the mass and stiffness matrices that will be later assembled in order to obtain the overall equilibrium equations. Also, Abaqus UEL subroutine takes advantage of some features available in Abaqus, such as the mesh generator, the assembly procedures, the specification of boundary conditions and prescription of loads, as well as the visualization module. Furthermore, the UEL subroutine avoids the user to program the element force vector in the subroutine, using a soft dummy element attached the UEL in the input file.

After the assembly of all elements, Abaqus solves the desired problem taking into account boundary conditions and loads as defined in the input file. Consequently, the solution vector containing the nodal DOFs is generated as an output. After this, Abaqus recalls the UEL subroutine for each element, adding the solution vector as an input to the UEL block, allowing post-processing procedures to be programmed within the subroutine, for the points (x, y) of interest through "IF" cycles. The results for each (x, y, z)

coordinates of interest are written in a *.log* text file generated by Abaqus.

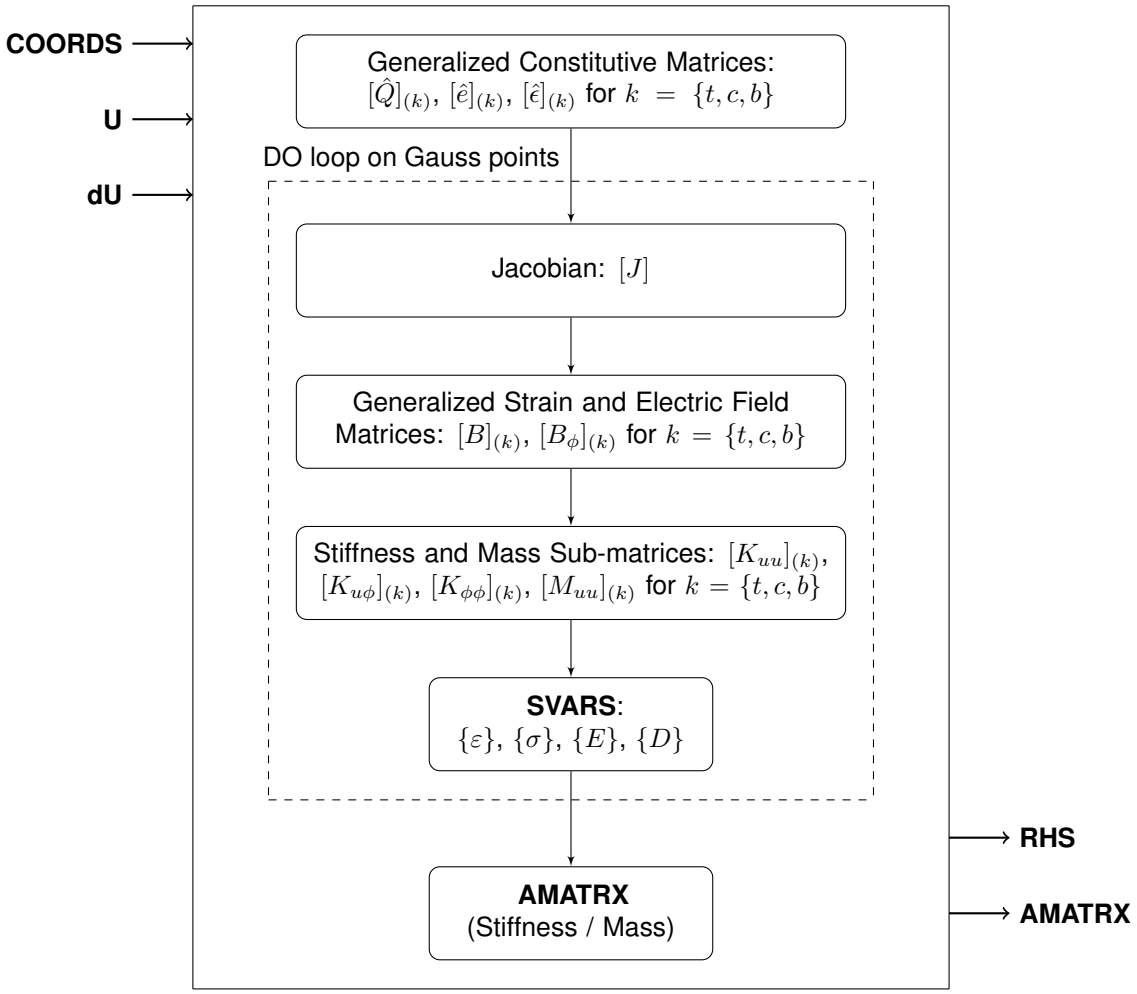

Figure 5.1: UEL Subroutine flow chart.

5.2 UEL Input and Output Variables

The input and output variables for the UEL subroutine are represented in figure 5.1, written in bold. According to Abaqus Manual [35], the input variable **COORDS** is a $2 \times n$ matrix, where n is the number of nodes per element, which contains the (x, y) coordinates of the element's nodes. Also, **U** is the solution vector that contains the values of the DOFs for each node at the end of the current time increment, while **dU** is a vector containing the incremental DOFs values for each node in the previous time increment.

The output variable **AMATRX** stands for the element mass and stiffness matrices, depending on the entries in the **LFLAGS** array, which is defined in the input file options. For each element, both mass and stiffness matrices must be calculated in the subroutine and then returned to Abaqus, having $N \times N$ components, where N is equal to the number of degrees of freedom per node times the number of nodes in the element, i.e., $N = 13 \times 8 = 104$ for the linear z-expansion of the electric potential and $N = 16 \times 8 = 128$ for the quadratic one.

For each k-discrete layer, with $k = \{t, c, b\}$, the generalized constitutive matrices in equation (3.44), likewise the $[P]_{(k)}$ matrices in equation (4.18), must be previously computed in order to be implemented

in a loop on the Gauss points, where the Jacobian matrix in equation (4.27) is employed to perform the coordinate transformation needed to build the generalized strain and electric field matrices in equations (4.8) and (4.10) necessary to numerically evaluate the mass and stiffness sub-matrices in equations (4.31), (4.32), (4.33) and (4.34).

The **RHS** is the internal force vector for the element with size N, defined as the product of the stiffness matrix **AMATRX** to the solution vector **U**. Furthermore, in figure 5.1, the **SVARS** is a vector which contains the element state-dependent variables, such as stresses and electric displacements, and it can also be considered as an output variable from the user's point of view, since it is not passed to Abaqus. The post-processing procedures explained in Section 4.5 are used, where strains, stresses, electric fields and electric displacements are evaluated at the Gauss points for all z-coordinates of interest and then direct local extrapolation is used, being the results included in the vector **SVARS**. Both **RHS** and **SVARS** are only calculated for static analysis.

5.3 Input File

The input file is a typical text file with *.inp* extension. It contains the key to call the UEL subroutine, by addressing the user-defined element to the desired mesh. In short, one could divide the input file in:

1. Nodes: definition of nodal coordinates and numbering.
2. User-element: declaration of the user element, defining the number of nodes, number of integration points, as well as the DOFs vector according to Abaqus convention.
3. Mesh: element definition in terms of element type and specification of the mesh in terms of nodes, where the UEL mesh is attached to an equal mesh of very soft S8R shell elements available in Abaqus, in order to apply forces without programming the force vector and also to visualize the in-plane variation of the displacements.
4. Assembly: assembling of all elements within a mesh and definition of node sets.
5. Analysis: specification of the type of analysis (static or frequency) and inherent options, such as the number of eigenvalues to extract in a frequency analysis.
6. Boundary Conditions: prescription of the essential boundary conditions for the desired node sets.
7. Loading: prescription of loading conditions.
8. Output: definition of the output request, only used for the nodal displacements.

Moreover, in order to link the input file with the UEL subroutine, both files must be in the same directory and the user must enter in the command window the following command:

abaqus job=input-file-name.inp user=UEL-subroutine-name.for

Chapter 6

Static Analysis Results

In this chapter, results for static analysis of two simply-supported piezoelectric multilayered composite plates, considering various aspect ratios, from thin to thicker plates, are presented. Both finite element models with linear z-expansion for the electric potential (UEL1) and quadratic z-expansion (UEL2), developed in Chapter 4, are compared with exact solutions reported by Moleiro et al. [13], available for the cases where the top surface of the plate is subjected to an applied bi-sinusoidal distributed transverse load $q(x, y)$ (monitoring mode) as follows,

$$q(x, y) = q_0 \sin\left(\frac{m\pi x}{a}\right) \sin\left(\frac{n\pi y}{b}\right) \tag{6.1}$$

and for the case where the same surface have instead of a load, an applied bi-sinusoidal electric potential $\hat{\phi}(x, y)$ (actuation mode) as shown:

$$\hat{\phi}(x, y) = \phi_0 \sin\left(\frac{m\pi x}{a}\right) \sin\left(\frac{n\pi y}{b}\right) \tag{6.2}$$

In the applied load case both top and bottom surfaces of the multilayered plate are grounded, while in the applied potential case, only the bottom surface is grounded. Also, on the simply-supported edges, the plate is grounded for both test cases. For numerical applications, an unitary value for the number of half-waves in the x and y-directions is considered, i.e., $m = n = 1$ in both equations (6.1) and (6.2), likewise an unitary amplitude values, meaning that $\phi_0 = 1$ V and $q_0 = 1$ N/m^2 (upwards).

6.1 Problem Description

Two symmetric stacking schemes are considered as test cases in line with some numerical applications reported by Moleiro et al. [13], where a multilayered composite core made of three graphite-epoxy unidirectional fiber reinforced layers is bonded with piezoelectric face layers as follows:

- Case 1: Transversely isotropic piezoceramic PZT-4 face layers [PZT-4/0° /90° /0° /PZT-4]
- Case 2: Orthotropic piezoelectric polymer PVDF face layers of 0° [PVDF/90° /0° /90° /PVDF]

The associated engineering constants, piezoelectric coefficients and relative dielectric constants are

listed in table 6.1. Both multilayered plates are square plates ($a = b$), with total thickness $h = 0.01$ m. Each piezoelectric layer has $h/10$ of thickness, while the multilayered composite core has $8h/10$ equal thickness composite layers. The side dimension a is determined by the plate's aspect ratio $a/h = 100,\ 20,\ 10$ or 4.

Table 6.1: Material properties, Heyliger [9].

Properties	Graphite-Epoxy	PZT-4	PVDF
E_1 (GPa)	132.28	81.3	237.0
E_2 (GPa)	10.756	81.3	23.2
E_3 (GPa)	10.756	64.5	10.5
G_{12} (GPa)	5.654	30.6	6.43
G_{13} (GPa)	5.654	25.6	4.40
G_{23} (GPa)	3.606	25.6	2.15
ν_{12}	0.24	0.33	0.154
ν_{13}	0.24	0.43	0.178
ν_{23}	0.49	0.43	0.177
e_{15} (C/m^2)	0	12.72	-0.01
e_{24} (C/m^2)	0	12.72	-0.01
e_{31} (C/m^2)	0	-5.20	-0.13
e_{32} (C/m^2)	0	-5.20	-0.14
e_{33} (C/m^2)	0	15.08	-0.28
ϵ_{11}/ϵ_0 *	3.5	1475	12.50
ϵ_{22}/ϵ_0 *	3.0	1475	11.98
ϵ_{33}/ϵ_0 *	3.0	1300	11.98
ρ (kg/m^3)	1578	7600	1780

*$\epsilon_0 = 8.85 \times 10^{-12}$ F/m (vacuum dielectric constant)

From the point of view of the present layerwise FSDT model and following Reddy's book [17], the simply-supported boundary conditions on the plate edges, represented in figure 6.1, imply that for the three discrete layers, with $k = \{t, c, b\}$, the following conditions:

$$u_{0_{(k)}} = w_0 = \theta_{x_{(k)}} = 0 \ \text{ at } y = 0, a \tag{6.3a}$$

$$v_{0_{(k)}} = w_0 = \theta_{y_{(k)}} = 0 \ \text{ at } x = 0, a \tag{6.3b}$$

One should note that from the chosen mechanical DOFs vector (3.11), the only rotations considered as independent unknowns are the composite core rotations θ_{x_c} and θ_{y_c}, which are the only ones that must be constrained regarding equations (6.3).

The electric boundary conditions are applied on the electric potentials DOFs in equation (3.29). Also, on the simply-supported edges, the plate is grounded across the thickness, which for the present model requires that

$$\phi_i = 0 \ \text{ at } x = 0, a \text{ and } y = 0, a \tag{6.4}$$

with $i = \{1, 2, 3, 4\}$ for UEL1, while $i = \{1, 2, ..., 7\}$ for UEL2. Furthermore, in order to prescribe an electric potential at the bottom surface of the plate, the DOF ϕ_1 must be prescribed, as well as the DOF ϕ_4 for the top surface, on both UEL models.

The in-plane locations for the desired variables are chosen in order to correspond to its absolute

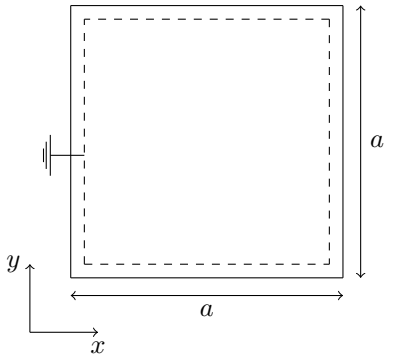

Figure 6.1: Simply-supported square plate, grounded in the edges.

maximum. According to the exact solutions of Heyliger [2] and in Moleiro et al. [11], the variables w, ϕ, σ_{xx}, σ_{yy} and D_z are given at the plate's center $(a/2, a/2)$, while u, τ_{xz} and D_x are determined for $(0, a/2)$, as well as v, τ_{yz} and D_y at $(a/2, 0)$. The absolute maximum for τ_{xy} occurs at the corner $(0, 0)$.

It should be enhanced that all results are given at the aforementioned in-plane locations, in S.I. units according to table 2.1. Moreover, in the presentation of the predicted transverse shear stresses by the developed models, the suffix (C) stands for constitutively derived stresses, while the suffix (E) stands for the equilibrium derived ones. Noting that in UEL1 only constitutively derived stresses are considered, where the suffix (C) is omitted for brevity.

6.2 Convergence Study

In order to choose an appropriate mesh for static analysis, a convergence study is conducted for UEL2 concerning the piezoelectric composite plate of Case 1, with $a/h = 20$, under applied load. The chosen primary variables for the convergence test are the transverse displacement w and the electric potential ϕ, likewise the in-plane normal stress σ_{xx}, as a representative secondary variable.

Table 6.2: Convergence study for UEL2 in static analysis of Case 1, with $a/h = 20$, under applied load.

Mesh	$w(a/2, a/2, 0) \times 10^{11}$	δ_w (%)	$\phi(a/2, a/2, 2h/5) \times 10^3$	δ_ϕ (%)	$\sigma_{xx}(a/2, a/2, h/2)$	δ_σ (%)
6x6	70.8754	0.49	1.6452	1.61	132.292	4.16
10x10	70.8971	0.46	1.6349	0.98	129.711	2.13
20x20	70.8982	0.46	1.6249	0.36	128.621	1.27
30x30	70.9002	0.46	1.6139	0.32	126.877	0.10
Exact	71.2282		1.6191		127.010	

$\delta_x\ (\%) = (x_{\text{UEL}} - x_{\text{Exact}}) \times 100 / x_{\text{Exact}}$

The results from table 6.2 show that even for the coarse mesh with 6×6 elements, the results are in good agreement with the exact solutions. Also, one can see a slower rate of convergence for the electric potential comparatively to the transverse displacement, being the in-plane stress the variable with slower rate of convergence, as expected.

In order to better predict the secondary variables such as the stresses or the electric displacements, the most refined mesh with 30×30 elements is chosen for all static analysis, since the additional computational effort to the 20×20 mesh is negligible when compared to the achieved level of accuracy for

all variables. The same mesh is used for UEL1 due to a similar convergence behaviour of the solution when using the UEL1 model instead of UEL2.

6.3 Case 1 - Transversely Isotropic Piezoelectric Layers

Static analysis results for simply-supported plates of Case 1, [PZT-4/0° /90° /0° /PZT-4], with applied bi-sinusoidal load or potential, from thin to thicker plates.

6.3.1 Thin Plates

Concerning the analysis of thin plates with $a/h = 100$, the results obtained with UEL2, presented in tables 6.3 and 6.5 for applied load, and in tables 6.4 and 6.6 for applied potential, show the through-thickness evolution of some representative mechanical and electrical variables, considering for this, both bottom and top transverse coordinates of each layer. Likewise, tables E.1 and E.2, in the Appendix E, show the same variables obtained with UEL1 model.

Table 6.3: Results Case 1, with $a/h = 100$, under applied load.

z/h	$u \times 10^{12}$		$w \times 10^{11}$	$\phi \times 10^{3}$		σ_{xx}		$D_x \times 10^{12}$	
	Exact	UEL2	Exact	Exact	UEL2	Exact	UEL2	Exact	UEL2
1/2	-6492.82	-6497.32	41457.67	0.00	0.00	3145.3	3149.9	0.00	2792.06
2/5	-5190.58	-5194.47	41459.50	40.60	40.19	2514.7	2518.4	3699.50	1143.69
2/5	-5190.58	-5194.47	41459.50	40.60	40.19	2211.5	2215.2	-3.95	-3.91
2/15	-1726.70	-1731.49	41461.97	40.60	40.18	735.8	738.4	-3.95	-3.91
2/15	-1726.70	-1731.49	41461.97	40.60	40.18	73.1	73.0	-3.39	-3.35
-2/15	1727.61	1731.49	41461.96	40.61	40.18	-72.6	-73.0	-3.39	-3.35
-2/15	1727.61	1731.49	41461.96	40.61	40.18	-735.9	-738.4	-3.95	-3.91
-2/5	5191.50	5194.47	41459.47	40.62	40.19	-2211.5	-2215.2	-3.95	-3.91
-2/5	5191.50	5194.47	41459.47	40.62	40.19	-2514.8	-2518.4	3698.84	1143.69
-1/2	6493.74	6497.32	41457.64	0.00	0.00	-3145.4	-3149.9	0.00	2792.06
UEL2			41478.06						

Table 6.4: Results Case 1, with $a/h = 100$, under applied potential.

z/h	$u \times 10^{12}$		$w \times 10^{11}$	ϕ		σ_{xx}		$D_x \times 10^{8}$	
	Exact	UEL2	Exact	Exact	UEL2	Exact	UEL2	Exact	UEL2
1/2	-2.949	-2.864	-1.203	1.0000	1.0000	-2.521	-2.489	-6.088	-6.097
2/5	-1.425	-1.438	-1.198	0.9998	0.9998	-2.836	-2.809	-6.087	-6.096
2/5	-1.425	-1.438	-1.198	0.9998	0.9998	0.615	0.607	-0.010	-0.010
2/15	-1.524	-1.524	-1.197	0.6665	0.6665	0.657	0.650	-0.006	-0.006
2/15	-1.524	-1.524	-1.197	0.6665	0.6665	0.072	0.072	-0.006	-0.006
-2/15	-1.624	-1.611	-1.196	0.3333	0.3333	0.077	0.076	-0.003	-0.003
-2/15	-1.624	-1.611	-1.196	0.3333	0.3333	0.700	0.693	-0.003	-0.003
-2/5	-1.726	-1.697	-1.194	0.0002	0.0002	0.743	0.736	0.000	0.000
-2/5	-1.726	-1.697	-1.194	0.0002	0.0002	-2.688	-2.660	-0.001	-0.001
-1/2	-1.763	-1.747	-1.190	0.0000	0.0000	-2.670	-2.641	0.000	0.000
UEL2			-1.205						

For both applied load and applied potential test cases, the displacements and electric potential are in agreement with the exact solutions, as well as the in-plane stresses and in-plane electric displacements. However, for the applied load case, due to the FSDT assumption of constant transverse shear strains, and recalling the constitutive equations (2.15), table 6.3 and table E.1 (in Appendix E), show that both

Table 6.5: Transverse electric displacement and transverse shear stresses for Case 1, with $a/h = 100$, under applied load.

z/h	$D_z \times 10^{12}$		τ_{xz}			τ_{yz}		
	Exact	UEL2	Exact	UEL2 (C)	UEL2 (E)	Exact	UEL2 (C)	UEL2 (E)
1/2	12.026	12.283	0.000	5.619	0.000	0.000	5.621	0.000
2/5	-0.030	-0.026	12.421	7.225	8.887	12.424	7.227	8.878
2/5	-0.030	-0.061	12.421	25.234	8.887	12.424	12.148	8.878
2/15	0.032	-0.031	25.795	25.234	21.226	14.676	12.148	10.145
2/15	0.032	-0.031	25.795	16.093	21.226	14.676	19.048	10.145
-2/15	0.093	0.031	25.796	16.093	21.226	14.676	19.048	10.145
-2/15	0.093	0.031	25.796	25.234	21.226	14.676	12.148	10.145
-2/5	0.155	0.092	12.422	25.234	8.887	12.425	12.148	8.918
-2/5	0.155	0.026	12.422	7.225	8.887	12.425	7.227	8.918
-1/2	-11.900	-12.283	0.000	5.619	0.000	0.000	5.621	0.000

Table 6.6: Transverse electric displacement and transverse shear stresses for Case 1, with $a/h = 100$, under applied potential.

z/h	$D_z \times 10^{8}$		τ_{xz}			τ_{yz}		
	Exact	UEL2	Exact	UEL2 (C)	UEL2 (E)	Exact	UEL2 (C)	UEL2 (E)
1/2	-0.370	-0.371	0.000	0.006	0.000	0.000	0.006	0.000
2/5	-0.332	-0.332	-0.007	-0.003	-0.003	-0.006	-0.003	-0.002
2/5	-0.332	-0.332	-0.007	0.000	-0.003	-0.006	0.000	-0.002
2/15	-0.332	-0.332	-0.001	0.000	0.002	-0.005	0.000	-0.002
2/15	-0.332	-0.332	-0.001	0.000	0.002	-0.005	0.000	-0.002
-2/15	-0.332	-0.332	0.000	0.000	0.002	0.005	0.000	0.007
-2/15	-0.332	-0.332	0.000	0.000	0.002	0.005	0.000	0.007
-2/5	-0.332	-0.332	0.007	0.000	0.008	0.006	0.000	0.008
-2/5	-0.332	-0.332	0.007	0.009	0.008	0.006	0.008	0.008
-1/2	-0.332	-0.332	0.000	-0.001	0.000	0.000	-0.001	0.000

UEL1 and UEL2 models are not capable to achieve the vanishing in-plane electric displacements for both top and bottom surfaces of the plate shown by the exact solutions. However, from the results for the applied potential case, shown in tables 6.4 and E.2, one can see that the in-plane electric displacements are well predicted by both UEL models.

Also, for both cases, tables 6.5 and 6.6 demonstrate that, besides the fact that the transverse electric displacement is constitutively derived, and consequently discontinuous, the results of the UEL2 follow approximately the exact solutions for thin plates, which is a benefit of the linear z-expansion of the transverse electric field of UEL2, over the constant one assumed in UEL1 (tables E.1 and E.2).

Furthermore, the constitutively derived transverse shear stresses, for both UEL models and loading cases, have an interlaminar discontinuous behaviour, with non-zero transverse shear stresses at the plate's top and bottom surfaces. Hence, the equilibrium derived stresses seem to be the more precise, accounting to the C_z^0-requirements and stress free boundary conditions.

6.3.2 Moderately Thick Plates

For moderately thick plates with $a/h = 20$, tables 6.7, 6.9 and 6.11 show both UEL1 and UEL2 results for the applied load case, while tables 6.8, 6.10 and 6.12 show the same results for the applied potential case. Also, for plates with $a/h = 10$, tables 6.13 and 6.15 show the UEL2 results for the applied load

case, while tables 6.14 and 6.16 concern the applied potential case.

Similarly to the thin plates, for both applied load and potential cases, tables 6.7 and 6.8 suggest that even for plates with $a/h = 20$, the displacements, in figure 6.2 and 6.3, and the electric potential, in figure 6.5, are almost independent on the linear or quadratic z-expansion used for the electric potential, being both good approximations to the exact solutions for thin and moderately thick plates. Figure 6.4 shows the in-plane distribution of the transverse displacement for both applied load and applied potential cases, with UEL2 model.

However, the UEL2 displacements and electric potential are slightly more precise than UEL1 within the piezoelectric layers, for both monitoring and actuation modes. Hence, the UEL2 quadratic z-expansion of the electric potential improves the evaluation of the transverse electric field comparatively to UEL1 model, predicting accurate in-plane normal stresses, shown in figures 6.6 and 6.7, and enhancing the transverse electric displacements represented in figure 6.10.

In fact, tables 6.9 and 6.10 demonstrate that in the applied potential case the UEL2 electric displacements almost match the exact solutions, opposing to the applied load case, where non-vanishing in-plane electric displacements on the plate's top and bottom surfaces appear due to the FSDT assumptions, represented in figures 6.8 and 6.9, as well as a discontinuous transverse electric displacement due to the constitutive approach.

Table 6.7: Results Case 1, with $a/h = 20$, under applied load.

z/h	$u \times 10^{12}$			$w \times 10^{11}$	$\phi \times 10^{3}$			σ_{xx}		
	Exact	UEL1	UEL2	Exact	Exact	UEL1	UEL2	Exact	UEL1	UEL2
1/2	-51.970	-52.118	-52.093	71.066	0.000	0.000	0.000	127.010	124.078	126.877
9/20	-46.399	-46.569	-46.547	71.105	0.858	0.807	0.855	113.511	113.481	113.428
2/5	-40.845	-41.019	-41.000	71.139	1.619	1.615	1.614	100.040	102.885	99.979
2/5	-40.845	-41.019	-41.000	71.139	1.619	1.615	1.614	87.380	87.498	87.457
2/15	-12.922	-13.673	-13.667	71.222	1.619	1.615	1.607	27.808	29.166	29.152
2/15	-12.922	-13.673	-13.667	71.222	1.619	1.615	1.607	3.099	2.895	2.893
0	0.097	0.000	0.000	71.228	1.621	1.615	1.606	0.225	0.000	0.000
-2/15	13.112	13.673	13.667	71.212	1.625	1.615	1.607	-2.648	-2.895	-2.893
-2/15	13.112	13.673	13.667	71.212	1.625	1.615	1.607	-27.862	-29.166	-29.152
-2/5	41.025	41.019	41.000	71.110	1.638	1.615	1.614	-87.409	-87.498	-87.457
-2/5	41.025	41.019	41.000	71.110	1.638	1.615	1.614	-100.094	-102.885	-99.979
-9/20	46.576	46.569	46.547	71.075	0.867	0.807	0.855	-113.559	-113.481	-113.428
-1/2	52.145	52.118	52.093	71.036	0.000	0.000	0.000	-127.052	-124.078	-126.877
UEL1				70.933						
UEL2				70.900						

Table 6.8: Results Case 1, with $a/h = 20$, under applied potential.

z/h	$u \times 10^{12}$			$w \times 10^{11}$	ϕ			σ_{xx}		
	Exact	UEL1	UEL2	Exact	Exact	UEL1	UEL2	Exact	UEL1	UEL2
1/2	-6.845	-6.800	-6.815	-1.218	1.0000	1.0000	1.0000	2.258	5.633	2.391
9/20	-3.039	-3.010	-3.023	-1.209	0.9997	0.9998	0.9997	-1.670	-1.631	-1.599
2/5	0.766	0.780	0.769	-1.206	0.9995	0.9995	0.9995	-5.598	-8.894	-5.590
2/5	0.766	0.780	0.769	-1.206	0.9995	0.9995	0.9995	-1.634	-1.685	-1.662
2/15	0.265	0.278	0.275	-1.207	0.6643	0.6664	0.6645	-0.566	-0.607	-0.599
2/15	0.265	0.278	0.275	-1.207	0.6643	0.6664	0.6645	-0.058	-0.061	-0.060
0	0.024	0.028	0.028	-1.208	0.4977	0.4999	0.4977	-0.006	-0.007	-0.007
-2/15	-0.217	-0.223	-0.219	-1.208	0.3316	0.3333	0.3314	0.046	0.046	0.045
-2/15	-0.217	-0.223	-0.219	-1.208	0.3316	0.3333	0.3314	0.463	0.472	0.464
-2/5	-0.717	-0.724	-0.713	-1.206	0.0002	0.0002	0.0002	1.528	1.551	1.527
-2/5	-0.717	-0.724	-0.713	-1.206	0.0002	0.0002	0.0002	-1.905	-1.795	-1.872
-9/20	-0.811	-0.823	-0.810	-1.204	0.0001	0.0001	0.0001	-1.676	-1.610	-1.641
-1/2	-0.905	-0.922	-0.908	-1.201	0.0000	0.0000	0.0000	-1.448	-1.426	-1.411
UEL1				-1.232						
UEL2				-1.213						

Table 6.9: Electric displacements for Case 1, with $a/h = 20$, under applied load.

z/h	$D_x \times 10^{12}$			$D_y \times 10^{12}$			$D_z \times 10^{12}$		
	Exact	UEL1	UEL2	Exact	UEL1	UEL2	Exact	UEL1	UEL2
1/2	0.000	559.978	560.267	0.000	563.143	563.431	12.182	-2604.475	11.280
9/20	394.345	394.329	384.886	397.764	397.496	388.051	9.013	52.827	5.187
2/5	744.657	228.681	229.131	751.494	231.849	232.298	-0.030	2615.040	-0.906
2/5	-0.788	-0.786	-0.786	-0.676	-0.674	-0.783	-0.030	0.000	-0.091
2/15	-0.788	-0.786	-0.783	-0.676	-0.674	-0.671	0.031	0.000	-0.030
2/15	-0.676	-0.674	-0.671	-0.788	-0.786	-0.783	0.031	0.000	-0.030
0	-0.677	-0.674	-0.671	-0.789	-0.786	-0.783	0.062	0.000	0.000
-2/15	-0.678	-0.674	-0.671	-0.791	-0.786	-0.783	0.093	0.000	0.030
-2/15	-0.791	-0.786	-0.783	-0.678	-0.674	-0.671	0.093	0.000	0.030
-2/5	-0.797	-0.786	-0.786	-0.683	-0.674	-0.673	0.154	0.000	0.091
-2/5	741.290	228.681	229.131	749.347	231.849	232.298	0.154	-2615.040	0.906
-9/20	392.653	394.329	384.886	396.681	397.496	388.051	-8.857	-5.283	-5.187
-1/2	0.000	559.978	560.267	0.000	563.143	563.431	-12.014	2604.475	-11.280

Table 6.10: Electric displacements for Case 1, with $a/h = 20$, under applied potential.

z/h	$D_x \times 10^{8}$			$D_y \times 10^{8}$			$D_z \times 10^{8}$		
	Exact	UEL1	UEL2	Exact	UEL1	UEL2	Exact	UEL1	UEL2
1/2	-30.442	-30.484	-30.484	-30.442	-30.484	-30.484	-1.292	-0.994	-1.294
9/20	-30.431	-30.479	-30.478	-30.431	-30.479	-30.478	-0.814	-0.815	-0.815
2/5	-30.426	-30.474	-30.474	-30.426	-30.474	-30.474	-0.336	-0.636	-0.336
2/5	-0.049	-0.049	-0.049	-0.042	-0.042	-0.042	-0.336	-0.332	-0.335
2/15	-0.032	-0.032	-0.032	-0.028	-0.028	-0.028	-0.332	-0.332	-0.333
2/15	-0.028	-0.028	-0.028	-0.032	-0.032	-0.032	-0.332	-0.332	-0.333
0	-0.021	-0.021	-0.021	-0.024	-0.024	-0.024	-0.331	-0.332	-0.332
-2/15	-0.014	-0.014	-0.014	-0.016	-0.016	-0.016	-0.331	-0.332	-0.331
-2/15	-0.016	-0.016	-0.016	-0.014	-0.014	-0.014	-0.331	-0.332	-0.331
-2/5	0.000	0.000	0.000	0.000	0.000	-0.001	-0.330	-0.332	-0.329
-2/5	-0.006	-0.005	-0.005	-0.006	-0.005	-0.005	-0.330	-0.326	-0.330
-9/20	-0.003	-0.003	-0.003	-0.003	-0.003	-0.003	-0.330	-0.330	-0.330
-1/2	0.000	-0.001	-0.001	0.000	-0.001	-0.001	-0.330	-0.335	-0.330

Table 6.11: Transverse shear stresses for Case 1, with $a/h = 20$, under applied load.

z/h	τ_{xz}				τ_{yz}			
	Exact	UEL1	UEL2 (C)	UEL2 (E)	Exact	UEL1	UEL2 (C)	UEL2 (E)
1/2	0.000	1.127	1.276	0.000	0.000	1.133	1.134	0.000
9/20	1.322	1.288	1.298	0.942	1.326	1.295	1.305	0.946
2/5	2.495	1.450	1.450	1.779	2.504	1.456	1.457	1.789
2/5	2.495	5.026	5.238	1.779	2.504	2.444	2.443	1.789
2/15	5.106	5.026	5.238	4.214	2.969	2.444	2.443	2.043
2/15	5.106	3.206	3.204	4.214	2.969	3.833	3.831	2.043
0	5.157	3.206	3.204	4.244	3.305	3.833	3.831	2.355
-2/15	5.098	3.206	3.204	4.214	2.960	3.833	3.831	2.043
-2/15	5.098	5.026	5.024	4.214	2.960	2.444	2.443	2.043
-2/5	2.491	5.026	5.024	1.779	2.512	2.444	2.443	1.797
-2/5	2.491	1.450	1.450	1.779	2.512	1.456	1.457	1.797
-9/20	1.319	1.288	1.298	0.942	1.330	1.295	1.305	0.951
-1/2	0.000	1.127	1.128	0.000	0.000	1.133	1.134	0.000

Table 6.12: Transverse shear stresses for Case 1, with $a/h = 20$, under applied potential.

z/h	τ_{xz}				τ_{yz}			
	Exact	UEL1	UEL2 (C)	UEL2 (E)	Exact	UEL1	UEL2 (C)	UEL2 (E)
1/2	0.000	0.089	0.088	0.000	0.000	0.088	0.087	0.000
9/20	0.039	0.040	0.028	0.060	0.039	0.039	0.027	0.064
2/5	0.019	-0.010	-0.011	0.032	0.019	-0.010	-0.011	0.036
2/5	0.019	-0.022	-0.021	0.032	0.019	0.007	0.008	0.036
2/15	-0.031	-0.022	-0.021	-0.016	0.010	0.007	0.008	0.028
2/15	-0.031	-0.014	-0.013	-0.016	0.010	0.011	0.012	0.028
0	-0.032	-0.014	-0.013	-0.016	0.002	0.011	0.012	0.018
-2/15	-0.031	-0.014	-0.013	-0.016	0.006	0.011	0.012	0.021
-2/15	-0.031	-0.022	-0.021	-0.016	0.006	0.007	0.008	0.021
-2/5	0.014	-0.022	-0.021	0.026	0.014	0.007	0.008	0.025
-2/5	0.014	0.027	0.028	0.026	0.014	0.027	0.028	0.025
-9/20	0.006	0.006	0.006	0.012	0.006	0.006	0.006	0.012
-1/2	0.000	-0.015	-0.015	0.000	0.000	-0.015	-0.015	0.000

Regarding the determination of the transverse shear stresses, similar results are found in tables 6.11 and 6.12 for both UEL models when the constitutive equation is employed. The equilibrium derived stresses differ from the exact ones, however the achieved through-thickness variation is the same as the exact solution, where the stress-free boundary conditions and interlaminar continuity conditions are fulfilled, as can be seen in figures 6.11 and 6.12.

Ultimately, from these figures, an additional correction factor, dependent on the loading and boundary conditions, seems to be needed to fit the predicted equilibrium derived stresses to the exact results. The average ratio between the equilibrium derived stresses and the exact ones is near of 0.74 for the applied load case, while in applied potential is near of 1.16.

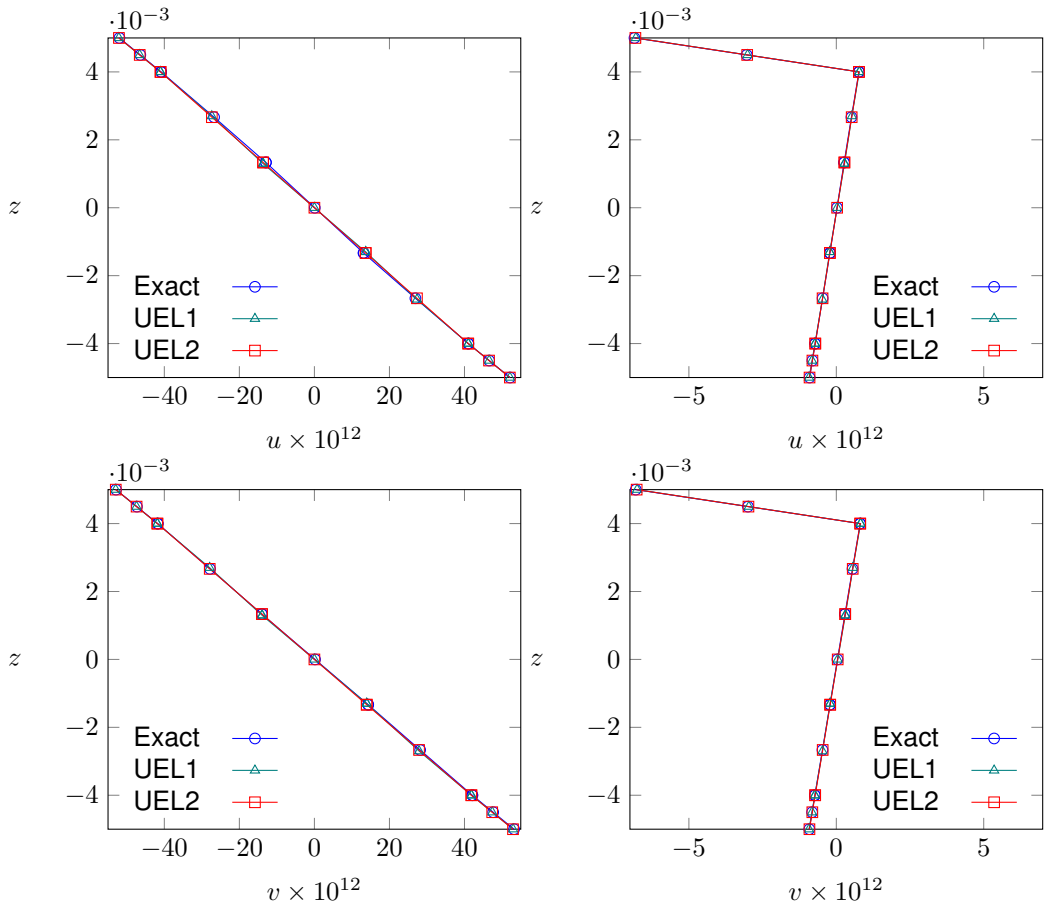

Figure 6.2: In-plane displacements (u, v) for Case 1, with $a/h = 20$, under applied load (on the left) and applied potential (on the right).

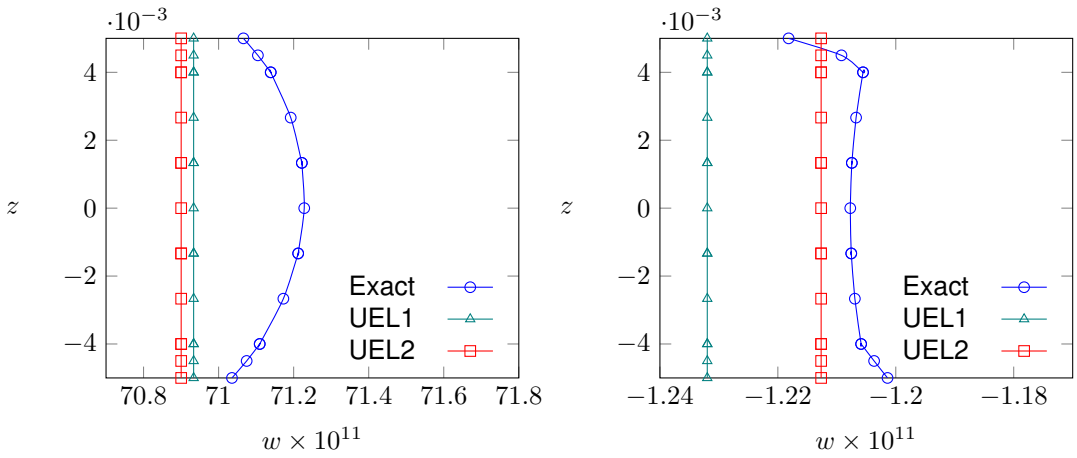

Figure 6.3: Transverse displacement w for Case 1, with $a/h = 20$, under applied load (on the left) and applied potential (on the right).

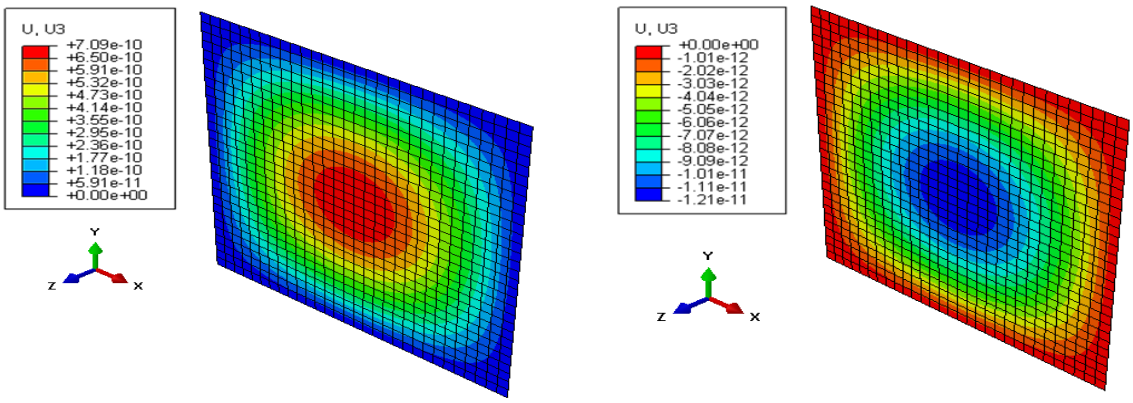

Figure 6.4: In-plane variation of the transverse displacement w for Case 1, with $a/h = 20$, under applied load (on the left) and applied potential (on the right) with UEL2.

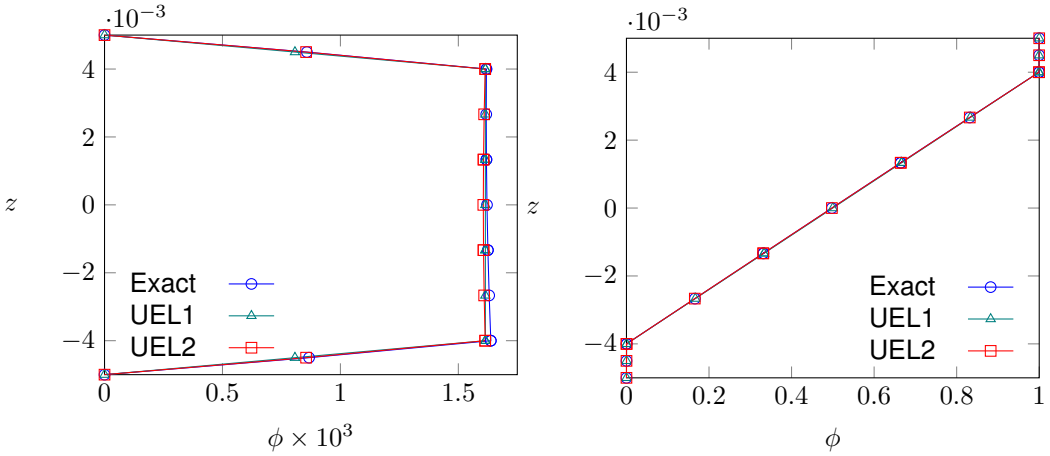

Figure 6.5: Electric potential ϕ for Case 1, with $a/h = 20$, under applied load (on the left) and applied potential (on the right).

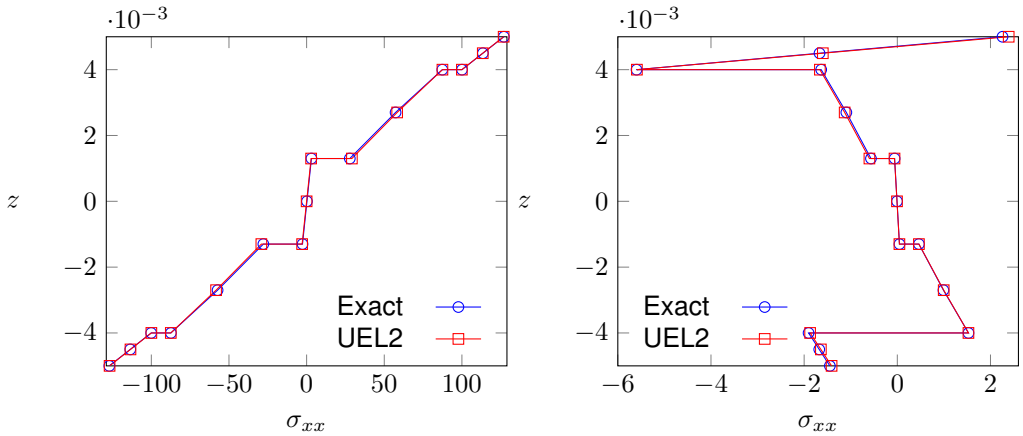

Figure 6.6: In-plane normal stress σ_{xx} for Case 1, with $a/h = 20$, under applied load (on the left) and applied potential (on the right).

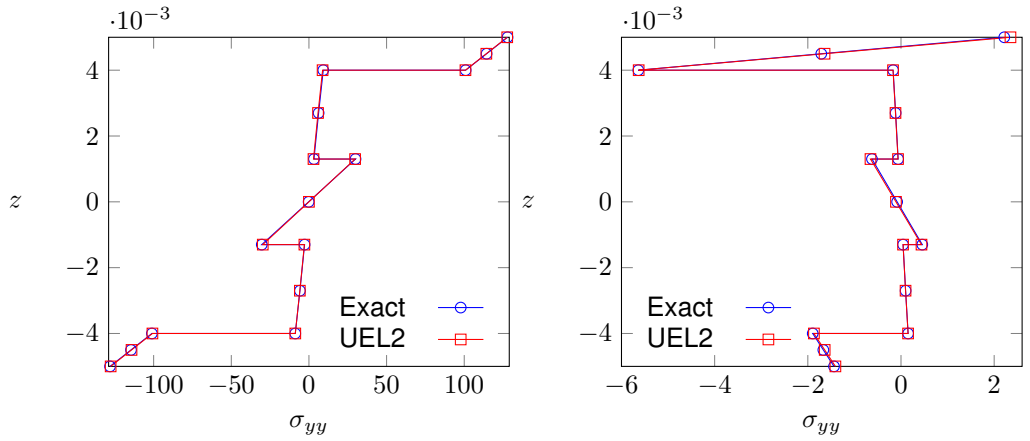

Figure 6.7: In-plane normal stress σ_{yy} for Case 1, with $a/h = 20$, under applied load (on the left) and applied potential (on the right).

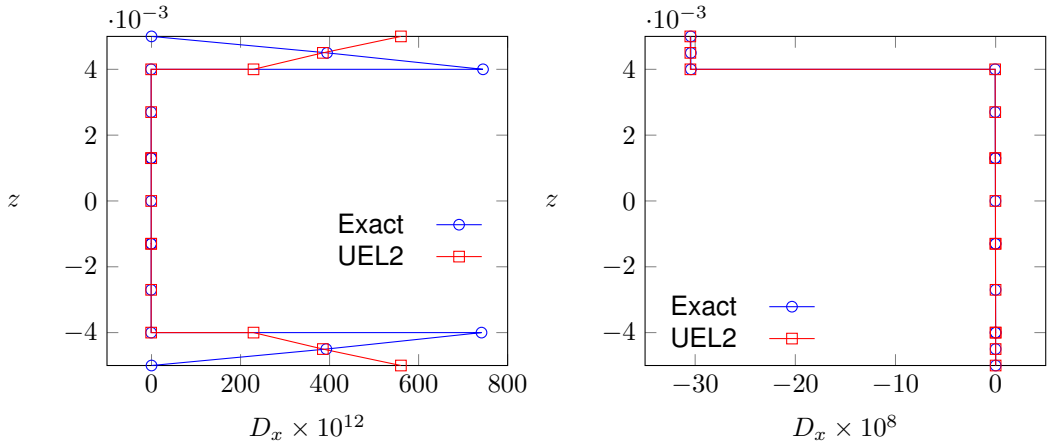

Figure 6.8: In-plane electric displacement D_x for Case 1, with$a/h = 20$, under applied load (on the left) and applied potential (on the right).

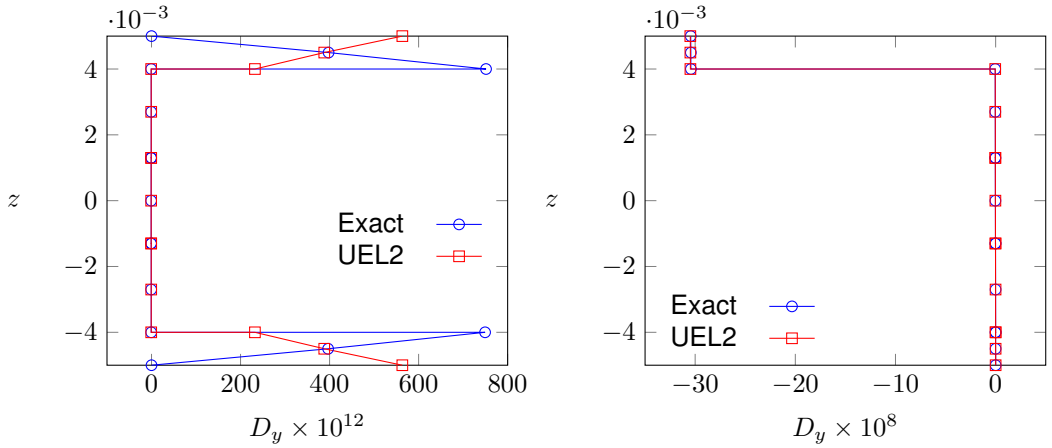

Figure 6.9: In-plane electric displacement D_y for Case 1, with $a/h = 20$, under applied load (on the left) and applied potential (on the right).

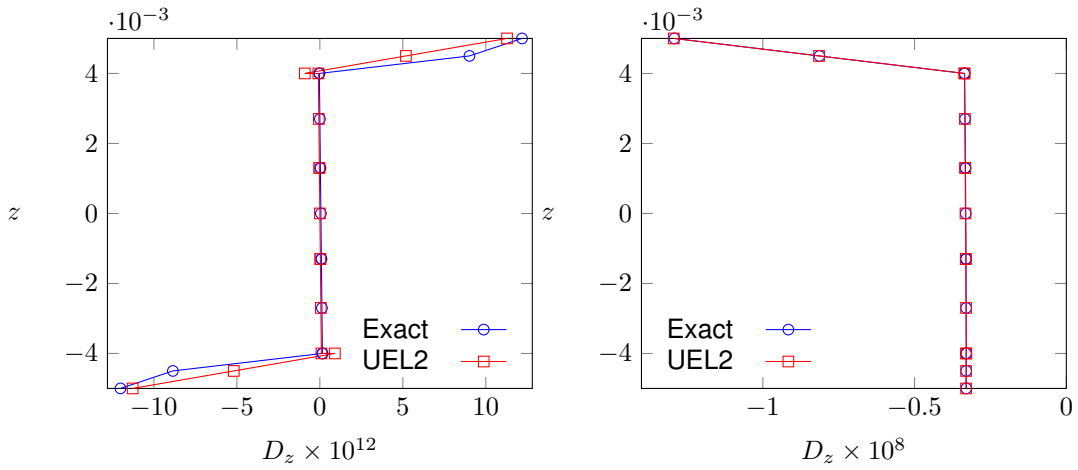

Figure 6.10: Transverse electric displacement D_z for Case 1, with $a/h = 20$, under applied load (on the left) and applied potential (on the right).

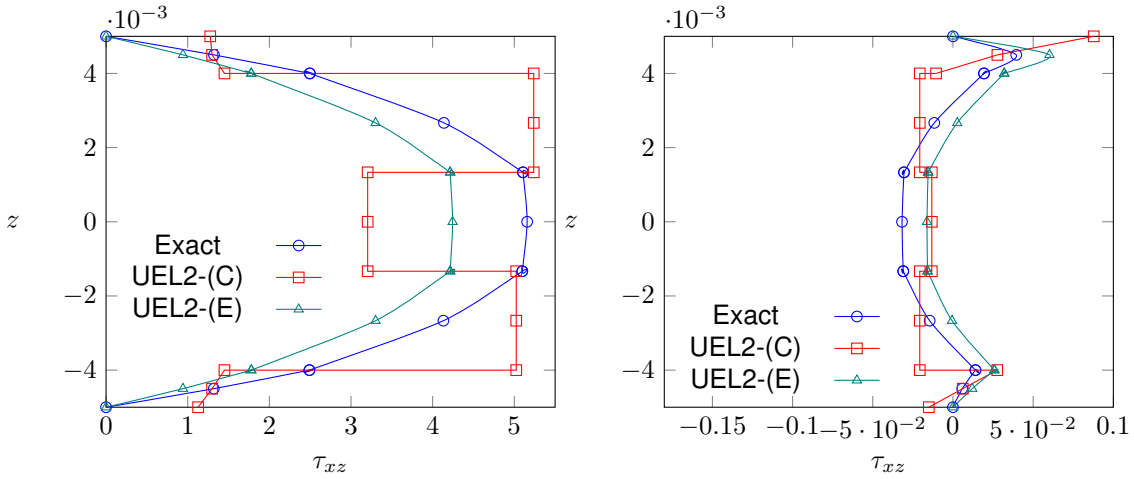

Figure 6.11: Shear stress τ_{xz} for Case 1, with $a/h = 20$, under applied load (on the left) and applied potential (on the right).

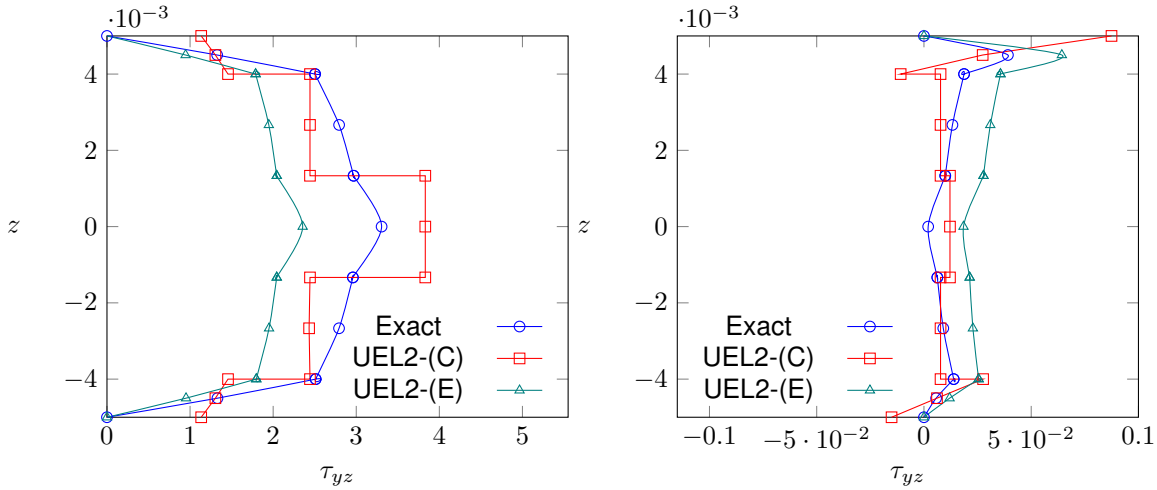

Figure 6.12: Shear stress τ_{yz} for Case 1, with $a/h = 20$, under applied load (on the left) and applied potential (on the right).

Due to the FSDT assumptions, one shall expect that the shear effects become more important for the analysis of thicker plates, particularly for $a/h = 10$ rather than for $a/h = 20$. These effects are mainly felt in the applied load case (table 6.13), where the achieved displacements start to differ to the exact ones, and consequently the in-plane stresses within the multilayered composite core follow the same tendency. Hence, the accuracy of both constitutively derived and equilibrium derived transverse shear stresses is also affected, as can be seen in table 6.5.

On the other hand, for the applied potential case, tables 6.14 and 6.16 demonstrate that UEL2 results remain in relatively good agreement with the exact solutions, even for plates with $a/h = 10$.

Table 6.13: Results Case 1, with $a/h = 10$, under applied load.

z/h	$u \times 10^{12}$		$w \times 10^{11}$	$\phi \times 10^{3}$		σ_{xx}		$D_x \times 10^{12}$	
	Exact	UEL2	Exact	Exact	UEL2	Exact	UEL2	Exact	UEL2
1/2	-6.540	-6.573	5.370	0.00000	0.00000	32.727	32.421	0.000	283.161
2/5	-4.872	-4.926	5.388	0.40034	0.40825	24.618	24.425	380.435	115.545
2/5	-4.872	-4.926	5.388	0.40034	0.40825	21.129	21.036	-0.390	-0.398
2/15	-1.285	-1.642	5.396	0.40025	0.40198	5.758	7.012	-0.390	-0.392
2/15	-1.285	-1.642	5.396	0.40025	0.40198	0.916	0.703	-0.334	-0.336
0	0.056	0.000	5.393	0.40249	0.40119	0.222	0.000	-0.336	-0.335
-2/15	1.392	1.642	5.386	0.40626	0.40198	-0.470	-0.703	-0.339	-0.336
-2/15	1.392	1.642	5.386	0.40626	0.40198	-5.857	-7.012	-0.396	-0.392
-2/5	4.957	4.926	5.358	0.41845	0.40825	-21.136	-21.036	-0.407	-0.398
-2/5	4.957	4.926	5.358	0.41845	0.40825	-24.649	-24.425	373.180	115.545
-1/2	6.615	6.573	5.340	0.00000	0.00000	-32.712	-32.421	0.000	283.161
UEL2			5.313						

Table 6.14: Results Case 1, with $a/h = 10$, under applied potential.

z/h	$u \times 10^{12}$		$w \times 10^{11}$	ϕ		σ_{xx}		$D_x \times 10^{8}$	
	Exact	UEL2	Exact	Exact	UEL2	Exact	UEL2	Exact	UEL2
1/2	-13.207	-13.197	-1.265	1.000	1.000	16.993	17.636	-60.885	-60.943
2/5	1.988	1.986	-1.227	0.999	0.999	-14.335	-14.196	-60.787	-60.891
2/5	1.988	1.986	-1.227	0.999	0.999	-8.525	-8.531	-0.097	-0.097
2/15	0.935	1.027	-1.238	0.658	0.658	-4.032	-4.424	-0.064	-0.064
2/15	0.935	1.027	-1.238	0.658	0.658	-0.451	-0.467	-0.055	-0.055
0	0.497	0.547	-1.241	0.491	0.491	-0.255	-0.260	-0.041	-0.041
-2/15	0.067	0.068	-1.242	0.326	0.326	-0.062	-0.053	-0.027	-0.027
-2/15	0.067	0.068	-1.242	0.326	0.326	-0.314	-0.316	-0.032	-0.032
-2/5	-0.877	-0.891	-1.240	0.000	0.000	3.718	3.791	0.000	0.000
-2/5	-0.877	-0.891	-1.240	0.000	0.000	0.348	0.519	-0.015	-0.012
-1/2	-1.262	-1.277	-1.234	0.000	0.000	2.221	2.386	0.000	-0.005
UEL2			-1.234						

Table 6.15: Transverse electric displacement and transverse shear stresses for Case 1, with $a/h = 10$, under applied load.

z/h	$D_z \times 10^{12}$		τ_{xz}			τ_{yz}		
	Exact	UEL2	Exact	UEL2 (C)	UEL2 (E)	Exact	UEL2 (C)	UEL2 (E)
1/2	12.650	11.462	0.000	0.570	0.000	0.000	0.581	0.000
2/5	-0.031	-0.939	1.256	0.733	0.891	1.279	0.745	0.913
2/5	-0.031	-0.092	1.256	2.480	0.891	1.279	1.240	0.913
2/15	0.029	-0.031	2.463	2.480	2.063	1.531	1.240	1.041
2/15	0.029	-0.031	2.463	1.581	2.063	1.531	1.945	1.041
-2/15	0.090	0.031	2.480	1.581	2.063	1.511	1.945	1.041
-2/15	0.090	0.031	2.480	2.480	2.063	1.511	1.240	1.041
-2/5	0.153	0.092	1.264	2.480	0.891	1.291	1.240	0.917
-2/5	0.153	0.939	1.264	0.657	0.891	1.291	0.745	0.917
-1/2	-12.337	-11.462	0.000	0.570	0.000	0.000	0.581	0.000

Table 6.16: Transverse electric displacement and transverse shear stresses for Case 1, with $a/h = 10$, under applied potential.

z/h	$D_z \times 10^{8}$		τ_{xz}			τ_{yz}		
	Exact	UEL2	Exact	UEL2 (C)	UEL2 (E)	Exact	UEL2 (C)	UEL2 (E)
1/2	-4.168	-4.174	0.000	0.664	0.000	0.000	0.648	0.000
2/5	-0.347	-0.347	0.362	0.151	0.373	0.327	0.135	0.354
2/5	-0.347	-0.343	0.362	-0.155	0.373	0.327	0.055	0.354
2/15	-0.334	-0.336	-0.207	-0.155	-0.169	0.209	0.055	0.279
2/15	-0.334	-0.336	-0.207	-0.099	-0.169	0.209	0.086	0.279
-2/15	-0.327	-0.328	-0.248	-0.099	-0.191	-0.101	0.086	-0.043
-2/15	-0.327	-0.328	-0.248	-0.155	-0.191	-0.101	0.055	-0.043
-2/5	-0.324	-0.321	-0.098	-0.155	-0.045	-0.085	0.055	-0.035
-2/5	-0.324	-0.325	-0.098	-0.025	-0.045	-0.085	-0.020	-0.035
-1/2	-0.324	-0.324	0.000	-0.092	0.000	0.000	-0.087	0.000

6.3.3 Thick Plates

For thick plates with $a/h = 4$, tables 6.17 and 6.19 show the UEL2 results for the applied load case, while tables 6.18 and 6.20 concern the applied potential case. The only values of reference are given at the interfaces between the composite core and the piezoelectric face layers, since for thick plates the plane stress and the FSDT assumptions are significantly far from the complex through-thickness variation shown by the exact solutions.

Hence, the discrepancy between the present model and the exact solutions, caused by the reduced side-to-thickness ratio, is visible in all variables, for both loading cases.

Table 6.17: Results Case 1, with $a/h = 4$, under applied load.

z/h	$u \times 10^{12}$		$w \times 10^{11}$	$\phi \times 10^{3}$		σ_{xx}		$D_x \times 10^{12}$	
	Exact	UEL2	Exact	Exact	UEL2	Exact	UEL2	Exact	UEL2
2/5	-0.253	-0.253	0.315	0.058	0.070	3.627	3.359	181.761	81.947
2/5	-0.253	-0.253	0.315	0.058	0.070	3.042	2.718	-0.140	51.211
-2/5	0.275	0.253	0.286	0.073	0.070	-2.924	-2.718	-0.177	-0.169
-2/5	0.275	0.253	0.286	0.073	0.070	-3.549	-3.359	156.167	51.211
UEL2			0.291						

Table 6.18: Results Case 1, with $a/h = 4$, under applied potential.

z/h	$u \times 10^{12}$		$w \times 10^{11}$	ϕ		σ_{xx}		$D_x \times 10^8$	
	Exact	UEL2	Exact	Exact	UEL2	Exact	UEL2	Exact	UEL2
2/5	5.070	4.731	-1.352	0.9930	0.9932	-79.342	-71.941	-150.852	-151.235
2/5	5.070	4.731	-1.352	0.9930	0.9932	-55.001	-51.024	-0.242	-0.242
-2/5	-1.209	-1.346	-1.388	-0.0001	-0.0002	12.768	14.482	0.000	0.000
-2/5	-1.209	-1.346	-1.388	-0.0001	-0.0002	10.559	15.402	-0.085	-0.046
UEL2			-1.359						

Table 6.19: Transverse electric displacement and transverse shear stresses for Case 1, with $a/h = 4$, under applied load.

z/h	$D_z \times 10^{12}$		τ_{xz}			τ_{yz}		
	Exact	UEL2	Exact	UEL2 (C)	UEL2 (E)	Exact	UEL2 (C)	UEL2 (E)
2/5	-0.033	-0.974	0.542	0.286	0.368	0.551	0.331	0.397
2/5	-0.033	-0.091	0.542	0.316	0.368	0.551	0.526	0.397
-2/5	0.140	0.091	0.537	0.316	0.368	0.562	0.526	0.399
-2/5	0.140	0.974	0.537	0.286	0.368	0.562	0.331	0.399

Table 6.20: Transverse electric displacement and transverse shear stresses for Case 1, with $a/h = 4$, under applied potential.

z/h	$D_z \times 10^8$		τ_{xz}			τ_{yz}		
	Exact	UEL2	Exact	UEL2 (C)	UEL2 (E)	Exact	UEL2 (C)	UEL2 (E)
2/5	-0.419	-0.412	5.796	3.367	6.358	4.465	2.848	5.418
2/5	-0.419	-0.395	5.796	-1.743	6.358	4.465	0.410	5.418
-2/5	-0.287	-0.265	-1.939	-1.743	-1.694	-1.855	0.410	-1.932
-2/5	-0.287	-0.288	-1.939	-1.437	-1.694	-1.855	-1.552	-1.932

6.4 Case 2 - Orthotropic Piezoelectric Layers

Static analysis results for simply-supported plates of Case 2, [PVDF/90° /0° /90° /PVDF] with PVDF layers at 0° , under applied bi-sinusoidal load or applied potential, from thin to thicker plates.

6.4.1 Thin Plates

For thin plates with $a/h = 100$, tables 6.21 and 6.23 show the results using UEL2 for applied load, as well as tables 6.22 and 6.24 for applied potential. In Appendix E, tables E.3 and E.4 show similar results when UEL1 model is used instead of UEL2, as already seen for the thin plates in Case 1.

From tables 6.21 and 6.22, one can see that for both loading conditions, the displacements and electric potential are in agreement with the exact solutions. However, due to the FSDT assumption of constant transverse shear strains, specially in the applied load case, the in-plane electric displacement within the piezoelectric layers does not match the exact solutions, since the in-plane electric displacements are dependent on the transverse shear strains from the constitutive equation (2.15).

For the applied potential case, the exact solution demonstrates that both piezoelectric layers exhibit significant variations of transverse displacements within the piezoelectric layers, which is due to a higher transverse normal compressibility of the piezoelectric polymer PVDF comparatively to the piezoceramic PZT-4 (see material properties in table 6.1), where the transverse normal strains are almost negligible.

Concerning the transverse electric displacement, one can see from table 6.23 that in the applied

Table 6.21: Results Case 2, with $a/h = 100$, under applied load.

z/h	$u \times 10^{12}$		$w \times 10^{11}$	$\phi \times 10^{3}$		σ_{xx}		$D_x \times 10^{12}$	
	Exact	UEL2	Exact	Exact	UEL2	Exact	UEL2	Exact	UEL2
1/2	-8364.63	-8366.15	53397.96	0.00	0.00	6339.58	6352.10	0.00	-22.29
2/5	-6689.30	-6690.70	53398.95	34.01	33.71	5069.88	5080.00	-54.73	-34.01
2/5	-6689.30	-6690.70	53398.95	34.01	33.71	282.14	282.24	-2.84	-2.81
-2/5	6690.55	6690.70	53398.92	33.79	33.71	-281.70	-282.24	-2.82	-2.81
-2/5	6690.55	6690.70	53398.92	33.79	33.71	-5070.60	-5080.00	-54.66	-34.01
-1/2	8365.88	8366.15	53397.92	0.00	0.00	-6340.31	-6352.10	0.00	-22.29
UEL2			53402.09						

Table 6.22: Results Case 2, with $a/h = 100$, under applied potential.

z/h	$u \times 10^{12}$		$w \times 10^{11}$	ϕ		σ_{xx}		$D_x \times 10^{8}$	
	Exact	UEL2	Exact	Exact	UEL2	Exact	UEL2	Exact	UEL2
1/2	-1.188	-1.182	0.092	1.000	1.000	-1.098	-1.097	-0.035	-0.035
2/5	-1.193	-1.188	0.019	0.972	0.972	-1.092	-1.091	-0.034	-0.034
2/5	-1.193	-1.188	0.019	0.972	0.972	0.055	0.055	-0.008	-0.008
-2/5	-1.188	-1.183	0.022	0.028	0.028	0.055	0.054	0.000	0.000
-2/5	-1.188	-1.183	0.022	0.028	0.028	-1.095	-1.093	-0.001	-0.001
-1/2	-1.189	-1.183	-0.050	0.000	0.000	-1.094	-1.093	0.000	0.000
UEL2			0.021						

load case, the present UEL2 model does not satisfy the exact solutions due to the insufficient linear z-expansion of the transverse electric field in UEL2 model. While in the applied potential case, tables 6.24 and E.4, show that both UEL models are capable to achieve accurate predictions of transverse electric displacements for thin plates.

Furthermore, the equilibrium derived transverse shear stresses in tables 6.23 and 6.24 are far more accurate than the constitutively derived ones. Also, when comparing the respective values associated to Case 1 (tables 6.5 and 6.6), one can see that in Case 2 the equilibrium derived stresses are closer to the exact solutions.

Table 6.23: Transverse electric displacement and transverse shear stresses for Case 2, with $a/h = 100$, under applied load.

z/h	$D_z \times 10^{12}$		τ_{xz}			τ_{yz}		
	Exact	UEL2	Exact	UEL2 (C)	UEL2 (E)	Exact	UEL2 (C)	UEL2 (E)
1/2	-0.915	-0.206	0.000	9.809	0.000	0.000	1.539	0.000
2/5	-0.785	-0.077	18.877	9.808	17.909	2.961	1.538	2.034
2/5	-0.785	-0.077	18.877	18.073	17.909	2.961	17.663	2.034
-2/5	-0.631	0.077	18.879	18.073	17.909	2.961	17.663	2.101
-2/5	-0.631	0.077	18.879	9.808	17.909	2.961	1.538	2.101
-1/2	-0.501	0.206	0.000	9.809	0.000	0.000	1.539	0.000

Table 6.24: Transverse electric displacement and transverse shear stresses for Case 2, with $a/h = 100$, under applied potential.

z/h	$D_z \times 10^8$		τ_{xz}			τ_{yz}		
	Exact	UEL2	Exact	UEL2 (C)	UEL2 (E)	Exact	UEL2 (C)	UEL2 (E)
1/2	-0.3140	-0.3145	0.000	-0.002	0.000	0.000	-0.004	0.000
2/5	-0.3138	-0.3142	-0.003	-0.001	-0.002	-0.007	-0.003	-0.006
2/5	-0.3138	-0.3142	-0.003	0.000	-0.002	-0.007	0.000	-0.006
-2/5	-0.3136	-0.3140	0.003	0.000	0.003	0.007	0.000	0.007
-2/5	-0.3136	-0.3140	0.003	0.001	0.003	0.007	0.003	0.007
-1/2	-0.3136	-0.3140	0.000	0.002	0.000	0.000	0.004	0.000

6.4.2 Moderately Thick Plates

For moderately thick plates with $a/h = 20$, tables 6.25, 6.27 and 6.29 show the results for both UEL models with applied load, while tables 6.26, 6.28 and 6.30 show the results for applied potential. Similarly to the thin plate results, both UEL models provide almost the same level of accuracy for the two loading conditions, regarding plates with $a/h = 20$. A further reduction in the analysis of moderately thick plates is made by considering plates with $a/h = 10$, where the UEL2 results are shown in tables 6.31 and 6.33 for applied load, and in tables 6.32 and 6.34 for applied potential.

Regarding the applied load case, the achieved results for both aspect ratios ($a/h = 20$ and 10) are in agreement with the exact solutions, although the electric potential for the upper part of the plate ($z > 0$) starts to differ from the exact solution in more then 10% for $a/h = 20$ (figure 6.14), increasing for 30% with $a/h = 10$. Hence, the transverse electric displacements do not agree with the exact solutions as already seen for thin plates. Also, the in-plane electric displacements are wrongly determined, specially for the piezoelectric layers, where the transverse normal strains and transverse shear effects become more important in moderately thick and thick plates, grossly taken into account on the FSDT assumptions used in the developed UEL models.

In the applied potential case, the results for both plate's aspect ratios are in good agreement with the exact solutions, evidencing a better approximation than in the applied load case, particularly for the electric variables. The major discrepancy between the present models and the exact solution is found on the transverse displacement in tables 6.26 and 6.32, as already mentioned for thin plates, since in the applied potential case, the piezoelectric layers made of PVDF undergo in considerable transverse normal strains, as can be seen in figure 6.13, which in the present FSDT models are assumed to be negligible. Moreover, when comparing the in-plane displacements and the in-plane normal stresses in the previous tables, one can see a lost on the accuracy of the UEL2 model when the plate's aspect ratio goes from $a/h = 20$, with relative errors near of 1%, to $a/h = 10$, with associated relative errors near of 5% .

Concerning the transverse shear stresses, tables 6.29 and 6.30 for $a/h = 20$, as well as tables 6.33 and 6.34 for $a/h = 10$, suggest that for both aspect ratios, the quadratic equilibrium derived stresses are more precise than the constitutively derived ones, namely for the applied load case.

Table 6.25: Results Case 2, with $a/h = 20$, under applied load.

z/h	$u \times 10^{12}$			$w \times 10^{11}$	$\phi \times 10^{3}$			σ_{xx}		
	Exact	UEL1	UEL2	Exact	Exact	UEL1	UEL2	Exact	UEL1	UEL2
1/2	-66.628	-66.580	-66.580	90.708	0.000	0.000	0.000	252.79	252.84	252.85
2/5	-52.819	-52.823	-52.823	90.740	1.578	1.354	1.354	200.44	200.62	200.61
2/5	-52.819	-52.823	-52.823	90.740	1.578	1.354	1.354	11.65	11.20	11.20
-2/5	53.066	52.823	52.823	90.710	1.365	1.354	1.354	-11.21	-11.20	-11.20
-2/5	53.066	52.823	52.823	90.710	1.365	1.354	1.354	-201.15	-200.62	-200.61
-1/2	66.868	66.580	66.580	90.670	0.000	0.000	0.000	-253.48	-252.84	-252.85
UEL1 & UEL2				90.392						

Table 6.26: Results Case 2, with $a/h = 20$, under applied potential.

z/h	$u \times 10^{12}$			$w \times 10^{11}$	ϕ			σ_{xx}		
	Exact	UEL1	UEL2	Exact	Exact	UEL1	UEL2	Exact	UEL1	UEL2
1/2	-0.235	-0.225	-0.226	0.093	1.000	1.000	1.000	-1.163	-1.177	-1.194
2/5	-0.260	-0.255	-0.256	0.019	0.972	0.972	0.972	-1.035	-1.062	-1.045
2/5	-0.260	-0.255	-0.256	0.019	0.972	0.972	0.972	0.059	0.058	0.058
-2/5	-0.234	-0.230	-0.230	0.022	0.027	0.027	0.027	0.054	0.053	0.053
-2/5	-0.234	-0.230	-0.230	0.022	0.027	0.027	0.027	-1.097	-1.106	-1.107
-1/2	-0.238	-0.229	-0.229	-0.050	0.000	0.000	0.000	-1.079	-1.109	-1.109
UEL1 & UEL2				0.021						

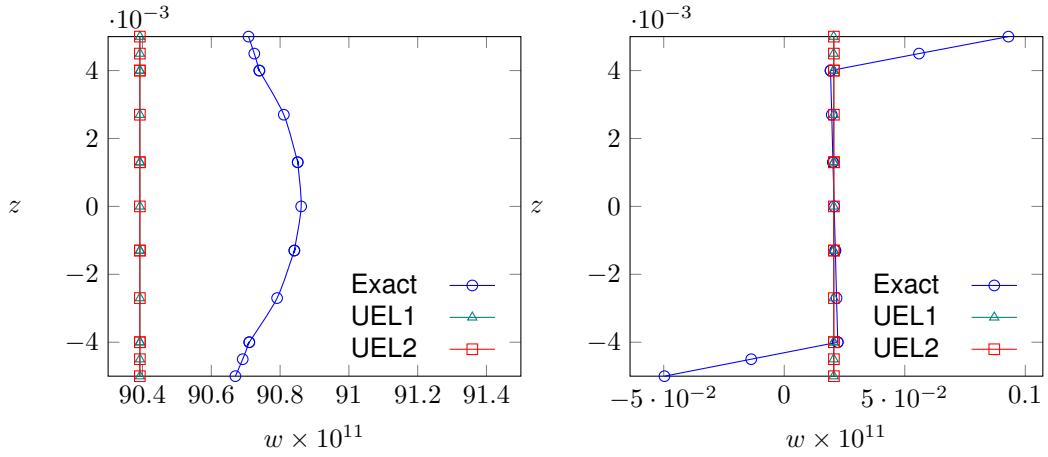

Figure 6.13: Transverse displacement w for Case 2, with $a/h = 20$, under applied load (on the left) and applied potential (on the right).

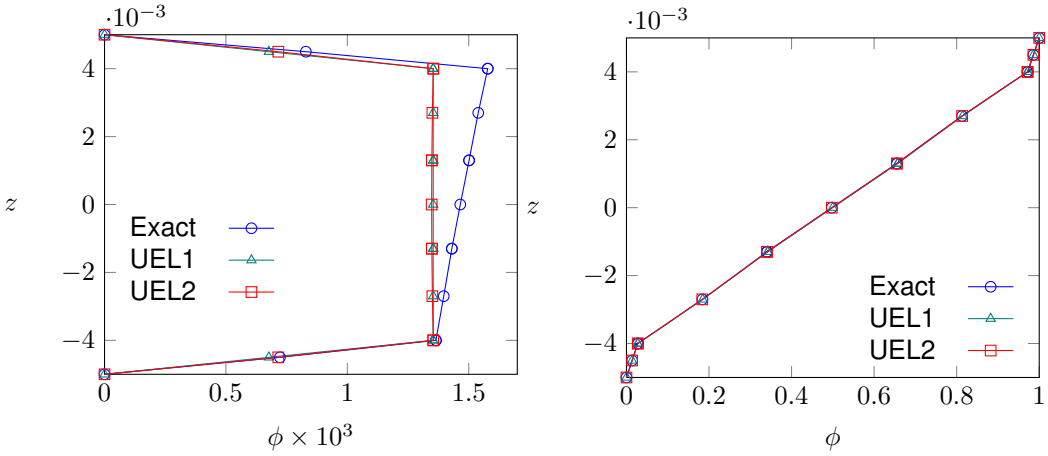

Figure 6.14: Electric potential ϕ for Case 2, with $a/h = 20$, under applied load (on the left) and applied potential (on the right).

Table 6.27: In-plane and transverse electric displacements for Case 2, with $a/h = 20$, under applied load.

z/h	$D_x \times 10^{12}$			$D_z \times 10^{12}$		
	Exact	UEL1	UEL2	Exact	UEL1	UEL2
1/2	0.000	-4.430	-4.430	-0.930	-17.830	-0.213
2/5	-11.261	-6.785	-6.785	-0.794	17.536	-0.082
2/5	-0.658	-0.565	-0.565	-0.794	0.000	-0.077
-2/5	-0.569	-0.565	-0.565	-0.627	0.000	0.077
-2/5	-10.917	-6.785	-6.785	-0.627	-17.536	0.082
-1/2	0.000	-4.430	-4.430	-0.497	17.830	0.213

Table 6.28: In-plane and transverse electric displacements for Case 2, with $a/h = 20$, under applied potential.

z/h	$D_x \times 10^{8}$			$D_z \times 10^{8}$		
	Exact	UEL1	UEL2	Exact	UEL1	UEL2
1/2	-0.174	-0.174	-0.174	-0.323	-0.320	-0.323
2/5	-0.169	-0.169	-0.169	-0.317	-0.320	-0.318
2/5	-0.041	-0.041	-0.041	-0.317	-0.314	-0.317
-2/5	-0.001	-0.001	-0.001	-0.312	-0.314	-0.311
-2/5	-0.005	-0.005	-0.005	-0.312	-0.312	-0.312
-1/2	0.000	0.000	0.000	-0.312	-0.312	-0.312

Table 6.29: Transverse shear stresses for Case 2, with $a/h = 20$, under applied load.

z/h	τ_{xz}				τ_{yz}			
	Exact	UEL1	UEL2 (C)	UEL2 (E)	Exact	UEL1	UEL2 (C)	UEL2 (E)
1/2	0.000	1.949	1.949	0.000	0.000	0.311	0.311	0.000
2/5	3.747	1.949	1.949	3.552	0.601	0.311	0.311	0.412
2/5	3.747	3.588	3.587	3.552	0.601	3.572	3.572	0.412
-2/5	3.759	3.588	3.587	3.552	0.600	3.572	3.572	0.426
-2/5	3.759	1.949	1.949	3.552	0.600	0.311	0.311	0.426
-1/2	0.000	1.949	1.949	0.000	0.000	0.311	0.311	0.000

Table 6.30: Transverse shear stresses for Case 2, with $a/h = 20$, under applied potential.

z/h	τ_{xz}				τ_{yz}			
	Exact	UEL1	UEL2 (C)	UEL2 (E)	Exact	UEL1	UEL2 (C)	UEL2 (E)
1/2	0.000	-0.011	-0.011	0.000	0.000	-0.021	-0.021	0.000
2/5	-0.016	-0.006	-0.006	-0.009	-0.037	-0.016	-0.016	-0.029
2/5	-0.016	0.000	0.000	-0.009	-0.037	0.000	0.000	-0.029
-2/5	0.016	0.000	0.000	0.017	0.035	0.000	0.000	0.036
-2/5	0.016	0.006	0.006	0.017	0.035	0.016	0.016	0.036
-1/2	0.000	0.010	0.010	0.000	0.000	0.020	0.020	0.000

Table 6.31: Results Case 2, with $a/h = 10$, under applied load.

z/h	$u \times 10^{12}$		$w \times 10^{11}$	$\phi \times 10^{3}$		σ_{xx}		$D_x \times 10^{12}$	
	Exact	UEL2	Exact	Exact	UEL2	Exact	UEL2	Exact	UEL2
1/2	-8.244	-8.219	6.716	0.000	0.000	62.792	62.492	0.000	-2.178
2/5	-6.352	-6.360	6.717	0.564	0.343	48.426	48.360	-6.135	-3.370
2/5	-6.352	-6.360	6.717	0.564	0.343	3.205	2.735	-0.471	-0.286
-2/5	6.471	6.360	6.688	0.351	0.343	-2.758	-2.735	-0.293	-0.286
-2/5	6.471	6.360	6.688	0.351	0.343	-49.109	-48.360	-5.440	-3.370
-1/2	8.351	8.219	6.677	0.000	0.000	-63.377	-62.492	0.000	-2.178
UEL2			6.610						

Table 6.32: Results Case 2, with $a/h = 10$, under applied potential.

z/h	$u \times 10^{12}$		$w \times 10^{11}$	ϕ		σ_{xx}		$D_x \times 10^{8}$	
	Exact	UEL2	Exact	Exact	UEL2	Exact	UEL2	Exact	UEL2
1/2	-0.115	-0.096	0.097	1.000	1.000	-1.360	-1.494	-0.348	-0.348
2/5	-0.163	-0.156	0.019	0.970	0.970	-0.855	-0.902	-0.337	-0.338
2/5	-0.163	-0.156	0.019	0.970	0.970	0.074	0.070	-0.081	-0.081
-2/5	-0.111	-0.104	0.022	0.027	0.027	0.052	0.048	-0.002	-0.002
-2/5	-0.111	-0.104	0.022	0.027	0.027	-1.104	-1.149	-0.009	-0.009
-1/2	-0.119	-0.103	-0.048	0.000	0.000	-1.036	-1.158	0.000	0.000
UEL2			0.021						

Table 6.33: Transverse electric displacement and transverse shear stresses for Case 2, with $a/h = 10$, under applied load.

z/h	$D_z \times 10^{12}$		τ_{xz}			τ_{yz}		
	Exact	UEL2	Exact	UEL2 (C)	UEL2 (E)	Exact	UEL2 (C)	UEL2 (E)
1/2	-0.974	-0.213	0.000	0.958	0.000	0.000	0.161	0.000
2/5	-0.820	-0.083	1.836	0.958	1.737	0.313	0.160	0.214
2/5	-0.820	-0.077	1.836	1.758	1.737	0.313	1.838	0.214
-2/5	-0.614	0.077	1.857	1.758	1.737	0.311	1.838	0.221
-2/5	-0.614	0.083	1.857	0.958	1.737	0.311	0.160	0.221
-1/2	-0.482	0.213	0.000	0.958	0.000	0.000	0.161	0.000

Table 6.34: Transverse electric displacement and transverse shear stresses for Case 2, with $a/h = 10$, under applied potential.

z/h	$D_z \times 10^{8}$		τ_{xz}			τ_{yz}		
	Exact	UEL2	Exact	UEL2 (C)	UEL2 (E)	Exact	UEL2 (C)	UEL2 (E)
1/2	-0.348	-0.348	0.000	-0.024	0.000	0.000	-0.045	0.000
2/5	-0.337	-0.338	-0.033	-0.015	-0.020	-0.078	-0.035	-0.064
2/5	-0.081	-0.081	-0.033	0.000	-0.020	-0.078	0.001	-0.064
-2/5	-0.002	-0.002	0.032	0.000	0.036	0.069	0.001	0.071
-2/5	-0.009	-0.009	0.032	0.013	0.036	0.069	0.031	0.071
-1/2	0.000	0.000	0.000	0.022	0.000	0.000	0.039	0.000

6.4.3 Thick Plates

For thick plates with $a/h = 4$, tables 6.35 and 6.37 show the UEL2 results for the applied load case, while tables 6.36 and 6.38 concern the applied potential case. The only values of reference are given at the interfaces between the composite core and the piezoelectric face layers, since for thick plates the FSDT kinematic assumptions are significantly far from the complex zig-zag through-thickness variation

shown by the exact solutions, as seen previously in Case 1.

The consequent discrepancy between the present model and the exact solutions is visible in almost all variables, for both loading cases. However, in the applied potential case, as shown in table 6.36, the quadratic z-expansion for the electric potential of UEL2 remains capable to almost match the exact solutions in the through-thickness distribution of the electric potential , as well as for the electric displacements.

Table 6.35: Results Case 2, with $a/h = 4$, under applied load.

z/h	$u \times 10^{12}$		$w \times 10^{11}$	$\phi \times 10^{3}$		σ_{xx}		$D_x \times 10^{12}$	
	Exact	UEL2	Exact	Exact	UEL2	Exact	UEL2	Exact	UEL2
2/5	-0.318	-0.338	0.372	0.278	0.058	6.299	6.462	-0.396	-1.337
2/5	-0.318	-0.338	0.372	0.278	0.058	0.855	0.388	-0.581	-0.121
-2/5	0.361	0.338	0.343	0.064	0.058	-0.400	-0.388	-0.133	-0.121
-2/5	0.361	0.338	0.343	0.064	0.058	-6.892	-6.462	-2.152	-1.337
UEL2			0.338						

Table 6.36: Results Case 2, with $a/h = 4$, under applied potential.

z/h	$u \times 10^{12}$		$w \times 10^{11}$	ϕ		σ_{xx}		$D_x \times 10^{8}$	
	Exact	UEL2	Exact	Exact	UEL2	Exact	UEL2	Exact	UEL2
2/5	-0.151	-0.135	0.021	0.959	0.959	0.324	0.035	-0.834	-0.835
2/5	-0.151	-0.135	0.021	0.959	0.959	0.172	0.144	-0.200	-0.200
-2/5	-0.028	-0.013	0.022	0.023	0.023	0.038	0.016	-0.005	-0.005
-2/5	-0.028	-0.013	0.022	0.023	0.023	-1.161	-1.452	-0.020	-0.020
UEL2			0.021						

Table 6.37: Transverse electric displacement and transverse shear stresses for Case 2, with $a/h = 4$, under applied load.

z/h	$D_z \times 10^{12}$		τ_{xz}			τ_{yz}		
	Exact	UEL2	Exact	UEL2 (C)	UEL2 (E)	Exact	UEL2 (C)	UEL2 (E)
2/5	-0.990	-0.083	0.676	0.367	0.642	0.159	0.074	0.099
2/5	-0.990	-0.076	0.676	0.654	0.642	0.159	0.804	0.099
-2/5	-0.536	0.076	0.703	0.654	0.642	0.148	0.804	0.102
-2/5	-0.536	0.083	0.703	0.367	0.642	0.148	0.074	0.102

Table 6.38: Transverse electric displacement and transverse shear stresses for Case 2, with $a/h = 4$, under applied potential.

z/h	$D_z \times 10^{8}$		τ_{xz}			τ_{yz}		
	Exact	UEL2	Exact	UEL2 (C)	UEL2 (E)	Exact	UEL2 (C)	UEL2 (E)
2/5	-0.398	-0.398	-0.087	-0.074	-0.084	-0.270	-0.137	-0.237
2/5	-0.398	-0.375	-0.087	0.004	-0.084	-0.270	0.009	-0.237
-2/5	-0.267	-0.247	0.077	0.004	0.115	0.149	0.009	0.159
-2/5	-0.267	-0.268	0.077	0.047	0.115	0.149	0.069	0.159

Chapter 7

Free Vibration Analysis Results

In this chapter, the free vibration analysis results are presented for the same piezoelectric multilayered composite plates, considered in Section 6.1 for static analysis. Particularly, the first twelve vibration frequencies ω_{mn} and associated modes (m, n) are determined, where m and n represent the number of half-waves in the x-direction and y-direction, respectively. The same simply-supported conditions and grounded plate edges in equations (6.3) and (6.4), respectively, are also used in free vibration analysis for comparison proposes with exact solutions.

Additionally, from Moleiro et al. [12], the grounded homogeneous potential conditions on both plate's surfaces, i.e.,

$$\phi(x, y, z = h/2) = \phi(x, y, z = -h/2) = 0 \tag{7.1}$$

provides lowest vibration frequencies when compared to other sets of possible electric boundary conditions. Following this, both top and bottom surfaces of the multilayered plate are assumed to be grounded, requiring that $\phi_1(x, y) = \phi_4(x, y) = 0$ for the developed UEL models.

For comparison proposes, the same unitary density is used for both piezoelectric and composite materials, i.e., $\rho = 1$ kg/m^3 instead of the real ones, presented in table 6.1. Hence, the results of both UEL1 and UEL2 models are compared to the ones obtained using a piezoelectric 3D element (C3D20RE) available in Abaqus, as well as to the exact solutions reported by Moleiro et al. [13] for the two thicker plates, with $a/h = 10$ and 4.

7.1 Convergence Study

For dynamic analysis, the convergence study of the UEL2 is carried out for the piezoelectric plate of Case 1, with $a/h = 20$, as shown in table 7.1, noting that a similar convergence is achieved when using UEL1 instead of UEL2. The first three vibration frequencies are followed from a mesh with 6×6 elements to the most refined mesh with 30×30 elements and compared to the Abaqus-3D solutions, with one element per layer, along with 30×30 in-plane elements, for which the convergence of the in-plane refinements is omitted for brevity. Furthermore, the relative discrepancy between the results in tables 6.2 to 7.11 (except tables 7.2 and 7.3) is obtained following: $\delta(\%) = (\omega_{\text{UEL}} - \omega_{\text{ref}}) \times 100/\omega_{\text{ref}}$, where the reference solution ω_{ref} is the exact solution, when available, otherwise Abaqus-3D solution is considered.

From table 7.1, one could see that the fundamental frequency is the less sensitive to the successive mesh refinements, while the higher order vibration frequencies (second and third modes) have slower convergence behaviours. Although the coarser mesh presents accurate results relative to the reference solution, one could expect an increase in the relative discrepancy for the remaining nine modes of interest. Hence, the most refined mesh is the chosen one due to a good compromise between the computational effort and accuracy of the results.

Table 7.1: Convergence of the first three vibration frequencies (rad/s) for UEL2, in Case 1, with $a/h = 20$.

Mesh	ω_{11}	δ_{11} (%)	ω_{12}	δ_{12} (%)	ω_{21}	δ_{21} (%)
6x6	374912	0.29	828258	0.32	998175	1.48
10x10	374878	0.28	827172	0.19	996710	1.34
20x20	374876	0.28	827105	0.18	996623	1.33
30x30	374874	0.28	827010	0.17	996489	1.31
Abaqus-3D	373829		825588		983573	

Regarding the analysis of the thicker plates with $a/h = 4$, using Abaqus-3D elements, the 30×30 mesh with one element per layer, M(5), show a considerable error relative to the exact solutions for the higher order modes, as can be seen in table 7.2. Consequently, for this aspect ratio a refined mesh with the same in-plane refinement, but with two elements per layer across the transverse direction, M(10), is used in order to better predict the complex behaviour of thicker plates. The results in table 7.2 show very precise solutions when using M(10) instead of M(5), hence two elements per layer are considered in the analysis of thicker plates with the brick elements.

Table 7.2: Convergence of the first thirteen vibration frequencies (rad/s), for thickness refinements of an in-plane mesh of 30×30 Abaqus-3D elements C3D20RE, in Case 1, with $a/h = 4$.

(m,n)	Exact	M(5)	$\delta(\%)$	M(10)	$\delta(\%)$
(1,1)-1	5707395	5513810	-3	5707450	0
(1,0)	8032970	8031020	0	8033060	0
(0,1)	8055542	8053690	0	8055640	0
(1,2)	10142101	9844950	-3	10142400	0
(2,1)	10524397	10240600	-3	10524800	0
(2,2)	13660384	10457200	-23	13660800	0
(1,3)	15219227	10547900	-31	15219900	0
(2,0)	15676601	10627300	-32	15676800	0
(0,2)	15841211	10683700	-33	15841400	0
(3,1)	15957590	10779200	-32	15958500	0
(2,3)	17869324	10907600	-39	17869900	0
(3,2)	18305531	10931600	-40	18306300	0
(1,1)-2	19130095	11123150	-42	19125700	0

In table 7.2, the thirteenth vibration mode, (1,1)-2, is added since it represents the second time that the fundamental mode (1,1)-1 appears for the multilayered plate of Case 1 with $a/h = 4$. In fact, the (1,1)-2 mode is a thickness mode, where transverse normal strains ε_{zz} are no more negligible, opposing to the fundamental mode where the plate's thickness remains almost constant while the plate its vibrating, as reported in Moleiro [13].

In table 7.3, a comparison between the UEL models with 30×30 elements and the Abaqus-3D

meshes is presented, regarding the number of DOFs and nodes used in each finite element model.

Table 7.3: Models comparison for plane meshes with 30x30 elements .

Model	# DOFs/node	# Nodes	# DOFs
UEL1	13	2821	36673
UEL2	16	2821	45136
Abaqus-3D M(5)	4	21731	86924
Abaqus-3D M(10)	4	40641	162564

7.2 Thin Plates

For thin plates with $a/h = 100$, the vibration frequencies and associated modes for both Case 1 and Case 2 are shown in the tables 7.4 and 7.5, respectively. For both stacking schemes, all first twelve modes are the typical flexural or bending modes, being the results in excellent agreement with the reference solution (Abaqus-3D).

Table 7.4: Vibration frequencies ω_{mn} (rad/s) for Case 1, with $a/h = 100$.

(m,n)	Abaqus-3D	UEL1	UEL2	δ_1 (%)	δ_2 (%)
(1,1)	15528	15522	15525	-0.04	-0.02
(1,2)	35490	35473	35481	-0.05	-0.03
(2,1)	44168	44183	44189	0.03	0.05
(2,2)	61807	61811	61823	0.01	0.03
(1,3)	69831	69795	69811	-0.05	-0.03
(3,1)	92138	92257	92270	0.13	0.14
(2,3)	93991	93979	94000	-0.01	0.01
(3,2)	108365	108477	108494	0.10	0.12
(1,4)	117883	117824	117852	-0.05	-0.03
(3,3)	137954	138052	138078	0.07	0.09
(2,4)	140600	140571	140603	-0.02	0.00
(4,1)	158412	158823	158843	0.26	0.27

Table 7.5: Vibration frequencies ω_{mn} (rad/s) for Case 2, with $a/h = 100$.

(m,n)	Abaqus-3D	UEL1	UEL2	δ (%)
(1,1)	13681	13683	13683	0.02
(1,2)	34509	34535	34535	0.08
(2,1)	41837	41846	41846	0.02
(2,2)	54496	54521	54521	0.05
(1,3)	72764	72903	72903	0.19
(2,3)	86179	86308	86308	0.15
(3,1)	90696	90735	90735	0.04
(3,2)	98974	99027	99027	0.05
(3,3)	121768	121899	121899	0.11
(1,4)	126462	126893	126893	0.34
(2,4)	136408	136825	136825	0.31
(4,1)	158453	158579	158579	0.08

Furthermore, in Case 1 both UEL models conduct to very similar vibration frequencies, while in Case 2 the models are coincident, due to a weaker electromechanical coupling in Case 2 comparatively to Case 1, i.e., lower piezoelectric coefficients (see the material properties in table 6.1), and consequent

insensitivity to the linear or quadratic z-expansions of the electric potential.

7.3 Moderately Thick Plates

For moderately thick plates with $a/h = 20$ and 10, the vibration frequencies and associated modes, for both Case 1 and Case 2, are shown in tables 7.6 and 7.7 for $a/h = 20$, respectively, likewise in tables 7.8 and 7.9 for $a/h = 10$. From these tables, one could see that in the first twelve vibration frequencies, some special modes, with null transverse displacement, known as membrane modes, in the form of $(m, 0)$ and $(0, n)$ emerge among the flexural modes, for moderately thick plates. These special modes only exhibit harmonic motion on the in-plane displacements, opposing to the flexural modes.

Similarly to the thin plates results, for the moderately thick plates with $a/h = 20$, the UEL models show very close values for the vibration frequencies of Case 1, while for Case 2 both UEL results are coincident. For both piezoelectric multilayered plates with $a/h = 20$, the achieved frequencies are in good agreement with the reference solutions, obtained using Abaqus-3D elements.

Table 7.6: Vibration frequencies ω_{mn} (rad/s) for Case 1, with $a/h = 20$.

(m, n)	Abaqus-3D	UEL1	UEL2	δ_1 (%)	δ_2 (%)
(1,1)	373829	374798	374874	0.26	0.28
(1,2)	825588	826792	827010	0.15	0.17
(2,1)	983573	996306	996489	1.29	1.31
(2,2)	1352630	1364710	1365050	0.89	0.92
(1,3)	1532650	1534950	1535420	0.15	0.18
(1,0)	1619960	1620510	1620510	0.03	0.03
(0,1)	1620150	1620510	1620510	0.02	0.02
(3,1)	1845390	1890250	1890640	2.43	2.45
(2,3)	1974270	1986520	1987150	0.62	0.65
(3,2)	2151350	2193270	2193840	1.95	1.98
(1,4)	2409900	2414460	2415350	0.19	0.23
(3,3)	2675670	2714400	2715290	1.45	1.48

Table 7.7: Vibration frequencies ω_{mn} (rad/s) for Case 2, with $a/h = 20$.

(m, n)	Abaqus-3D	UEL1	UEL2	δ (%)
(1,1)	331036	332008	332008	0.29
(1,2)	790713	803598	803598	1.63
(2,1)	935453	939386	939386	0.42
(0,1)	1197230	1197240	1197240	0.00
(1,0)	1197230	1223360	1223360	2.18
(2,2)	1211270	1223360	1223360	1.00
(1,3)	1523590	1573740	1573740	3.29
(3,1)	1804450	1830290	1830290	1.43
(2,3)	1817020	1850440	1850440	1.84
(3,2)	1993880	2012000	2012000	0.91
(0,2)	2394460	2394480	2394480	0.00
(2,0)	2394460	2394480	2394480	0.00

For plates with $a/h = 10$, the exact solutions reported by Moleiro et al. [13] are also presented and used as reference solution in the relative error computation. The results from the exact solutions and the Abaqus-3D elements are in good agreement, as expected from the quadratic twenty node element. Moreover, even being $a/h = 10$ the limit of applicability of the FSDT assumptions, the vibration results obtained with both UEL models, shown in tables 7.8 and 7.9, reveal a good resemblance to the exact ones. Again, in Case 1 both UEL models show similar results between them, being coincident in Case 2, as seen previously for plates with $a/h = 20$ and 100.

Table 7.8: Vibration frequencies ω_{mn} (rad/s) for Case 1, with $a/h = 10$.

(m, n)	Exact	Abaqus-3D	UEL1	UEL2	δ_1 (%)	δ_2 (%)
(1,1)	1352637	1352630	1364713	1365092	0.89	0.92
(1,2)	2782211	2782530	2796307	2797477	0.51	0.55
(2,1)	3094893	3095080	3183149	3184097	2.85	2.88
(1,0)	3236504	3236540	3241018	3241018	0.14	0.14
(0,1)	3237982	3238020	3241018	3241018	0.09	0.09
(2,2)	4157822	4158160	4232076	4233974	1.79	1.83
(1,3)	4710385	4711530	4732349	4734878	0.47	0.52
(3,1)	5160833	5161900	5354052	5356266	3.74	3.79
(2,3)	5761513	5762440	5829659	5833137	1.18	1.24
(3,2)	5984538	5985510	6149998	6153476	2.76	2.82
(2,0)	6446207	6446290	6481088	6481088	0.54	0.54
(0,2)	6457880	6457960	6481088	6481088	0.36	0.36

Table 7.9: Vibration frequencies ω_{mn} (rad/s) for Case 2, with $a/h = 10$.

(m, n)	Exact	Abaqus-3D	UEL1	UEL2	δ (%)
(1,1)	1211320	1211270	1223359	1223359	0.99
(0,1)	2394406	2394460	2394477	2394477	0.00
(1,0)	2394407	2394460	2394477	2394477	0.00
(1,2)	2600998	2601150	2709756	2709756	4.18
(2,1)	2951466	2951630	2983103	2983103	1.07
(0,2)	3789856	3790120	3887388	3887388	2.57
(2,0)	4447030	4448480	4731084	4731084	6.39
(2,2)	4788771	4788880	4788953	4788953	0.00
(1,3)	4788776	4788880	4788953	4788953	0.00
(3,1)	5029363	5029970	5099489	5099489	1.39
(2,3)	5260431	5261760	5516910	5516910	4.88
(3,2)	5583238	5583870	5695895	5695895	2.02

From the results for thin plates in tables 7.4 and 7.5, to moderately thick plates in tables 7.6 to 7.9, one can see an increase in the relative discrepancy between the predicted vibration frequencies of the UEL models and the associated reference solutions. However it remains very low ($\sim 1\%$), specially for the first flexural modes and for the special membrane modes. Furthermore, in Case 2 the discrepancy between results increases for the higher-order flexural modes, such as the $(1, 2)$ and $(2, 3)$, as well as for the second pair of special modes $(0, 2)$ and $(2, 0)$.

7.4 Thick Plates

For the thicker plates with $a/h = 4$, the vibration frequencies and associated modes for both plates of Case 1 and Case 2 are shown in the tables 7.10 and 7.11, respectively. From the comparison of the results predicted by the UEL models and the exact solutions reported by Moleiro et al. [13], one can conclude that both UEL models predict the first twelve vibration modes and associated frequencies for thick plates, with relatively good accuracy to the exact ones. When comparing the Abaqus-3D results to the exact solutions, in table 7.2, one can notice an excellent resemblance between the results, at cost of higher computational effort, as shown in table 7.3, by considering two brick elements per layer.

Table 7.10: Vibration frequencies ω_{mn} (rad/s) for Case 1, with $a/h = 4$.

(m,n)	Exact	Abaqus-3D	UEL1	UEL2	δ_1 (%)	δ_2 (%)
(1,1)	5707395	5707450	5817642	5820804	1.93	1.99
(1,0)	8032970	8033060	8100807	8100807	0.84	0.84
(0,1)	8055542	8055640	8100807	8100807	0.56	0.56
(1,2)	10142101	10142400	10245147	10256848	1.02	1.13
(2,1)	10524397	10524800	10791589	10802973	2.54	2.65
(2,2)	13660384	13660800	13877023	13899159	1.59	1.75
(1,3)	15219227	15219900	15358866	15390173	0.92	1.12
(2,0)	15676601	15676800	16190862	16190862	3.28	3.28
(0,2)	15841211	15841400	16190862	16190862	2.21	2.21
(3,1)	15957590	15958500	16206989	16236715	1.56	1.75
(2,3)	17869324	17869900	18085698	18130287	1.21	1.46
(3,2)	18305531	18306300	18539485	18582808	1.28	1.51

Table 7.11: Vibration frequencies ω_{mn} (rad/s) for Case 2, with $a/h = 4$.

(m,n)	Exact	Abaqus-3D	UEL1	UEL2	δ (%)
(1,1)	5224114	5223940	5389470	5389470	3.17
(0,1)	5985925	5986050	5986192	5986192	0.00
(1,0)	5985936	5986060	5986192	5986192	0.00
(1,2)	9308119	9308340	9883699	9883699	6.18
(2,1)	9862718	9862790	10072803	10072803	2.13
(0,2)	11971204	11971500	11972067	11972067	0.01
(2,0)	11971291	11971600	11972067	11972067	0.01
(2,2)	12524293	12524600	13047874	13047874	4.18
(1,3)	14113537	14115100	14938916	14938916	5.85
(3,1)	14835346	14835800	15120431	15120431	1.92
(2,3)	16414198	16415600	17199312	17199312	4.78
(3,2)	16720868	16721400	17243900	17243900	3.13

Again, in Case 1 similar vibration frequencies are achieved using both UEL models, being coincident for the membrane modes, while in Case 2, both UEL results are coincident. Hence, the linear z-expansion takes advantage over the quadratic one by achieving the same level of accuracy with less computational effort, as can be seen by the total number of DOFs in table 7.3.

Furthermore, the increase in relative error of the vibration frequencies, from the moderately thick plates to the thicker ones, is less visible in the flexural modes of Case 1 than in the respective ones of Case 2, particularly the $(1,2)$ and the $(1,3)$. The opposite occurs in the special membrane modes, which

are perfectly estimated for Case 2, while in Case 1 the second pair of special modes, i.e., the $(2,0)$ and $(0,2)$, exhibit a slightly discrepancy to the exact solutions.

Some representative vibration modes are represented for the plate's mid-plane ($z=0$), in figures 7.1 to 7.11, for the plate of Case 1, with $a/h=4$, where the special modes, which only exhibit the harmonic motion on the in-plane displacements, contrast with the flexural modes, where the harmonic vibration occurs on the transverse direction.

As presented in Section 7.1, a curious result is found for Case 1, with $a/h=4$, where the thirteenth mode is a thickness mode. Besides the fact that these types of modes show a considerable variation of the plate's thickness as reported in Moleiro et al. [13], which is out of the scope of the FSDT assumptions used in the developed models, the predicted vibration frequencies for the first thickness mode $(1,1)-2$ are 19595040 rad/s for UEL1 and 19595054 rad/s for UEL2. The achieved values have a relative error to the exact solution shown in table 7.2, of near 2%, which is a very good approximation, even when assuming a constant transverse displacement across the transverse direction. However, the associated vibration mode is only representative for the plate's mid-plane, since it does not correspond to the overall physical vibration mechanism demonstrated by the exact solutions and by the piezoelectric 3D element, when two elements per layer are used.

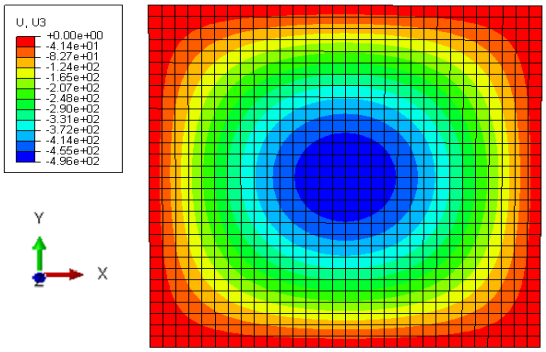

Figure 7.1: Fundamental mode, (1,1), of Case 1, with $a/h=4$.

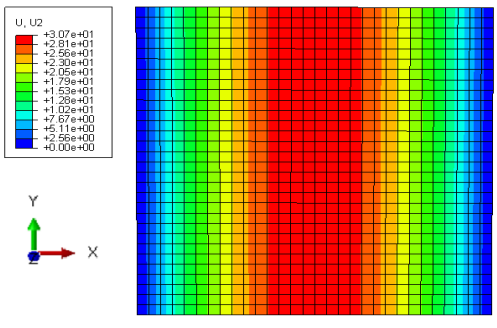

Figure 7.2: Mode (1,0) of Case 1, with $a/h=4$.

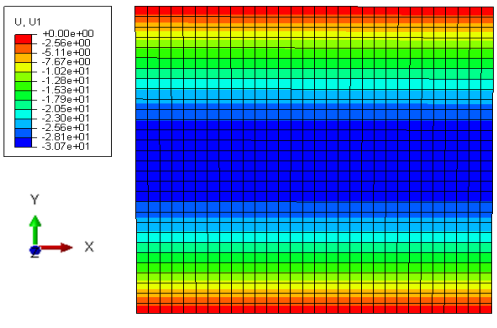

Figure 7.3: Mode (0,1) of Case 1, with $a/h=4$.

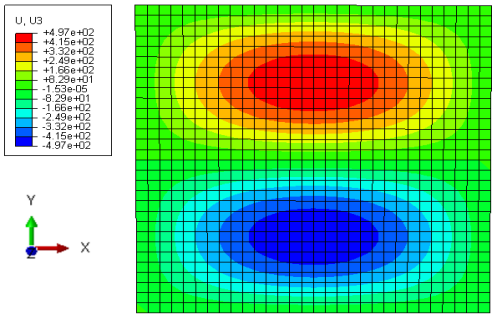

Figure 7.4: Mode (1,2) of Case 1, with $a/h = 4$.

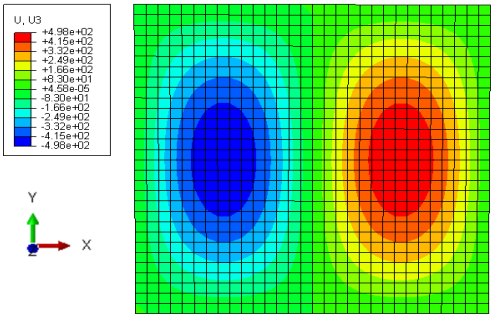

Figure 7.5: Mode (2,1) of Case 1, with $a/h = 4$.

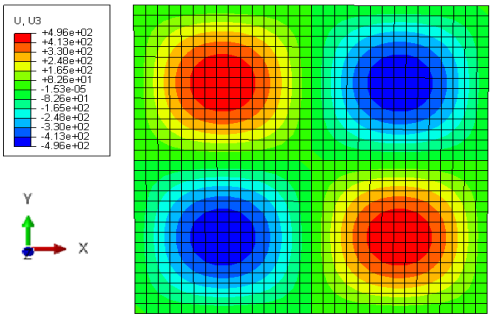

Figure 7.6: Mode (2,2) of Case 1, with $a/h = 4$.

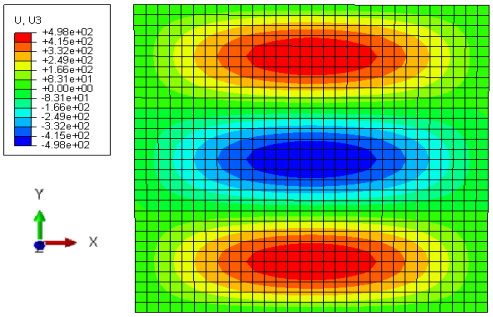

Figure 7.7: Mode (1,3) of Case 1, with $a/h = 4$.

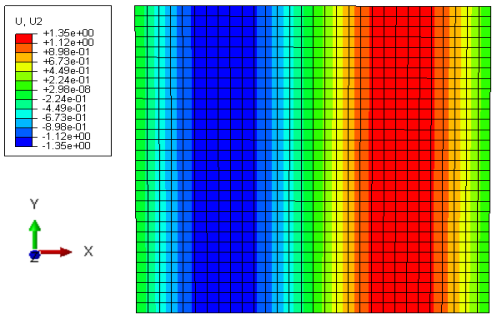

Figure 7.8: Mode (2,0) of Case 1, with $a/h = 4$.

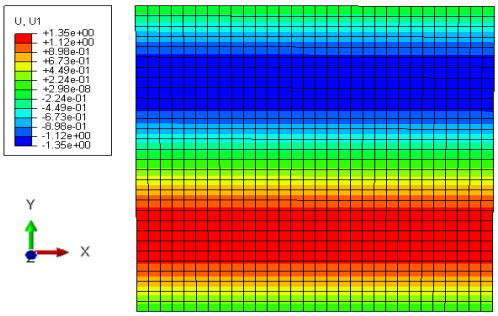

Figure 7.9: Mode (0,2) of Case 1, with $a/h = 4$.

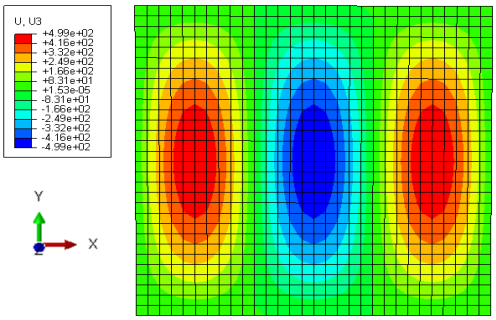

Figure 7.10: Mode (3,1) of Case 1, with $a/h = 4$.

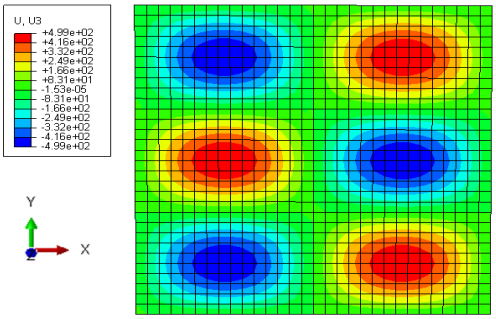

Figure 7.11: Mode (2,3) of Case 1, with $a/h = 4$.

Chapter 8

Conclusions

The present thesis reveals an useful and efficient new approach for static and free vibration analysis of piezoelectric multilayered composite plates, through the implementation of the discrete LW electro-elastic plate finite elements developed in Chapters 3 and 4, using Abaqus UEL subroutine presented in Chapter 5, taking advantage of the software's tools, such as the mesh generation, the specification of loads and boundary conditions, as well as the robust solvers. The developed UEL models assume a LW description for three-discrete layers, allowing both mechanical displacements and electric potential to *a priori* fulfill the C_z^0-requirements for the primary variables, according to Heyliger's exact solutions [10]. Moreover, the middle discrete layer consists in an ESL model of a multilayered composite plate, being the remaining two discrete layers the top and bottom piezoelectric face layers.

In each discrete layer, the FSDT displacement field is modified to account for the interlaminar continuity conditions and combined with two different z-expansions of the electric potential, namely a simple linear approximation in UEL1 and a quadratic variation in UEL2. For both eight node UEL models, the elementary mass and stiffness matrices were derived from the Hamilton's principle and numerically computed using Gauss-Legendre integration, with reduced integration in the shear terms, in which an unitary shear correction factor is used for all discrete layers as first approach.

The validation of the present models, in statics and dynamics, is made with benchmark numerical applications used for evaluation of exact solutions available on the literature, namely the reported test cases by Moleiro et al. [13]. Specifically, two symmetric stacking sequences with different piezoelectric materials and a multilayered graphite-epoxy core are investigated: [PZT-4/0°/90°/0°/PZT-4] in Case 1 and [PVDF/90°/0°/90°/PVDF] in Case 2, from thin to thicker square plates, with associated aspect ratios of $a/h = 100,\ 20,\ 20$ and 4.

8.1 Concluding Remarks and Achievements

In static analysis, the results of the developed models are compared with the associated exact solutions available for the case of simply-supported plates with applied bi-sinusoidal load (monitoring mode) and for the case of an applied bi-sinusoidal potential (actuation mode), through the implementation of other two subroutines available in Abaqus for specifying loads and boundary conditions. Furthermore, the assessment of the transverse shear stresses is improved in UEL2 using direct integration of the fundamental equilibrium equations.

The predictive capabilities of the developed UEL models in static response, for thin and moderately thick piezoelectric composite plates, under applied load or potential, is demonstrated by the resemblance between the UEL static analysis results and the exact ones, in terms of displacements, electric potential and in-plane stresses shown in Chapter 6. However, due to the assumption of a constant transverse shear strain state in each discrete layer, some shortcomings are detected, particularly in the applied load case. In fact, for the applied load case, the FSDT assumptions lead to an inaccurate description of the in-plane electric displacements within the piezoelectric layers, since these variables are dependent on the shear strains, which are assumed to be constant in each discrete layer. Also, even the quadratic z-expansion for the electric potential appears to be slightly inappropriate for a sufficiently accurate evaluation of the transverse electric displacements for the piezoelectric layers of moderately thick plates, under applied load.

The aforementioned discrepancies become more pronounced for moderately thick plates with $a/h = 20$ or 10 of Case 2, where the transversely softer piezoelectric polymer PVDF undergoes in larger normal compressibility effects, where the transverse normal strains and transverse shear strains play an important role. Therefore, in the applied load case, a poorest performance of both UEL models is achieved in the assessment of the in-plane displacements, in-plane stresses as well as in the electric potential distribution and consequently on the electric displacements, comparatively to Case 1 that concerns the piezoceramic PZT-4. Likewise, for the applied potential case, this transversely softer behaviour of PVDF produces considerable through-thickness variations of the transverse displacement, that can not be taken into account in the present FSDT based models, with negligible transverse normal strains.

On the other hand, the static response to an applied potential of plates with the piezoceramic PZT-4 in Case 1, almost match the exact solutions for thin and moderately thick plates, including in-plane stresses and electric displacements. In this case, the hypothesis of constant transverse displacement is far more accurate than for the PVDF case, being the transverse displacements of the UEL2 model the most precise comparatively to UEL1. This result suggest that the present electro-elastic elements are more suitable to be used in the analysis of sensors or actuators made of harder piezoelectric materials.

Regarding the evaluation of the transverse shear stresses, it is concluded that the direct integration of the equilibrium equations provides a better description for these stresses than the constitutive approach, fulfilling the interlaminar continuity conditions and the stress free conditions for both top and bottom surfaces of the plate. Although both methods fail on an accurate determination of the transverse shear stresses with respect to the exact solutions, both constitutively and equilibrium derived stresses give

an idea of the stress state in each layer, where the second ones offer an exact distribution expect for a correction factor, dependent on the loading, dimensions and material properties.

Comparing the accuracy of the equilibrium derived stresses in Case 1 to Case 2, it is demonstrated that for Case 2 the predicted results are the closest to the exact solutions, particularly for the applied potential condition. However, for the stacking scheme of Case 1, slightly more precise results are obtained in the applied load case rather than in the applied potential. Ultimately, the discrepancy found in the equilibrium derived stresses relatively to the exact solutions is more dependent on the material and on the loading and boundary conditions, than on the plate's aspect ratio.

For free vibration analysis, the available exact solutions are also restricted to simply-supported plates, being the electric boundary conditions of most interest the grounded homogeneous electric potential boundary conditions for both plate surfaces. In this case, the first twelve vibration modes and frequencies, obtained using the UEL models, are additionally compared to one piezoelectric brick element available in Abaqus, for the same stacking sequences and aspect ratios used in static analysis. Noting that the associated exact solutions are only presented for the thicker plates with $a/h = 10$ and 4, reported by Moleiro et al. [13].

The free vibration analysis results, for both stacking sequences, presented in Chapter 7, demonstrate a good behaviour of both UEL models in the evaluation of at least the first twelve vibration frequencies in agreement with the reference solutions, including special membrane modes, from thin to thicker plates. Although for thick plates with $a/h = 4$, the results match with relatively good accuracy the first twelve vibration frequencies, the use of the developed models for the determination of higher-order modes is limited to the earliest appearance of thickness modes in thick plates, comparatively to moderately thick and thin plates. Due to their inherent complex behaviour, thickness modes are out of the scope of validity of the present models due to the assumption of negligible transverse normal strains in the developed first-order models.

Ultimately, the main achievements of the present thesis is the development, implementation and validation, with exact solutions, of two LW electro-elastic UEL models in Abaqus, completing the lack of piezoelectric plate elements in the software's library. In fact, the present work and achieved results represent a complement to the literature, particularly by implementing an Abaqus UEL subroutine to access a comprehensive comparison of the performance of two LW electro-elastic plate elements relatively to the exact solutions, in both static and free vibration analysis, for two different piezoelectric materials and four side-to-thickness ratios.

To sum up, the conformity between the UEL results and the exact solutions in the test cases, suggests the capability of the developed elements to perform static analysis, in monitoring modes and specially in actuation modes, of thin and moderately thick piezoelectric multilayered composite plates, as well as to perform free vibration analysis to access the vibration modes and associated frequencies. However, some inherent limitations of the FSDT displacement field must be kept in mind, with an overall advantage in static analysis of the quadratic z-expansion for the electric potential. The developed models represent a breakthrough for preliminary modelling and analysis of piezoelectric smart structures, since the developed finite element models can be easily implement for other flat geometries, with different boundary

conditions and also with less computational effort than Abaqus-3D elements. Furthermore, due to the highlighted level of accuracy in free vibration analysis, both finite element models are suitable to be used in optimization processes, as well as in active vibration control using damping treatments with feed-back control laws.

8.2 Future Work

The present work opens several possibilities for future work, regarding not only improvements of the present LW models, but also the application of similar discrete LW descriptions, using Abaqus UEL subroutine or other computational tools, to investigate different phenomena occurring in multilayered composite plates.

Some suggestions can be made to improve the performance of the present models, specially for thick plates, where a refined-FSDT or the HSDT can be used rather than the simple FSDT. Further improvements can be made by considering a generalized formulation with an arbitrary number of layers, as well as by including transverse normal strains by means of Reissner's Variational Theorem. Similarly, for the description of the electric potential, one could think on using a cubic z-expansion or a refined quadratic one with trigonometric terms, in order to better evaluate the evolution of the electric displacements, particularly for the case of an applied load in static analysis.

Furthermore, the present models can be applied for optimization purposes, namely in active damping treatments of plates, where the optimal location and geometry of the piezoelectric sensors and actuators can be estimated. In this sense, the inclusion of frequency-dependent materials in the models, such as the presence of viscoeleastic layers, is also an interesting improvement, allowing the analysis of active-passive multilayered composite plates.

Regarding the application of similar formulations for analysis of other multiphysic phenomena associated with multilayered composite plates, one could think on use the same type of discrete LW approach to access thermo-elastic effects or even hygro-thermo-elastic effects by adding the moister absorption mechanisms. Also, plates with functionally graded materials can also be considered as a possible issue of study using LW plate elements.

Bibliography

[1] Marsh G. Composites in commercial jets. *Reinforced Plastics*, 59(4):190–193, 2015.

[2] Heyliger P.R. Static behavior of laminated elastic/piezoelectric plates. *American Institute of Aeronautics and Astronautics Journal*, 32(12):2481–2484, 1994.

[3] Lee H. and Saravanos D.A. Generalized finite element formulation for smart multilayered thermal piezoelectric composite plates. *Pergamon Press*, 34(26):3355–3371, 1997.

[4] Moleiro F., Mota Soares C.M., and Carrera E. Three-dimensional exact hygro-thermo-elastic solutions for multilayered plates, composite laminates, fibre metal laminates and sandwich plates. *Composite Structures*, 216:260–278, 2019.

[5] Campos L.M.B.C., Moleiro F., and Silva M.J.S. On the fundamental equations of unsteady anisothermal viscoelastic piezoelectromagnetism. *European Journal of Mechanics / A Solids*, 78: 103848, 2019.

[6] Curie P. and Curie J. Développement, par pression, de l'électricité polaire dans lex cristaux hémièdres à faces inclinées. *Compte Rendus (France)*, 91:294–295, 1880.

[7] Lippmann J. Principe de la conservation de l'électricité. *Ann de Chemie e de Physique*, 5:24–145, 1881.

[8] Pagano N.J. Exact solutions for rectangular bidirectional composites and sandwich plates. *Journal of Composite Materials*, 4:20–34, 1970.

[9] Heyliger P.R. Exact free-vibration analysis of laminated plates with embedded piezoelectric layers. *The Journal of the Acoustical Society of America*, 98(3):1547–1557, 1995.

[10] Heyliger P.R. Exact solutions for simply supported laminated piezoelectric plates. *Journal of Applied Mechanics*, 64:299–306, 1997.

[11] Moleiro F., Mota Soares C.M., Mota Soares C.A., and Reddy J.N. Benchmark exact solutions for the static analysis of multilayered piezoelectric composite plates using pvdf. *Composite Structures*, 107:389–395, 2014.

[12] Moleiro F., Araújo A.L., and Reddy J.N. Benchmark exact free vibration solutions for multilayered piezoelectric composite plates. *Composite Structures*, 182:598–605, 2017.

[13] Moleiro F., Mota Soares C.M., Carrera E., and Reddy J.N. Evaluation of exact electro-elastic static and free vibration solutions of multilayered plates for benchmarking: piezoelectric composite laminates and soft core sandwich plates. *Composites Part C: Open Access*, 2, 2020. doi:https://doi.org/10.1016/j.jcomc.2020.100038.

[14] Vel S.S. and Batra R.C. Exact solution for rectangular sandwich plates with embedded piezoelectric shear actuators. *American Institute of Aeronautics and Astronautics Journal*, 39(7):1363–1373, 2001.

[15] Baillargeon B.P. and Vel S.S. Exact solution for the vibration and active damping of composite plates with piezoelectric shear actuators. *Journal of Sound and Vibration*, 282:781–804, 2005.

[16] Carrera E. Theories and finite elements for multilayered anisotropic, composite plates and shells. *Archives of Computational Methods in Engineering*, 9(2):87–140, 2002.

[17] Reddy J.N. *Mechanics of Laminated Composite Plates and Shells – Theory and Analysis*. Boca Raton, CRC Press, 2nd edition, 2004.

[18] Reddy J.N. *An Introduction to the Finite Element Method*. Boston, Mc Graw Hill, 3rd edition, 2006.

[19] Saravanos D.A. and Heyliger P.R. Mechanics and computational models for laminated piezoelectric beams, plates and shells. *Applied Mechanics Reviews*, 52(10):305–320, 1999.

[20] Benjeddou A. Advances in piezoelectric finite element modeling of adaptive structural elements, a survey. *Computers and Structures*, 76:347–363, 2000.

[21] Carrera E. Developments, ideas, and evaluations based upon reissner's mixed variational theorem in the modeling of multilayered plates and shells. *Applied Mechanics Reviews*, 54(5):301–329, 2001.

[22] Li D. Layerwise theories of laminated composite structures and their applications: A review. *Archives of Computational Methods in Engineering*, 2020. doi: https://doi.org/10.1007/s11831-019-09392-2.

[23] Saravanos D.A., Heyliger P.R., and Hopkins D.A. Layerwise mechanics and finite element for the dynamic analysis of piezoelectric composite plates. *International Journal of Solids and Structures*, 34(3):359–378, 1997.

[24] Semedo Garção J.E., Mota Soares C.M., Mota Soares C.A., and Reddy J.N. Analysis of laminated adaptive plate structures using layerwise finite element models. *Computers and Structures*, 82: 1939–1959, 2004.

[25] Robaldo A., Carrera E., and Benjeddou A. A unified formulation for finite element analysis of piezoelectric adaptive plates. *Computers and Structures*, 8:1494–1505, 2006.

[26] Garcia Lage R., Mota Soares C.M., Mota Soares C.A., and Reddy J.N. Modelling of piezolaminated plates using layerwise mixed finite elements. *Computers and Structures*, 82:1849–1863, 2004.

[27] Carrera E. and Boscolo M. Classical and mixed finite elements for static and dynamic analysis of piezoelectric plates. *International Journal for Numerical Methods in Engineering*, 70:1135–1181, 2007.

[28] Moleiro F., Mota Soares C.M., and Mota Soares C.A. Assessment of a layerwise mixed least-squares model for analysis of multilayered piezoelectric composite plates. *Composite Structures*, 108–109:14–30, 2012.

[29] Moleiro F., Mota Soares C.M., and Mota Soares C.A. Layerwise mixed models for analysis of multilayered piezoelectric composite plates using least-squares formulation. *Composite Structures*, 119:134–149, 2015.

[30] Polit O. and Bruant I. Electric potential approximations for an eight node plate finite element. *Computers and Structures*, 84:1480–1493, 2006.

[31] Moreira R.A.S., Rodrigues J.D., and Ferreira A.J.M. A generalized layerwise finite element model for multi-layer damping treatments. *Computational Mechanics*, 37:426–444, 2006.

[32] Mantari J.L. and Guedes Soares C. Generalized layerwise hsdt and finite element formulation for symmetric laminated and sandwich composite plates. *Composite Structures*, 105:319–331, 2013.

[33] Araújo A.L., Mota Soares C.M., and Mota Soares C.A. Finite element model for hybrid active-passive damping analysis of anisotropic laminated sandwich structures. *Journal of Sandwich Structures and Materials*, 12:397–419, 2010.

[34] Lam K.Y., Peng X.Q., Liu G.R., and Reddy J.N. A finite-element model for piezoelectric composite laminates. *Smart Material and Structures*, 6:583–591, 1997.

[35] Dassault Systems Simulia Corporation. *Abaqus 6.14 Users's Manual*. 2014.

[36] Serway R. A. and Jewett J.W. *Physics for Scientists and Engineers*. Boston, Brooks/Cole, 9th edition, 2013.

[37] Araújo A.L., Lopes H.M.R., Vaz M.A.P., Mota Soares C.M., Herskovits J., and Pedersen P. Parameter estimation in active plate structures. *Composite Structures*, 84:1471–1479, 2006.

[38] Yang J. *An introduction to the theory of piezoelectricity*. Springer, 2005.

[39] Birman V. and Bert C.W. On the choice of shear correction factor in sandwich structures. *Journal of Sandwich Structures and Materials*, 4:83–95, 2002.

[40] Barlow J. Optimal stress locations in finite element models. *International Journal for Numerical Methods in Engineering*, 10:243–251, 1976.

[41] Hinton E. and Campbell J.S. Local and global smoothing of discontinuous finite element functions using a least squares method. *International Journal for Numerical Methods in Engineering*, 8: 461–480, 1974.

[42] Hinton E., Scott F.C., and Ricketts R.E. Local least squares stress smoothing for parabolic isoparametric elements. *International Journal for Numerical Methods in Engineering*, 9:235–256, 1975.

Appendix A

Piezoelectric Constitutive Equations

Piezoelectric constitutive equations can be derived in the same way as the Hooke's law for pure elastic materials. For this, an energetic principle must be used following the first law of thermodynamics, adding the contribution from the work done by the electric displacement in the electric field to the elastic deformation work, according to Campos [5].

A thermo-electro-elastic evolution over a piezoelectric material results in an infinitesimal variation of internal energy $d\mathcal{U}$, described following the first law of thermodynamics as shown,

$$d\mathcal{U} = \mathcal{T} dS + dW \tag{A.1}$$

where $\mathcal{T}$ is the absolute temperature, S the entropy and dW an infinitesimal of work, which is set to be the sum of both mechanical and electrical components, as follows:

$$dW = \sigma_{ij} d\varepsilon_{ij} - D_i dE_i \tag{A.2}$$

Replacing equation (A.2) in equation (A.1), one obtains the following energy balance:

$$d\mathcal{U} = \mathcal{T} dS + \sigma_{ij} d\varepsilon_{ij} - D_i dE_i \tag{A.3}$$

So far, from the previous equation, the total energy $\mathcal{U}$ is a function of the following state variables: entropy, strain field and electric field. From this point on, since the temperature is more reliable to measure than the entropy, the dependency entropy will be replaced by a dependency on the temperature, by means of a Legendre's transform that represents the free energy, Ψ_0, according to Yang [38] and Reddy's book [17]. Defining Ψ_0 as $\Psi_0 = \mathcal{U} - \mathcal{T} S$, one obtains the energy balance in equation (A.3), written in terms of Ψ_0 as shown,

$$d\Psi_0 = \sigma_{ij} d\varepsilon_{ij} - D_i dE_i - S d\mathcal{T} \tag{A.4}$$

which expresses the free energy as a function of the new state variables: temperature, strain field and

electric field. Noting that from equation (A.4), one obtains the following identities:

$$\sigma_{ij} = \frac{\partial \Psi_0}{\partial \varepsilon_{ij}} \, , D_i = -\frac{\partial \Psi_0}{\partial E_i} \, , S = -\frac{\partial \Psi_0}{\partial \mathcal{T}} \tag{A.5}$$

The presence of the temperature in equation (A.4) implies a couple phenomena between mechanical, electrical and thermal domains. A more complex constitutive equation can be achieved by taking into account thermal effects, where the coefficient of thermal expansion and pyroelectric properties are present. Excluding pyroelectric effects for simplicity, the piezoelectric constitutive equations can be derived, assuming that the temperature remains constant in equation (A.4), which means that $d\mathcal{T} = 0$, leading to:

$$d\Psi_0 = \sigma_{ij} d\varepsilon_{ij} - D_i dE_i \tag{A.6}$$

Now, equation (A.6) provides a stress field and electric displacement field dependent both on strains and electric field components.

Defining the elastic tensor C_{ijkl}, the piezoelectric tensor e_{ijk} and the dielectric tensor ϵ_{ij} as follows,

$$\begin{aligned}
C_{ijkl} &\equiv \frac{\partial \sigma_{ij}}{\partial \varepsilon_{kl}} = \frac{\partial^2 \Psi_0}{\partial \varepsilon_{kl} \partial \varepsilon_{ij}} = \frac{\partial^2 \Psi_0}{\partial \varepsilon_{ij} \partial \varepsilon_{kl}} \equiv C_{klij} \\
e_{ijk} &\equiv -\frac{\partial \sigma_{ij}}{\partial E_k} = -\frac{\partial^2 \Psi_0}{\partial \varepsilon_{ij} \partial E_k} = -\frac{\partial^2 \Psi_0}{\partial E_k \partial \varepsilon_{ij}} = \frac{\partial D_k}{\partial \varepsilon_{ij}} \equiv e_{jik} \\
\epsilon_{ij} &\equiv \frac{\partial D_i}{\partial E_j} = -\frac{\partial^2 \Psi_0}{\partial E_j \partial E_i} = -\frac{\partial^2 \Psi_0}{\partial E_i \partial E_j} = \frac{\partial D_j}{\partial E_i} \equiv \epsilon_{ji}
\end{aligned} \tag{A.7}$$

one obtains the differential form of the constitutive equations as shown:

$$\begin{aligned}
d\sigma_{ij} &= C_{ijkl} d\varepsilon_{kl} - e_{ijk} dE_k \\
dD_i &= e_{jki} d\varepsilon_{jk} + \epsilon_{ij} dE_j
\end{aligned} \tag{A.8}$$

Assuming a constant elastic tensor C_{ijkl}, piezoelectric tensor e_{ijk} and dielectric tensor ϵ_{ij}, the integration of equations (A.8) leads to the linear piezoelectric constitutive equations as follows:

$$\begin{aligned}
\sigma_{ij} &= C_{ijkl} \varepsilon_{kl} - e_{ijk} E_k \\
D_i &= e_{jki} \varepsilon_{jk} + \epsilon_{ij} E_j
\end{aligned} \tag{A.9}$$

The 4$^{\text{th}}$-order constitutive elastic tensor C_{ijkl} is doubly symmetric and symmetric in the first and last two indices. Hence, the elastic tensor has in general 21 independent entries as such as a symmetric 6×6 matrix. The piezoelectric tensor is a symmetric 3$^{\text{rd}}$-order tensor, having 18 independent components, while the dielectric tensor ϵ_{ij} is a symmetric 2$^{\text{nd}}$-order tensor, with 6 independent components

A reduced number of independent components is found for some types of material systems, such as the orthotropic, the transversely isotropic or the isotropic material systems, as can bee seen in Section 2.1 and in more detail in Reddy's book [17].

Appendix B

Electro-elastic Variational Principle

Consider an arbitrary elastic solid, with volume domain Ω, made of an anisotropic composite material with piezoelectric effect, subjected to a volume force f_i. According to Reddy [17], following a linear momentum balance to an infinitesimal piece of volume, the equilibrium equation, in the i-direction, in terms of the Cauchy stress tensor σ_{ij} and the displacement field u_i is given by,

$$\frac{\partial \sigma_{ij}}{\partial x_j} + f_i = \rho \frac{\partial^2 u_i}{\partial t^2} \quad \text{on } \Omega \tag{B.1}$$

and from an angular momentum balance, the symmetry property of the stress tensor, i.e., $\sigma_{ij} = \sigma_{ji}$ is proved.

From the electrostatics point of view, the Gauss law for the electric displacement field, in the absence of volumetric distributed charges, is valid over the piezoelectric medium according to Yang [38],

$$\frac{\partial D_i}{\partial x_i} = 0 \quad \text{on } \Omega \tag{B.2}$$

Essential and natural boundary conditions for the differential equations (B.1) and (B.2) are respectively,

$$u_i = u_i^s \ \text{ on } S_u \ \ , \ \ \phi = \phi^s \ \text{ on } S_\phi \tag{B.3}$$

and

$$\sigma_{ij} n_j = t_i^s \ \text{ on } S_t \ \ , \ \ D_i n_i = \mathcal{Q}^s \ \text{ on } S_\mathcal{Q} \tag{B.4}$$

representing applied displacement u_i^s, applied potential ϕ^s, applied stress t_i^s and applied surface charge $\mathcal{Q}^s$.

Moreover, the electric field is assumed to be irrotational, i.e., conservative, since negligible magnetic effects may be assumed, $\partial_t B_i \approx 0$, leading to an electro-quasi-static description. Following the Faraday's law accordingly to Serway's book [36] one obtains,

$$\varepsilon_{ijk} \nabla_j E_k = -\partial_t B_i = 0 \tag{B.5}$$

where ∇_j is the spatial gradient operator in the j-direction, ∂_t the time derivative operator and ε_{ijk} is the Lévi-Civita symbol. Consequently, from the fundamental theorem of calculus applied to the Faraday's law in equation (2.5), the electric field can be represented in terms of a gradient of a scalar field, the electric potential ϕ, as follows:

$$E_k = -\frac{\partial \phi}{\partial x_k} \tag{B.6}$$

Substituting the piezoelectric constitutive equations (A.9), into the coupled governing differential equations of linear momentum (B.1) and Gauss law (B.2), and using the field-potential relation in equation (B.6), as well as the infinitesimal strain tensor definition, i.e.,

$$\varepsilon_{kl} = \frac{1}{2}\left(\frac{\partial u_k}{\partial x_l} + \frac{\partial u_l}{\partial x_k}\right) \tag{B.7}$$

one obtains the following displacement based strong formulation for piezoelectric analysis as shown,

$$\frac{1}{2}C_{ijkl}\left(\frac{\partial^2 u_k}{\partial x_j \partial x_l} + \frac{\partial^2 u_l}{\partial x_j \partial x_k}\right) + e_{ijk}\frac{\partial^2 \phi}{\partial x_j \partial x_k} + f_i = \rho \frac{\partial^2 u_i}{\partial t^2} \quad \text{on } \Omega \tag{B.8}$$

$$\epsilon_{ij}\frac{\partial^2 \phi}{\partial x_i \partial x_j} - \frac{1}{2}e_{jki}\left(\frac{\partial^2 u_k}{\partial x_i \partial x_j} + \frac{\partial^2 u_j}{\partial x_i \partial x_k}\right) = 0 \quad \text{on } \Omega \tag{B.9}$$

equipped with essential and natural boundary conditions in equations (B.3) and (B.4), respectively.

Following Reddy's book [17], the principle of virtual displacements states that the virtual work for an arbitrary admissible variable of the displacement field δu_i and potential $\delta\phi$ is null in equilibrium. Hence, and according to Benjeddou [20], for an arbitrary admissible variation of displacement δu_i and an admissible variation of electric potential $\delta\phi$, equations (B.1) and (B.2) are equivalent to:

$$\int_\Omega \left(\frac{\partial \sigma_{ij}}{\partial x_j} + f_i - \rho\frac{\partial^2 u_i}{\partial t^2}\right)\delta u_i + \frac{\partial D_i}{\partial x_i}\delta\phi \; d\Omega = 0 \tag{B.10}$$

and using the linear property of the integral operator, one obtains:

$$\int_\Omega \frac{\partial \sigma_{ij}}{\partial x_j}\delta u_i d\Omega + \int_\Omega f_i \delta u_i d\Omega - \int_\Omega \rho\frac{\partial^2 u_i}{\partial t^2}\delta u_i d\Omega + \int_\Omega \frac{\partial D_i}{\partial x_i}\delta\phi \; d\Omega = 0 \tag{B.11}$$

The first and last terms of equation (B.11) can now be simplified using integration by parts and the divergence theorem, accordingly to Reddy's book [18]. Also the symmetry property of the stress tensor must be taken into account, as well as the natural boundary conditions (B.4), the piezoelectric constitutive equations (A.9), the relation between electric potential and electric field in equation (B.6), as well as the infinitesimal strain tensor definition in equation (B.7). Following this procedure, the stress dependent term in (B.11) holds,

$$\begin{aligned}\int_\Omega \frac{\partial \sigma_{ij}}{\partial x_j}\delta u_i d\Omega &= -\int_\Omega \sigma_{ij}\frac{\partial \delta u_i}{\partial x_j}d\Omega + \oint_{\partial\Omega}\sigma_{ij}n_j\delta u_i dA \\ &= -\int_\Omega \sigma_{ij}\frac{\partial \delta u_i}{\partial x_j}d\Omega + \int_{S_t} t_i\delta u_i dA \\ &= -\frac{1}{2}\int_\Omega \sigma_{ij}\frac{\partial \delta u_i}{\partial x_j} + \sigma_{ji}\frac{\partial \delta u_j}{\partial x_i}d\Omega + \int_{S_t} t_i\delta u_i dA \\ &= -\int_\Omega \sigma_{ij}\frac{1}{2}\left(\frac{\partial \delta u_i}{\partial x_j} + \frac{\partial \delta u_j}{\partial x_i}\right)d\Omega + \int_{S_t} t_i^s\delta u_i dA \\ &= -\int_\Omega \sigma_{ij}\delta\varepsilon_{ij}d\Omega + \int_{S_t} t_i^s\delta u_i dA \\ &= -\int_\Omega C_{ijkl}\varepsilon_{kl}\delta\varepsilon_{ij}d\Omega + \int_\Omega e_{ijk}E_k\delta\varepsilon_{ij}d\Omega + \int_{S_t} t_i^s\delta u_i dA\end{aligned} \tag{B.12}$$

while the electric displacement dependent term becomes,

$$\begin{aligned}\int_\Omega \frac{\partial D_i}{\partial x_i}\delta\phi\, d\Omega &= -\int_\Omega D_i\frac{\partial \delta\phi}{\partial x_i}d\Omega + \oint_{\partial\Omega} D_i n_i\delta\phi\, dA \\ &= \int_\Omega D_i\delta E_i\, d\Omega + \int_{S_\mathcal{Q}} \mathcal{Q}^s\delta\phi\, dA \\ &= \int_\Omega e_{jki}\varepsilon_{jk}\delta E_i\, d\Omega + \int_\Omega \epsilon_{ij}E_j\delta E_i\, d\Omega + \int_{S_\mathcal{Q}} \mathcal{Q}^s\delta\phi\, dA\end{aligned} \tag{B.13}$$

Replacing the previous results of equations (B.12) and (B.13) into equation (B.11), one obtains the variational principle as follows,

$$\begin{aligned}0 = \int_\Omega &-C_{ijkl}\varepsilon_{kl}\delta\varepsilon_{ij} + e_{ijk}E_k\delta\varepsilon_{ij} + e_{jki}\varepsilon_{jk}\delta E_i + \epsilon_{ij}E_j\delta E_i + f_i\delta u_i - \rho\frac{\partial^2 u_i}{\partial t^2}\delta u_i\, d\Omega \\ &+ \int_{S_t} t_i^s\delta u_i dA + \int_{S_\mathcal{Q}} \mathcal{Q}^s\delta\phi\, dA\end{aligned} \tag{B.14}$$

which is equivalent to have:

$$\begin{aligned}\int_\Omega &C_{ijkl}\varepsilon_{kl}\delta\varepsilon_{ij} - e_{ijk}E_k\delta\varepsilon_{ij} - e_{jki}\varepsilon_{jk}\delta E_i - \epsilon_{ij}E_j\delta E_i - f_i\delta u_i + \rho\frac{\partial^2 u_i}{\partial t^2}\delta u_i\, d\Omega \\ &= \int_{S_t} t_i^s\delta u_i dA + \int_{S_\mathcal{Q}} \mathcal{Q}^s\delta\phi\, dA\end{aligned} \tag{B.15}$$

Appendix C

Generalized Strain and Electric Field Matrices

For the three k-discrete layers considered in the present model, i.e., $k = \{t, c, b\}$ (top, core and bottom layers), the generalized strain matrices $[B]_j^{(k)}$ and generalized electric field matrices $[B_\phi]_j^{(k)}$ for an arbitrary j-node, regarding both models (through-thickness linear and quadratic electric potential), are presented.

Considering a finite element present in a mesh, the generalized strains and generalized electric field components for the k-layer, can be calculated using the respective nodal strain matrices and nodal electric field matrices in equations (4.8) and (4.10). Where the nodal strain and electric field matrices are derived, replacing the finite element approximation for the DOFs in the strains and electric field definitions, for each discrete layer, in equations (3.17), (3.18), (3.19, (3.31), (3.32), (3.33) and (3.37), following the generalized strain and electric field definitions in equations (3.22) and (3.34), respectively.

C.1 UEL1: Linear Electric Potential

Core Layers

$$[B]_j^c = \begin{bmatrix} \frac{\partial \psi_j}{\partial x} & 0 & 0 & 0 & 0 & 0 & 0 & 0 & 0 \\ 0 & \frac{\partial \psi_j}{\partial y} & 0 & 0 & 0 & 0 & 0 & 0 & 0 \\ \frac{\partial \psi_j}{\partial y} & \frac{\partial \psi_j}{\partial x} & 0 & 0 & 0 & 0 & 0 & 0 & 0 \\ 0 & 0 & 0 & \frac{\partial \psi_j}{\partial x} & 0 & 0 & 0 & 0 & 0 \\ 0 & 0 & 0 & 0 & \frac{\partial \psi_j}{\partial y} & 0 & 0 & 0 & 0 \\ 0 & 0 & 0 & \frac{\partial \psi_j}{\partial y} & \frac{\partial \psi_j}{\partial x} & 0 & 0 & 0 & 0 \\ 0 & 0 & \frac{\partial \psi_j}{\partial y} & 0 & \psi_j & 0 & 0 & 0 & 0 \\ 0 & 0 & \frac{\partial \psi_j}{\partial x} & \psi_j & 0 & 0 & 0 & 0 & 0 \end{bmatrix}, \quad [B_\phi]_j^c = \begin{bmatrix} 0 & \frac{\partial \psi_j}{\partial x} & \frac{\partial \psi_j}{\partial x} & 0 \\ 0 & \frac{\partial \psi_j}{\partial y} & \frac{\partial \psi_j}{\partial y} & 0 \\ 0 & -\frac{\partial \psi_j}{\partial x} & \frac{\partial \psi_j}{\partial x} & 0 \\ 0 & -\frac{\partial \psi_j}{\partial y} & \frac{\partial \psi_j}{\partial y} & 0 \\ 0 & -\psi_j & \psi_j & 0 \end{bmatrix} \tag{C.1}$$

Top Layer

$$[B]_j^t = \begin{bmatrix} 0 & 0 & 0 & 0 & 0 & \frac{\partial\psi_j}{\partial x} & 0 & 0 & 0 \\ 0 & 0 & 0 & 0 & 0 & 0 & \frac{\partial\psi_j}{\partial y} & 0 & 0 \\ 0 & 0 & 0 & 0 & 0 & \frac{\partial\psi_j}{\partial y} & \frac{\partial\psi_j}{\partial x} & 0 & 0 \\ \alpha_1\frac{\partial\psi_j}{\partial x} & 0 & 0 & \alpha_2\frac{\partial\psi_j}{\partial x} & 0 & \alpha_3\frac{\partial\psi_j}{\partial x} & 0 & 0 & 0 \\ 0 & \alpha_1\frac{\partial\psi_j}{\partial y} & 0 & 0 & \alpha_2\frac{\partial\psi_j}{\partial y} & 0 & \alpha_3\frac{\partial\psi_j}{\partial y} & 0 & 0 \\ \alpha_1\frac{\partial\psi_j}{\partial y} & \alpha_1\frac{\partial\psi_j}{\partial x} & 0 & \alpha_2\frac{\partial\psi_j}{\partial y} & \alpha_2\frac{\partial\psi_j}{\partial x} & \alpha_3\frac{\partial\psi_j}{\partial y} & \alpha_3\frac{\partial\psi_j}{\partial x} & 0 & 0 \\ 0 & \alpha_1\psi_j & \frac{\partial\psi_j}{\partial y} & 0 & \alpha_2\psi_j & 0 & \alpha_3\psi_j & 0 & 0 \\ \alpha_1\psi_j & 0 & \frac{\partial\psi_j}{\partial x} & \alpha_2\psi_j & 0 & \alpha_3\psi_j & 0 & 0 & 0 \end{bmatrix}, \quad [B_\phi]_j^t = \begin{bmatrix} 0 & 0 & \frac{\partial\psi_j}{\partial x} & \frac{\partial\psi_j}{\partial x} \\ 0 & 0 & \frac{\partial\psi_j}{\partial y} & \frac{\partial\psi_j}{\partial y} \\ 0 & 0 & -\frac{\partial\psi_j}{\partial x} & \frac{\partial\psi_j}{\partial x} \\ 0 & 0 & -\frac{\partial\psi_j}{\partial y} & \frac{\partial\psi_j}{\partial y} \\ 0 & 0 & -\psi_j & \psi_j \end{bmatrix} \tag{C.2}$$

Bottom Layer

$$[B]_j^b = \begin{bmatrix} 0 & 0 & 0 & 0 & 0 & 0 & 0 & \frac{\partial\psi_j}{\partial x} & 0 \\ 0 & 0 & 0 & 0 & 0 & 0 & 0 & 0 & \frac{\partial\psi_j}{\partial y} \\ 0 & 0 & 0 & 0 & 0 & 0 & 0 & \frac{\partial\psi_j}{\partial y} & \frac{\partial\psi_j}{\partial x} \\ \beta_1\frac{\partial\psi_j}{\partial x} & 0 & 0 & \beta_2\frac{\partial\psi_j}{\partial x} & 0 & 0 & 0 & \beta_3\frac{\partial\psi_j}{\partial x} & 0 \\ 0 & \beta_1\frac{\partial\psi_j}{\partial y} & 0 & 0 & \beta_2\frac{\partial\psi_j}{\partial y} & 0 & 0 & 0 & \beta_3\frac{\partial\psi_j}{\partial y} \\ \beta_1\frac{\partial\psi_j}{\partial y} & \beta_1\frac{\partial\psi_j}{\partial x} & 0 & \beta_2\frac{\partial\psi_j}{\partial y} & \beta_2\frac{\partial\psi_j}{\partial x} & 0 & 0 & \beta_3\frac{\partial\psi_j}{\partial y} & \beta_3\frac{\partial\psi_j}{\partial x} \\ 0 & \beta_1\psi_j & \frac{\partial\psi_j}{\partial y} & 0 & \beta_2\psi_j & 0 & 0 & 0 & \beta_3\psi_j \\ \beta_1\psi_j & 0 & \frac{\partial\psi_j}{\partial x} & \beta_2\psi_j & 0 & 0 & 0 & \beta_3\psi_j & 0 \end{bmatrix}, \quad [B_\phi]_j^b = \begin{bmatrix} \frac{\partial\psi_j}{\partial x} & \frac{\partial\psi_j}{\partial x} & 0 & 0 \\ \frac{\partial\psi_j}{\partial y} & \frac{\partial\psi_j}{\partial y} & 0 & 0 \\ -\frac{\partial\psi_j}{\partial x} & \frac{\partial\psi_j}{\partial x} & 0 & 0 \\ -\frac{\partial\psi_j}{\partial y} & \frac{\partial\psi_j}{\partial y} & 0 & 0 \\ -\psi_j & \psi_j & 0 & 0 \end{bmatrix} \tag{C.3}$$

C.2 UEL2: Quadratic Electric Potential

Since in UEL2 model the displacement field is the same as in UEL1, the generalized strain matrices remain the same ones as shown previously. The new generalized electric field matrices for a through-thickness quadratic electric potential, for each discrete layer, are the following:

Core Layers

$$[B_\phi]_j^c = -\begin{bmatrix} 0 & 0 & \frac{\partial\psi_j}{\partial x} & 0 & 0 & 0 & 0 \\ 0 & \frac{\partial\psi_j}{\partial x} & 0 & 0 & 0 & 0 & 0 \\ 0 & 0 & 0 & 0 & 0 & \frac{\partial\psi_j}{\partial x} & 0 \\ 0 & 0 & \frac{\partial\psi_j}{\partial y} & 0 & 0 & 0 & 0 \\ 0 & \frac{\partial\psi_j}{\partial y} & 0 & 0 & 0 & 0 & 0 \\ 0 & 0 & 0 & 0 & 0 & \frac{\partial\psi_j}{\partial y} & 0 \\ 0 & 0 & \psi_j & 0 & 0 & 0 & 0 \\ 0 & \psi_j & 0 & 0 & 0 & 0 & 0 \\ 0 & 0 & 0 & 0 & 0 & \psi_j & 0 \end{bmatrix} \tag{C.4}$$

Top Layer

$$[B_\phi]_j^t = - \begin{bmatrix} 0 & 0 & 0 & \frac{\partial \psi_j}{\partial x} & 0 & 0 & 0 \\ 0 & 0 & \frac{\partial \psi_j}{\partial x} & 0 & 0 & 0 & 0 \\ 0 & 0 & 0 & 0 & 0 & 0 & \frac{\partial \psi_j}{\partial x} \\ 0 & 0 & 0 & \frac{\partial \psi_j}{\partial y} & 0 & 0 & 0 \\ 0 & 0 & \frac{\partial \psi_j}{\partial y} & 0 & 0 & 0 & 0 \\ 0 & 0 & 0 & 0 & 0 & 0 & \frac{\partial \psi_j}{\partial y} \\ 0 & 0 & 0 & \psi_j & 0 & 0 & 0 \\ 0 & 0 & \psi_j & 0 & 0 & 0 & 0 \\ 0 & 0 & 0 & 0 & 0 & 0 & \psi_j \end{bmatrix} \tag{C.5}$$

Bottom Layer

$$[B_\phi]_j^b = - \begin{bmatrix} 0 & \frac{\partial \psi_j}{\partial x} & 0 & 0 & 0 & 0 & 0 \\ \frac{\partial \psi_j}{\partial x} & 0 & 0 & 0 & 0 & 0 & 0 \\ 0 & 0 & 0 & 0 & \frac{\partial \psi_j}{\partial x} & 0 & 0 \\ 0 & \frac{\partial \psi_j}{\partial y} & 0 & 0 & 0 & 0 & 0 \\ \frac{\partial \psi_j}{\partial y} & 0 & 0 & 0 & 0 & 0 & 0 \\ 0 & 0 & 0 & 0 & \frac{\partial \psi_j}{\partial y} & 0 & 0 \\ 0 & \psi_j & 0 & 0 & 0 & 0 & 0 \\ \psi_j & 0 & 0 & 0 & 0 & 0 & 0 \\ 0 & 0 & 0 & 0 & \psi_j & 0 & 0 \end{bmatrix} \tag{C.6}$$

Appendix D

Generalized Constitutive Matrices

In the present models, generalized constitutive equations appear as a relation between the stress resultants and the generalized strain and electric field. For an arbitrary k-discrete layer (where k stands for top, core or bottom layers), the generalized matrices in equation (3.44) are determined for the UEL1 model, with a through-thickness linear electric potential.

D.1 UEL1: Linear Electric Potential

From the integration across the thickness of equation (3.44), one obtains the generalized constitutive matrices as follows:

$$[\hat{Q}]_{(k)} = \begin{bmatrix} \bar{Q}_{11}\bar{H}_{0_{(k)}} & \bar{Q}_{12}\bar{H}_{0_{(k)}} & \bar{Q}_{16}\bar{H}_{0_{(k)}} & \bar{Q}_{11}\bar{H}_{1_{(k)}} & \bar{Q}_{12}\bar{H}_{1_{(k)}} & \bar{Q}_{16}\bar{H}_{1_{(k)}} & 0 & 0 \\ \bar{Q}_{12}\bar{H}_{0_{(k)}} & \bar{Q}_{22}\bar{H}_{0_{(k)}} & \bar{Q}_{26}\bar{H}_{0_{(k)}} & \bar{Q}_{12}\bar{H}_{1_{(k)}} & \bar{Q}_{22}\bar{H}_{1_{(k)}} & \bar{Q}_{26}\bar{H}_{1_{(k)}} & 0 & 0 \\ \bar{Q}_{16}\bar{H}_{0_{(k)}} & \bar{Q}_{26}\bar{H}_{0_{(k)}} & \bar{Q}_{66}\bar{H}_{0_{(k)}} & \bar{Q}_{16}\bar{H}_{1_{(k)}} & \bar{Q}_{26}\bar{H}_{1_{(k)}} & \bar{Q}_{66}\bar{H}_{1_{(k)}} & 0 & 0 \\ \bar{Q}_{11}\bar{H}_{1_{(k)}} & \bar{Q}_{12}\bar{H}_{1_{(k)}} & \bar{Q}_{16}\bar{H}_{1_{(k)}} & \bar{Q}_{11}\bar{H}_{2_{(k)}} & \bar{Q}_{12}\bar{H}_{2_{(k)}} & \bar{Q}_{16}\bar{H}_{2_{(k)}} & 0 & 0 \\ \bar{Q}_{12}\bar{H}_{1_{(k)}} & \bar{Q}_{22}\bar{H}_{1_{(k)}} & \bar{Q}_{26}\bar{H}_{1_{(k)}} & \bar{Q}_{12}\bar{H}_{2_{(k)}} & \bar{Q}_{22}\bar{H}_{2_{(k)}} & \bar{Q}_{26}\bar{H}_{2_{(k)}} & 0 & 0 \\ \bar{Q}_{16}\bar{H}_{1_{(k)}} & \bar{Q}_{26}\bar{H}_{1_{(k)}} & \bar{Q}_{66}\bar{H}_{1_{(k)}} & \bar{Q}_{16}\bar{H}_{2_{(k)}} & \bar{Q}_{26}\bar{H}_{2_{(k)}} & \bar{Q}_{66}\bar{H}_{2_{(k)}} & 0 & 0 \\ 0 & 0 & 0 & 0 & 0 & 0 & K_s\bar{Q}_{44}\bar{H}_{0_{(k)}} & K_s\bar{Q}_{45}\bar{H}_{0_{(k)}} \\ 0 & 0 & 0 & 0 & 0 & 0 & K_s\bar{Q}_{45}\bar{H}_{0_{(k)}} & K_s\bar{Q}_{55}\bar{H}_{0_{(k)}} \end{bmatrix} \tag{D.1}$$

$$[\hat{e}]_{(k)} = \begin{bmatrix} 0 & 0 & 0 & 0 & \bar{e}_{31}\bar{H}_{0_{(k)}}/h_{(k)} \\ 0 & 0 & 0 & 0 & \bar{e}_{32}\bar{H}_{0_{(k)}}/h_{(k)} \\ 0 & 0 & 0 & 0 & \bar{e}_{36}\bar{H}_{0_{(k)}}/h_{(k)} \\ 0 & 0 & 0 & 0 & \bar{e}_{31}\bar{H}_{1_{(k)}}/h_{(k)} \\ 0 & 0 & 0 & 0 & \bar{e}_{32}\bar{H}_{1_{(k)}}/h_{(k)} \\ 0 & 0 & 0 & 0 & \bar{e}_{36}\bar{H}_{1_{(k)}}/h_{(k)} \\ \bar{e}_{14}\bar{H}_{0_{(k)}}/2 & \bar{e}_{24}\bar{H}_{0_{(k)}}/2 & \bar{e}_{14}\bar{H}_{1_{(k)}}/h_{(k)} & \bar{e}_{24}\bar{H}_{1_{(k)}}/h_{(k)} & 0 \\ \bar{e}_{15}\bar{H}_{0_{(k)}}/2 & \bar{e}_{25}\bar{H}_{0_{(k)}}/2 & \bar{e}_{15}\bar{H}_{1_{(k)}}/h_{(k)} & \bar{e}_{25}\bar{H}_{1_{(k)}}/h_{(k)} & 0 \end{bmatrix} \tag{D.2}$$

$$[\hat{\epsilon}]_{(k)} = \begin{bmatrix} \epsilon_{xx}\bar{H}_{0_{(k)}}/4 & \epsilon_{xy}\bar{H}_{0_{(k)}}/4 & \epsilon_{xx}\bar{H}_{1_{(k)}}/(2h_{(k)}) & \epsilon_{xy}\bar{H}_{1_{(k)}}/(2h_{(k)}) & 0 \\ \epsilon_{xy}\bar{H}_{0_{(k)}}/4 & \epsilon_{yy}\bar{H}_{0_{(k)}}/4 & \epsilon_{xy}\bar{H}_{1_{(k)}}/(2h_{(k)}) & \epsilon_{yy}\bar{H}_{1_{(k)}}/(2h_{(k)}) & 0 \\ \epsilon_{xx}\bar{H}_{1_{(k)}}/(2h_{(k)}) & \epsilon_{xy}\bar{H}_{1_{(k)}}/(2h_{(k)}) & \epsilon_{xx}\bar{H}_{2_{(k)}}/h^2_{(k)} & \epsilon_{xy}\bar{H}_{2_{(k)}}/h^2_{(k)} & 0 \\ \epsilon_{xy}\bar{H}_{1_{(k)}}/(2h_{(k)}) & \epsilon_{yy}\bar{H}_{1_{(k)}}/(2h_{(k)}) & \epsilon_{xy}\bar{H}_{2_{(k)}}/h^2_{(k)} & \epsilon_{yy}\bar{H}_{2_{(k)}}/h^2_{(k)} & 0 \\ 0 & 0 & 0 & 0 & \epsilon_{zz}\bar{H}_{0_{(k)}}/h^2_{(k)} \end{bmatrix} \tag{D.3}$$

In this generalized constitutive matrices, thickness integrals of the z-dependent functions, contained in $[S]_{(k)}$ and $[S_\phi]_{(k)}$ matrices, are represented by $\bar{H}_{n_{(k)}}$, with $n = \{0, 1, 2, 3\}$ and $k = \{b, c, t\}$, defined as,

$$\bar{H}_{n_{(k)}} = \left[\frac{(z - \bar{z}_k)^{n+1}}{n+1}\right]_{z=z^{inf}_{(k)}}^{z=z^{sup}_{(k)}} \tag{D.4}$$

where $z^{inf}_{(k)}$ and $z^{sup}_{(k)}$ are the bottom and top transverse coordinates of the k-discrete layer, respectively, and $\bar{z}_k$ is the transverse coordinate of the k-layer mid-plane. Moreover, the elastic, piezoelectric and dielectric constants must be properties of the material associated to the k-layer.

D.2 UEL2: Quadratic Electric Potential

Since in the UEL2 model the displacement field is the same as in UEL1 model, hence the generalized constitutive elastic matrix $[\hat{Q}]$ remains the same as for UEL1. The new generalized constitutive piezoelectric and dielectric matrices for a through-thickness quadratic electric potential are not presented for brevity. It can be noticed that they are similar to the previous ones, adding higher order terms due to a higher order description for the electric potential.

Appendix E

UEL1 Static Analysis Results for Thin Plates

In this appendix, the UEL1 model static analysis results are presented, for Case 1, [PZT-4/0° /90° /0° /PZT-4], and Case 2, [PVDF/90° /0° /90° /PVDF], regarding thin plates with $a/h = 100$. Both applied load and applied potential results are respectively shown in tables E.1 and E.2 for Case 1, and in tables E.3 and E.4 for Case 2.

As mentioned in Chapter 6, the results with UEL1 are mostly similar to the already presented UEL2 results, namely to the ones present in tables 6.3 to 6.6 for Case 1, and in tables 6.21 to 6.24 for Case 2.

E.1 Case 1- Transversely Isotropic Piezoelectric Layers

Table E.1: UEL1 Results for Case 1, with $a/h = 100$, under applied load.

z/h	$u \times 10^{12}$	$w \times 10^{11}$	$\phi \times 10^{3}$	σ_{xx}	$D_x \times 10^{12}$	$D_z \times 10^{12}$	τ_{xz}	τ_{yz}
1/2	-6500.18	41496.31	0.000	3084.31	2790.69	-61294.64	5.62	5.62
2/5	-5196.76	41496.31	40.211	2586.52	1141.59	61307.07	7.22	7.22
2/5	-5196.76	41496.31	40.211	2216.19	-3.91	0.00	25.24	12.15
2/15	-1732.25	41496.31	40.211	738.73	-3.91	0.00	25.24	12.15
2/15	-1732.25	41496.31	40.211	73.07	-3.35	0.00	16.10	19.06
-2/15	1732.25	41496.31	40.211	-73.07	-3.35	0.00	16.10	19.06
-2/15	1732.25	41496.31	40.211	-738.73	-3.91	0.00	25.24	12.15
-2/5	5196.76	41496.31	40.211	-2216.19	-3.91	0.00	25.24	12.15
-2/5	5196.76	41496.31	40.211	-2586.52	1141.59	-61307.07	7.22	7.22
-1/2	6500.18	41496.31	0.000	-3084.31	2790.69	61294.64	5.62	5.62

Table E.2: UEL1 Results for Case 1, with $a/h = 100$, under applied potential.

z/h	$u \times 10^{12}$	$w \times 10^{11}$	ϕ	σ_{xx}	$D_x \times 10^8$	$D_z \times 10^8$	τ_{xz}	τ_{yz}
1/2	-2.861	-1.224	1.0000	-2.360	-6.097	-0.359	0.0061	0.0064
2/5	-1.436	-1.224	0.9998	-2.941	-6.096	-0.344	-0.0034	-0.0031
2/5	-1.436	-1.224	0.9998	0.606	-0.008	-0.332	-0.0002	0.0000
2/15	-1.480	-1.224	0.6666	0.650	-0.006	-0.332	-0.0002	0.0000
2/15	-1.480	-1.224	0.6666	0.071	-0.004	-0.332	-0.0001	0.0000
-2/15	-1.612	-1.224	0.3334	0.076	-0.003	-0.332	-0.0001	0.0000
-2/15	-1.612	-1.224	0.3334	0.693	-0.002	-0.332	-0.0002	0.0000
-2/5	-1.700	-1.224	0.0002	0.737	0.000	-0.332	-0.0002	0.0000
-2/5	-1.700	-1.224	0.0002	-2.657	-0.001	-0.332	0.0086	0.0083
-1/2	-1.750	-1.224	0.0000	-2.642	0.000	-0.332	-0.0005	-0.0008

E.2 Case 2- Orthotropic Piezoelectric Layers

Table E.3: UEL1 Results for Case 2, with $a/h = 100$, under applied load.

z/h	$u \times 10^{12}$	$w \times 10^{11}$	$\phi \times 10^3$	σ_{xx}	$D_x \times 10^{12}$	$D_z \times 10^{12}$	τ_{xz}	τ_{yz}
1/2	-8366.16	53402.20	0.00	6351.84	-22.29	-425.988	9.809	1.539
2/5	-6690.71	53402.20	33.71	5080.28	-34.01	425.706	9.808	1.538
2/5	-6690.71	53402.20	33.71	282.24	-2.81	0.000	18.073	17.663
-2/5	6690.71	53402.20	33.71	-282.24	-2.81	0.000	18.073	17.663
-2/5	6690.71	53402.20	33.71	-5080.28	-34.01	-425.706	9.808	1.538
-1/2	8366.16	53402.20	0.00	-6351.84	-22.29	425.988	9.809	1.539

Table E.4: UEL1 Results for Case 2, with $a/h = 100$, under applied potential.

z/h	$u \times 10^{12}$	$w \times 10^{11}$	ϕ	σ_{xx}	$D_x \times 10^8$	$D_z \times 10^8$	τ_{xz}	τ_{yz}
1/2	-1.182	0.020	1.000	-1.096	-0.035	-0.3144	-0.002	-0.004
2/5	-1.188	0.020	0.972	-1.091	-0.003	-0.3144	-0.001	-0.003
2/5	-1.188	0.020	0.972	0.055	-0.008	-0.3141	0.000	0.000
-2/5	-1.183	0.020	0.028	0.054	0.000	-0.3141	0.000	0.000
-2/5	-1.183	0.020	0.028	-1.093	-0.001	-0.3140	0.001	0.003
-1/2	-1.183	0.020	0.000	-1.093	0.000	-0.3140	0.002	0.004